

Simulation Studies of Functional Electrical Stimulation for Facial Reanimation

Patrick Brebner

Department of Biological & Biomedical Engineering

McGill University, Montreal

April 2021



A thesis submitted to McGill University in partial fulfillment of the requirements of the degree
of Master of Engineering.

Abstract

Facial palsy can be a devastating condition that often impairs blinking and can lead to other functional, esthetic, communication, and psychological issues. The current reanimation technologies aimed at restoring function often only achieve limited results, usually only enabling functional movement through non-spontaneous means. Due to recent advances, techniques like facial pacing have become feasible. Facial pacing is a technique proposed to restore the symmetry of facial movement that has been lost due to unilateral facial paralysis. The main idea of facial pacing is to measure the muscle activity from the healthy side with electromyography (EMG) and use this to activate the muscles on the paralyzed side through functional electrical stimulation (FES). This thesis uses simulation studies to investigate the feasibility of building a facial reanimation control system (FRCS) that uses EMG to determine the stimulus required for synchronous movements on the paralyzed side. Based on our knowledge of muscle physiology, simulation models were developed that represent the healthy and paralyzed sides of the face. These models simulated the signals needed to identify the models required for the FRCS. The identified models were validated and tested for various conditions to determine if they were robust enough for use in a facial reanimation device. The results indicate that we can successfully identify these models, using the simulated data, that are able to achieve high accuracies for reasonable signal record lengths and output noise levels. The results are a proof of concept that shows that the FRCS is a feasible approach to facial pacing. The next step will be to apply the methods developed in this thesis to experimental data.

Résumé

Not required for the initial thesis submission.

Table of Contents

Abstract.....	ii
Résumé	iii
Table of Contents.....	iv
Acknowledgments.....	vi
Contribution of Authors.....	vi
Chapter 1: Introduction	1
Chapter 2: Background	4
2.1 Motor Unit Physiology	4
2.1.1 Motor Neuron	4
2.1.2 Muscle Fibers	5
2.2 Muscle Behavior.....	7
2.2.1 Force Summation.....	7
2.2.2 Muscle Recruitment.....	8
2.2.3 Force-Length and Force-Velocity Relationship	9
2.2.4 Muscle Feedback.....	11
2.3 Functional Electrical Stimulation	11
2.4 Muscle Modeling.....	13
2.4.1 Electromyogram.....	13
2.4.3 Muscle Activation and Contraction Dynamics	17
2.4.4 Categories of Muscle Models.....	18
2.4.5 Hammerstein Models.....	19
Chapter 3: Literature Review	20
3.1 Facial Palsy	20
3.2 Current Treatments	21
3.3 Facial Reanimation.....	24
3.4 Rationale and Objective	25
Chapter 4: Methods & Results – EMG Response System (ERS)	29
4.1 Methods: EMG Response System	29
4.1.1 ERS Simulation Model.....	29
4.1.2 Input Signals.....	34
4.1.3 ERS Model Identification.....	36
4.2 Results: EMG Response System	36

Simulation Studies of Functional Electrical Stimulation for Facial Reanimation
Patrick Brebner

4.2.1 Simulation and Identification with PRBS Inputs	36
4.2.2 Simulation and Identification with “Physiological” Input	40
4.2.3 ERS Model Validation.....	44
4.2.4 Input Signal Limitations.....	48
4.2.5 Noise and Record Length	50
Chapter 5: Methods & Results – Stimulus Response System (SRS)	54
5.1 Methods: Stimulus Response System	54
5.1.1 SRS Simulation Model	54
5.1.2 Input Signals.....	57
5.1.3 Model Identification.....	59
5.2 Results: Stimulus Response System	59
5.2.1 Simulation and Identification with PRBS Inputs	59
5.2.2 Simulation and Identification with “Physiological” Inputs	61
5.2.3 Model Validation.....	65
5.2.4 Input Signal Limitations.....	69
5.2.5 Noise and Record Length	70
Chapter 6: Methods & Results - Facial Reanimation Control System.....	73
6.1 Methods: Facial Reanimation Control System.....	73
7.1.1 Estimating the Inverse of the Stimulus Response System (SRS^{-1})	75
7.1.2 Facial Reanimation Control System Output.....	76
6.2 Results: Facial Reanimation Control System.....	76
6.2.1 Estimating the Inverse of the Stimulus Response System (SRS^{-1})	78
6.2.2 Facial Reanimation Control System Output.....	80
Chapter 7: Discussion & Conclusion	84
References	89

Acknowledgments

I owe a dept of gratitude to my primary supervisor, Dr. Robert Kearney, for his guidance and time over the past two years. Not only has Dr. Kearney been my primary supervisor, but he was also my professor in several graduate classes that provided me with the necessary background knowledge. His expertise in biomedical system identification was crucial in completing this thesis. Dr. Kearney was also the primary editor, whose critical review improved the overall quality of the thesis.

I would also like to acknowledge Dr. Nate Jowett as part of the overall research program: Surgical and Rehabilitative Management of Facial Nerve Injury. As a head and neck surgeon, Dr. Jowett's work is focused on improving the therapeutic treatments of facial paralysis. His first-hand experience working with patients suffering from facial paralysis provided valuable background knowledge of facial paralysis, current treatments, and the limitations of these treatments. Dr. Jowett was also leading the design and execution of experimental trials with rat models prior to Covid-19.

This thesis was supported by the Natural Sciences and Engineering Research Council of Canada (NSERC) through a research grant (RGPIN-2019-04624) and the National Institute of Neurological Disorder and Stroke (NINDS) of the U.S. NIH through a R-01 grant (5R01NS071067-09).

Contribution of Authors

I was the sole author of this Master's thesis. I performed the necessary background research and analyzed the data in MATLAB. In addition to expertise in biomedical system identification, Dr. Robert Kearney critically reviewed the thesis and provided guidance on research, data analysis, and writing.

Chapter 1: Introduction

Facial palsy is a condition that involves weakness of the facial muscles, mainly resulting from temporary or permanent damage to the facial nerve. When the facial nerve does not function properly or is missing, the facial muscles do not receive the input signals needed for correct function. Causes of facial palsy include Bell's palsy, neurological conditions, traumatic injury, and stroke. Facial palsy diminishes the quality of life in many dimensions. It often impairs blinking, and can lead to other functional, esthetic, communication, and psychological issues [2, 3]. There are many reanimation techniques to restore function. These are chosen based on the cause of the injury, but dynamic procedures that attempt to restore some voluntary movement are the most desirable. Dynamic reanimation in hemi-facial paralysis is generally limited to smile restoration by nerve or functional muscle transfers. Even when the smile is reanimated it is often through motor tracts intended for other functions. Therefore, smiling can require a conscious bite effort and does not occur spontaneously [4]. Efforts to reanimate other facial regions including brow elevation, blink, and lip pucker have achieved only limited results. The largest obstacle to effective facial reanimation in facial palsy has been a lack of effective mechanisms to activate and control denervated or aberrantly re-innervated facial muscles [4]. Recent advances in technology have led to improved techniques in signal processing, implantable electrodes, and control methods for prosthetic limbs. These improvements have made techniques such as facial pacing feasible. Facial pacing is a technique proposed to restore the symmetry of facial movement which has been lost due to unilateral facial palsy [5]. The main idea of facial pacing is to measure the muscle activity from the healthy side with electromyography (EMG) and use this to activate the muscles on the paralyzed side through functional electrical stimulation (FES).

This Master's thesis project is part of a larger research program entitled: Surgical and Rehabilitative Management of Facial Nerve Injury. The program is supported through an NIH grant and is a collaboration between the Kearney laboratory at McGill University and Dr. Nate Jowett and his team at Massachusetts General Hospital. Dr. Nate Jowett is a head and neck surgeon specializing in facial plastic and reconstructive surgery. His work is devoted to improving therapeutic treatments for patients experiencing facial paralysis. The goal of the research is to

design a device that will address clinical facial paralysis resulting from the absence or damage to the facial nerve. The approach is to use functional electrical stimulation driven from the contralateral, healthy facial muscle activity to dynamically reanimate the unilateral facial paralysis. Conductive polymer electrodes (CPEs) will record EMG from the healthy side facial musculature. This will be the input to a signal acquisition and generator platform where digital signal processing algorithms will determine the concordant output stimulatory signals to distal nerve branches via implantable nerve cuff electrodes (NCEs) on the paralyzed side. The goal of reanimation is to restore the main symmetrical facial movements (brow elevation, blink, and smile). This would significantly improve the patient's wellbeing. If successful, this project would drastically improve the acute and long-term management of facial paralysis.

This thesis focuses on the models required for the signal acquisition and generator platform. The goal was to create a facial reanimation control system that takes EMG as input and produces the stimulus required for synchronized movement on the paralyzed side. Due to Covid-19, there was a lack of experimental data and we had to rely on simulated data to identify our models. As such, simulation models were developed that represent the healthy and paralyzed sides of the face. These simulation models used desired displacement inputs to generate simulated output signals: EMG and output displacement for the healthy side model, and output displacement for the paralyzed side model. With the models completed, we were able to generate data to:

1. Develop and validate a model to predict movement from an EMG input,
2. Develop and validate a model to predict movement from a stimulus input,
3. Combine these models together to demonstrate how the facial reanimation control system would work in practice.

The methods and results of building and evaluating the healthy side model, paralyzed side model, and the resulting facial reanimation control system are covered in Chapters 4, 5, and 6, respectively. Results indicate that the control system produces a predicted paralyzed displacement that consistently achieves a high variance accounted for when compared to the healthy displacement. Overall, the results are promising, as they demonstrate the feasibility of

Simulation Studies of Functional Electrical Stimulation for Facial Reanimation
Patrick Brebner

implementing the same system with experimental data in the proposed facial reanimation device.

Chapter 2: Background

This section covers the background, relevant biology, and modeling history related to the implementation of a facial reanimation device. A brief description of motor unit physiology, muscle behavior, and functional electrical stimulation is followed by a discussion of what is required of a muscle model.

2.1 Motor Unit Physiology

Most muscle models are based on the understanding of the underlying physiology of muscles. This section reviews two components of a motor unit: the motor neuron, and the muscle fibers it innervates. Understanding these concepts is essential to understand how it can be controlled.

2.1.1 Motor Neuron

Any action requires coordinating the movements of the body.

This is accomplished through the interaction of the nervous system with muscle. The role of the nervous system is to determine the correct muscles to activate and how much to activate them to produce the required force. When a movement is required, the central nervous system (CNS), that includes the brain and spinal cord, sends signals from motor neurons in the spinal cord to the muscle fibers. A typical muscle is controlled by hundreds of motor neurons whose cell bodies are clustered in a motor nucleus in the spinal cord or brain stem [1]. These motor neurons are often called lower motor neurons and are the final common pathway for transmitting neural information from the CNS to the skeletal muscles.

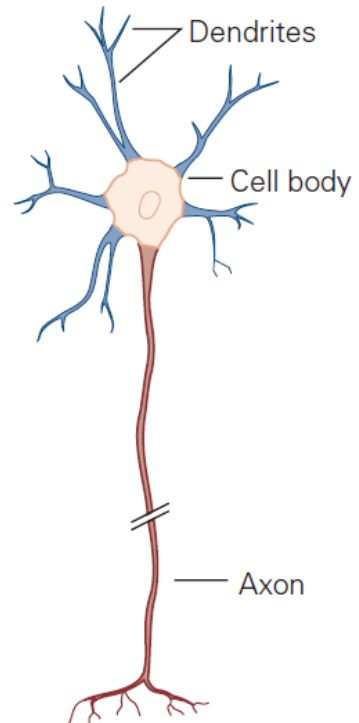


Figure 2-1: Motor Neuron Anatomy [1] (pg. 25).

Fig. 2-1 shows a typical motor neuron that is made up of a cell body, a long axon, and branching dendrites coming off the cell body. The connection between the transmitting axon of one neuron to the receiving dendrites of another neuron or the motor endplate of muscle fibers is called a synapse. When the muscle is to be contracted an action potential travels along the motor neuron towards the neuron-muscle synapse. When the action potential reaches the synapse, neurotransmitters (acetylcholine in this case) are released that bind to receptors of the

muscle fiber endplate. The acetylcholine causes an influx of sodium through the activated acetylcholine receptors. This leads to depolarization, where the muscle fiber endplate becomes more electropositive. If this electrical potential reaches a threshold, an action potential will propagate across the muscle fiber and leads to a muscle contraction.

A single motor neuron axon connects to many muscle fibers, but each muscle fiber is only innervated by a single axon. The motor neuron and all the muscle fibers that it innervates is called a motor unit [1].

2.1.2 Muscle Fibers

Skeletal muscle is composed of bundles of long, thin cells called muscle fibers. Fig. 2-2 shows the anatomy of a muscle fiber. Muscle fibers are made up of clusters of sarcomeres, that form a contractile unit. Sarcomeres have three main components: actin filaments, thick myosin filaments, and Z-disks which define the length of the sarcomere. An action potential propagating along a muscle fiber causes calcium ions to be released by the sarcoplasmic reticulum. These ions bond to part of the actin filament which leads to a transformation of the actin filament that exposes bonding sites for myosin. Once these sites are exposed, the heads on the myosin filaments attach to the actin filament forming structures called cross-bridges. Through a process called the cross-bridge power stroke, the myosin heads pull on the actin filaments which shortens the sarcomere and results in contraction of the muscle. After the power stroke, adenosine triphosphate (ATP) is used to release the bonds between the myosin and actin filament and return to a position ready for the next power stroke [1].

Simulation Studies of Functional Electrical Stimulation for Facial Reanimation
Patrick Brebner

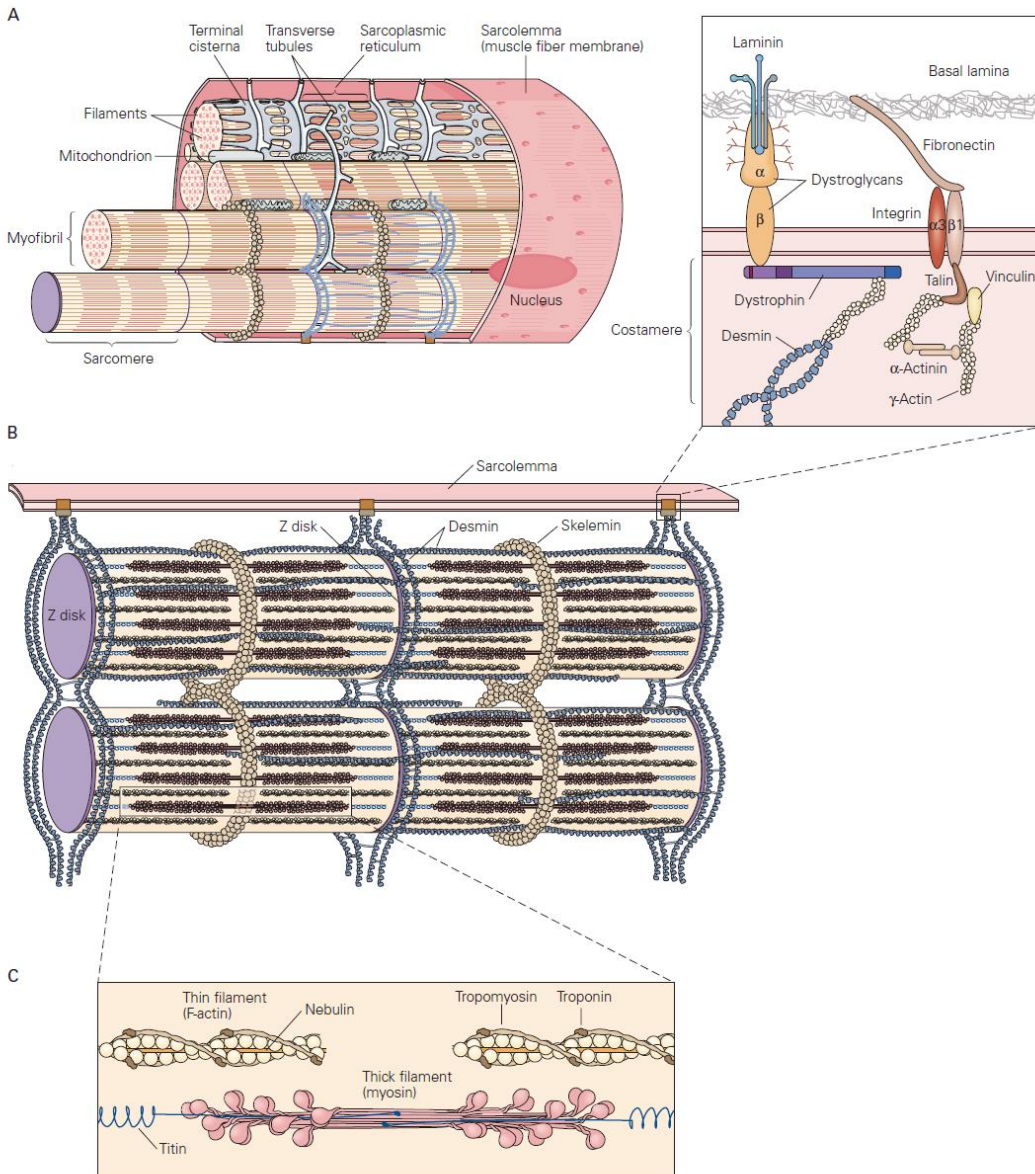


Figure 2-2: Muscle Fiber Anatomy [1] (pg. 778).

Muscle fibers can either be fast-twitch or slow-twitch fibers. Slow-twitch muscle fibers are fatigue resistant and are focused on sustained smaller movement and postural control. They contain more mitochondria and myoglobin and are aerobic in nature. Slow-twitch fibers are sometimes called red fibers because of their blood supply. In contrast, fast-twitch muscle fibers produce larger forces quickly, but last for shorter durations and fatigue quickly. They are more anaerobic with less blood supply and have a white appearance. This means that slow-twitch fibers are used for endurance activities like marathon running, while fast-twitch muscle fibers are

used in quick, powerful movements like sprinting. The fiber composition of muscle varies and may need to be considered when modeling a certain muscle [1].

2.2 Muscle Behavior

The microscopic behavior discussed in the last section leads to muscle's macroscopic behavior. This section details four specific behaviors and traits of muscles during contraction: force summation, muscle recruitment, force-length and force-velocity relationships, and feedback mechanisms. All four influence the production and/or control of muscle force and must be considered when modeling the system.

2.2.1 Force Summation

During a muscle contraction, a single action potential causes a muscle twitch. A single muscle twitch generally does not produce much force and decays quickly. That is because the amount of calcium released due to a single action potential does not create many cross-bridges. When action potential frequency increases to the point that the muscle twitches overlap, they begin to summate, and the muscle goes into a state of unfused tetanus. Finally, when the calcium ions are released at a rate higher than the rate of reuptake, a fused tetanus occurs [1]. In a fused tetanus, the force produced is more constant and is sustained. Fig. 2-3 shows the effects of force summation for slow and fast twitch muscle fibers. When a larger and sustained muscle force is required there will be more action potentials from the motor neuron. However, there is a limit to the amount of force that a single motor unit can produce and increasing the action potential frequency past this point has no effect. It is however possible to generate higher forces by contracting additional motor units. This is called muscle recruitment and is covered in the next section.

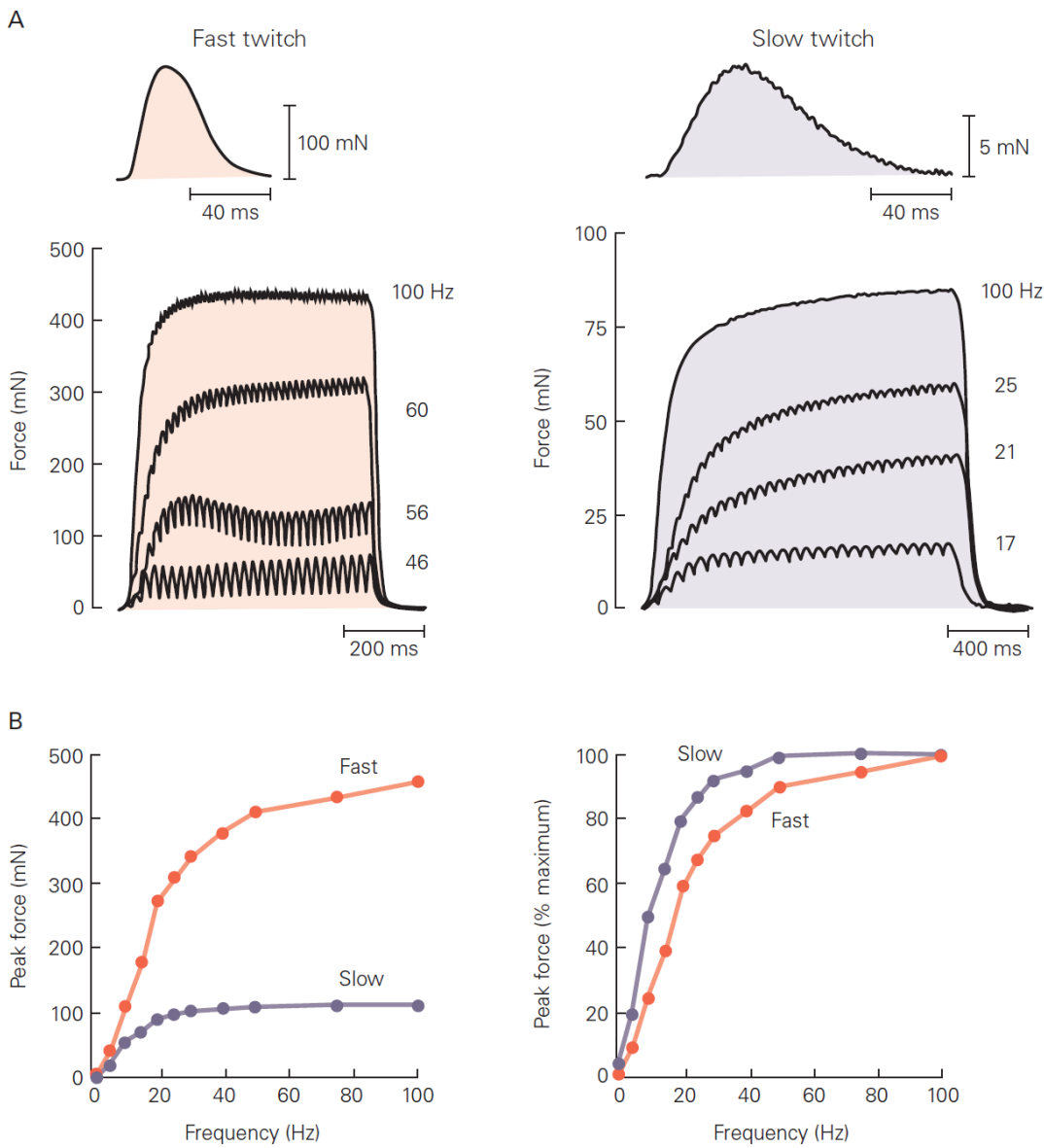


Figure 2-3: Force Summation of Fast Twitch and Slow Twitch Muscle Fibers; A) Traces show the forces exerted by fast and slow twitch motor units in response to a single action potential (top) and a series of action potentials at different frequencies (four traces below); B) Relation between peak force and rate of action potentials for fast and slow twitch motor units [1] (pg. 771).

2.2.2 Muscle Recruitment

A single motor unit is only able to produce a limited amount of force. To generate larger forces, multiple motor units must be recruited. Motor unit recruitment starts with the smallest motor neurons and gradually increases to the larger ones. This is known as Henneman's principle, which means slow-twitch fibers are recruited before the fast-twitch fibers [6]. As discussed previously, muscle fibers can either be fast-twitch or slow-twitch but a motor unit will comprise fibers of only

one type. If an endurance movement is required, such as marathon running or postural control, the force requirement is relatively low and only small fatigue resistant slow-twitch fibers will be stimulated. Fig. 2-3 shows that these fibers slowly contract, produce low forces, but can be sustained for a long period. If a powerful or fast movement is required, such as sprinting or weightlifting, the force requirement is much higher and larger, fatigue prone fast-twitch fibers will also be stimulated. Fig. 2-3 shows that these fibers contract faster, produce more force, but the force cannot be sustained for as long as slow-twitch fibers. This natural order of recruitment is crucial for proper function of movement. Unfortunately, this natural order of recruitment is not maintained during functional electrical stimulation as will be discussed further below.

2.2.3 Force-Length and Force-Velocity Relationship

The two previous sections described the main ways that force is produced and controlled. However, they are not the only factors that affect the force output. The amount of force produced depends on the length of the muscle as well as its velocity of contraction. Essentially, a muscle with changing length behaves differently than a muscle of fixed length (isometric contraction).

The force produced by a muscle depends on its length and velocity. The force-length and force-velocity relationship act independently on the muscle force and both relationships are based on the behavior of the sarcomeres during contraction. As the actin and myosin filaments slide past each other there is a position when the overlapping area is at a maximum. At this point there is the most actin and myosin interaction, which permits the most cross-bridges to form, so the muscle can produce its maximum force. At longer or shorter lengths fewer cross-bridges can form so the maximum force that can be generated is less [1]. Fig. 2-4 shows this effect.

Simulation Studies of Functional Electrical Stimulation for Facial Reanimation
Patrick Brebner

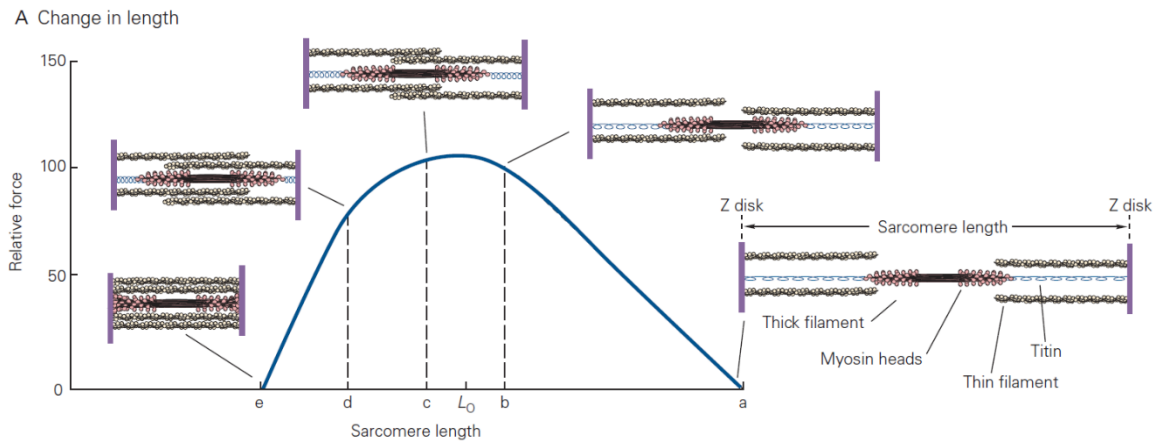


Figure 2-4: Force-Length Relationship; At an intermediate length, the amount of overlap between actin and myosin is optimal and the relative force is maximal. When the sarcomere is stretched beyond the point of overlap (length a), cross bridges cannot form and no force is exerted. When the length is reduced well below optimal (between length d and e), the extreme overlap of the thin filaments with each other occludes potential cross-bridge forming sites and the force decreases. [1] (pg. 781).

Fig. 2-5 shows that the force produced during contraction varies with the rate of change in sarcomere length. The peak force declines as the rate of shortening increases while the peak force increases while the rate of sarcomere lengthening increases. Shortening of the sarcomere causes the myosin heads to spend more time near the end of the power stroke, where they produce less contractile force, and spend more time detaching, repositioning (recocking), and reattaching. In contrast, during lengthening, the myosin heads spend more time being stretched beyond their angle of attachment and less time unattached because they do not need to be recocked after being pulled away in this manner [1].

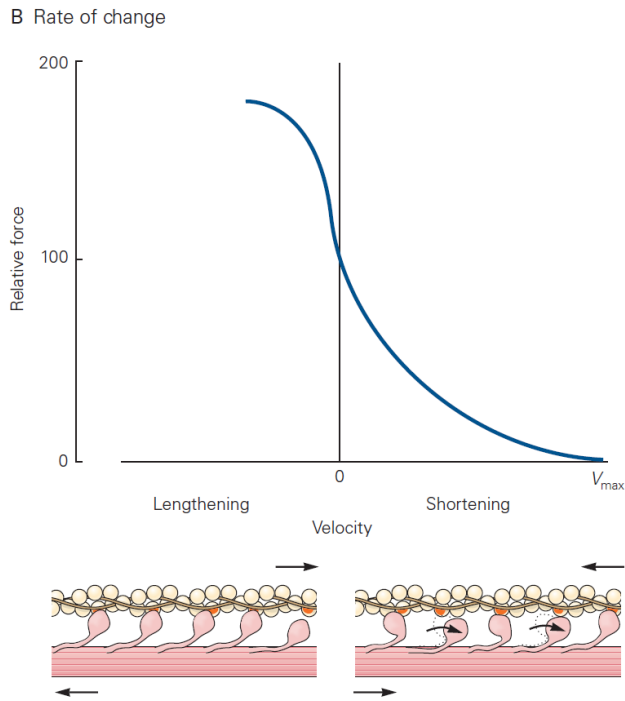


Figure 2-5: Force-Velocity Relationship; Contractile force varies with the rate of change in sarcomere length. Relative to the force that a sarcomere can exert during an isometric contraction (zero velocity), the peak force declines as the rate of shortening increases. In contrast, when the sarcomere is lengthened while being activated, the peak force increases to values greater than those during an isometric contraction. [1] (pg. 781).

2.2.4 Muscle Feedback

There are several feedback mechanisms in motor function that help control movement, regulate strain on the muscle-tendon unit and prevent injury. The two sensory organs directly related to muscle contraction dynamics are the muscle spindle endings and the Golgi tendon organs. The spindle endings sense muscle length and strain rate while the Golgi tendon organs sense tension. Proper function of these sensory organs are key to proper movement as dysfunction can cause spasticity and oscillatory tremors [7].

2.3 Functional Electrical Stimulation

Functional electrical stimulation (FES) is a technique that uses electrical pulses to stimulate muscle to produce a desired movement. FES is very useful for generating muscle contraction in otherwise paralyzed limbs to produce, or assist, movements such as grasping and walking. This usefulness has led to a ramp up of research in the field of neuroprosthetics and functional electrical stimulation. FES is used in cases when the muscle is still intact, but the neural activation is impaired by nervous tissue damage from either trauma or disease. This technology can be used

in neuroprosthetics to permanently substitute impaired functions in individuals with spinal cord injury or stroke. In clinical settings, electrical stimulation can be used for improving strength, increasing range of motion, reducing edema, decreasing atrophy, healing tissue, and decreasing pain [8]. To be functional, the electrical stimulation needs to activate muscle predictably and reliably while also being tolerable in terms of discomfort experienced by the patient.

In FES, frequency refers to the number of pulses applied per second and is measured in Hertz (Hz). Depending on the task, the stimulation frequency is usually between 20 – 50 Hz [9]. Higher frequencies are reported to be more comfortable since the force output is smoother, whereas lower frequencies are more noticeable since they evoke a tapping-like sensation with each stimulus pulse [10]. To avoid muscle fatigue, constant low frequency stimulation is often used because it produces a smooth contraction at low force [11]. Amplitude is another parameter that must be adjusted depending on the requirements of electrical stimulation. The higher the amplitude, the stronger the depolarizing effect on the structure stimulated by the electrode [12]. A higher amplitude activates more muscle fibers which leads to a larger contraction. However, the intensity of the stimulation will effect patient comfort since high amplitude signals are less tolerated and can stimulate pain sensing nociceptors [13]. Overall, the frequency and amplitude of the electrical stimulation will determine the quality of the muscle contraction.

The pulse width and waveform type are two other parameters that need to be determined. The length of a single pulse is known as the pulse width. It has been shown that wider pulse widths produce stronger contractions [14]. In addition, longer pulse widths generally penetrate more deeply into the subcutaneous tissues [15]. Electrical stimulation devices deliver pulses in waveforms patterns that are usually represented by geometric shapes such as square, triangle, or sine wave. In a recent study, the frontalis facial muscle was electrically stimulated with four different waveforms to investigate their effects on muscle activation, comfort and discomfort. The waveforms investigated were square, square wavelet, sine, and sine wavelet. Other than some personal preferences, there were no significant differences between waveforms for producing movement or the individuals' comfort [16].

On top of the improved functionality there are other benefits from FES treatment. FES has been proven to strengthen muscle [17], enhance circulation and blood flow [18, 19], reduce pain [20], heal tissue [21], reduce spasticity [22], and slow the rate of muscle atrophy [23]. Although not the main target, electrical stimulation also stimulates sensory fibers which can lead to improvements in sensation and tactile awareness [24]. Finally, there can be a psychological benefit for the patient in seeing/experiencing the movement caused by a FES system in a previously paralyzed body part [25]. The patient may feel more confident and motivated by regaining functional movement. As facial paralysis is such a visually obvious impairment, this benefit is likely to occur.

Although FES has many benefits it still has some limitations that must be addressed. Most importantly, FES can induce excessive neuromuscular fatigue. There are two main reasons for this. First, electrical stimulation alters the normal motor unit recruitment order [26]. Physiologically, the smaller, fatigue resistant motor neurons are activated first. These motor units are essential for any long duration task. The order of motor unit recruitment during electrical stimulation is flipped, which reduces this natural fatigue resistance [27]. Second, during electrical stimulation muscle fibers are stimulated synchronously. This is unlike the normal and highly effective recruitment and de-recruitment process of motor units. During these contractions the motor system reduces fatigue by increasing the firing rate of active motor units and/or recruiting new motor units to replace others that have succumbed to fatigue [28].

2.4 Muscle Modeling

To properly control a muscle, a FES system requires a working model of the muscle to be controlled. During muscle contraction, a signal called an electromyogram is produced. The relationship between the electromyogram, neural input, and muscle force can be used to model the system in a variety of ways.

2.4.1 Electromyogram

As previously discussed, during muscle contraction there is an electrical depolarization in the form of propagating action potentials caused by an influx of calcium ions into the muscle fiber. This electrical depolarization can be detected with electrodes placed on the surface of the skin or inserted into the muscle. The resulting signal, called the electromyogram (EMG), provides a

measure of the muscle's activation in response to neural input. EMG is commonly used in motor control research, prosthetics, rehabilitation, and biomechanics. EMG is detected using either surface or intramuscular electrodes. Surface electrodes are the easiest to apply since they are non-invasive, and they record from a significant portion of the muscle. However, they can only detect activity from superficial muscles. Their lack of selectivity means that cross-talk – the detection of signals from unwanted sources can be a problem. Intramuscular electrodes can be further split into needle electrodes and wire electrodes, both of which record from the muscular tissue. Needle electrodes are not surgically attached so they can be repositioned easily but, as a result, are sensitive to movement. Wire electrodes may be surgically attached to provide stable, selective EMG recordings for long term recordings where significant movement occurs. These features are important for a rat model of facial palsy when consistent recordings from the same muscle tissue are desired for multiple trials. However, since they cannot be repositioned, special care must be taken to ensure they are attached in the correct location.

Tissue filtering and electrode pick-up area are two things that must be considered when choosing the electrode type and attachment location for measuring EMG. Tissue between the muscle of interest and the electrode will act as a low pass filter that increases with distance. Finally, the electrode pick-up area is the area of EMG detection. This area is limited since there is a voltage gradient in muscle and the surrounding tissue that decrease rapidly as distance from the contracting muscle increases. Surface electrodes generally detect activity from a significant portion of the muscle while wire electrodes are much more selective.

With the electrodes selected and in place, EMG signal processing is the essential next step. EMG signal processing usually involves a differential preamplifier, a high pass filter, a gain, a detector, and a low pass filter. The high pass filter, with a usual cut-off frequency between 10 – 100 Hz, is used to reject low frequency content that may contain artifacts such as DC polarization of the electrodes and motion artifacts. The gain amplifies signals to levels compatible with recording. This is necessary since EMG amplitude is quite small with typical ranges in the millivolt or microvolt range. The detector is typically a full wave rectifier since it is easy to implement. Finally, the low pass filter is used to reduce variance. This creates a tradeoff between

variance and temporal resolution with a high cut-off frequency resulting in a rapid response and large variance while a low cut-off frequency results in a slow response and low variance.

In some cases, it is necessary to simulate an EMG signal to explore the relationship between muscle structure and activation. As previously discussed, each group of muscle fibers is controlled by one motor neuron which together forms a motor unit. The contraction of a muscle is proceeded by a depolarization that propagates along the muscle fiber. This wave of depolarization creates an electrical field in the extracellular medium around the muscle fibers. These electrical fields, when detected by a suitable electrode, and the resulting voltage waveform is called a muscle fiber action potential. Since all the muscle fibers of a motor unit are activated simultaneously, detected waveforms are determined by contributions from all the muscle fibers of a motor unit and are termed motor unit action potentials (MUAP). Fig. 2-6 demonstrates this behavior. Assuming the detection set-up is consistent, a MUAP has the same waveform every time the motor unit is activated.

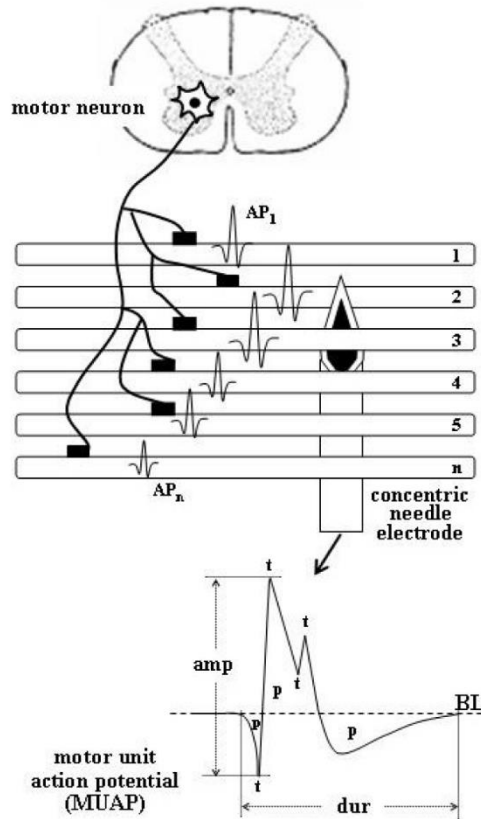


Figure 2-6: Schematic Representation of Motor Unit with Muscle Fibers; The motor unit contains n muscle fibers, each of which produces a muscle fiber action potential, AP_n , that when combined produce the motor unit action potential (MUAP). The parameters of the MUAP waveform in this figure: amp = amplitude, dur = duration, p = phase, t = turn, BL = baseline [29].

The repeated discharge of a motor neuron results in a train of MUAPs. When a muscle contracts, numerous motor neurons will be active and the EMG signal detected is the summation of all the MUAP trains. Depending on the contracting muscle, the number of detected motor units may range from tens to hundreds [30, 31]. Based on this, if the individual muscle fiber action potentials that contribute to the MUAPs can be modeled along with firing times of individual motor units, the EMG signal can be simulated [32]. This type of EMG simulation requires knowledge of the muscle fiber positions relative to the detecting electrode, the distribution of muscle fibers among the motor units of a muscle, and the firing times of individual motor units [32, 33]. The benefit of this type of simulation is that the effects of motor unit morphology and activation can be analyzed at the fiber, motor unit and muscle level [33]. A simpler way to simulate recorded EMG is as the summation of MUAPs multiplied by the discharge impulses with added zero mean white noise over all active motor units [34]. Equation 2-1 shows that the EMG

signal, $x(t)$, can be modeled as the sum of trains of motor unit action potentials $m_i(t)$, each of which can be defined as the time convolution between motor neuron discharge impulses $\delta_i(t - t_{ij})$ and the waveform $s_i(t)$ of the MUAP [35].

$$x(t) = \sum_i^N m_i(t) = \sum_i^N \sum_j^{M_i} \delta(t - t_{ij}) * s_i(t)$$

Equation 2-1: Simple EMG Model [35].

Where N and M_i correspond to the number of motor units and the total number of discharge impulses ($j = 1, 2, 3, \dots, M_i$) for the i -th motor unit, respectively. This approach is further illustrated in Fig. 2-7 where the EMG signal, $x(t)$, is combined with noise, $e(t)$, before passing through the transfer function $H(f)$ of the EMG recording apparatus. The output, $g(t)$, is the EMG at the surface of recording and is what would be available for analysis [35].

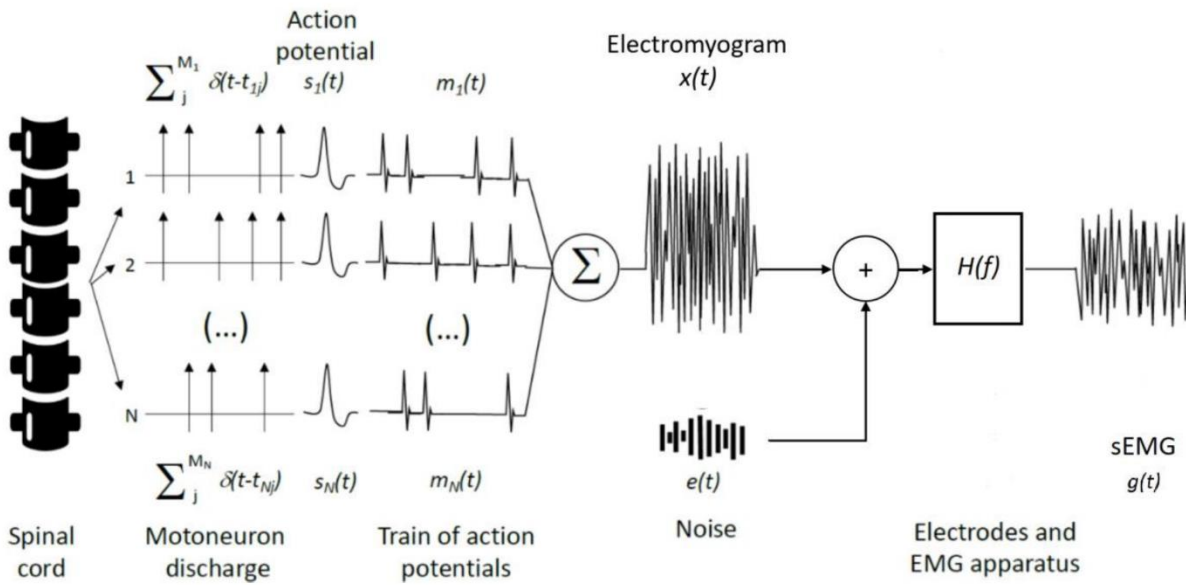


Figure 2-7: Schematic Representation of the Generation of EMG from Motor Unit Action Potentials (MUAPs); $g(t)$ is the recorded EMG signal that would be available for analyses, $e(t)$ is additive noise, and $H(f)$ is the transfer function of the recording apparatus [35].

2.4.3 Muscle Activation and Contraction Dynamics

The main mechanisms of muscle force generation are activation dynamics and contraction dynamics [36]. With these both modeled, an accurate and reproducible prediction of muscle forces can be predicted from EMG. Muscle contraction dynamics describe the mechanical

properties of muscle tissue and tendons. These are generally expressed as the force-length and force-velocity relationships discussed previously. Muscle activation dynamics include the voluntary and non-voluntary excitation signals and motor unit recruitment level in the muscle [36]. To transform EMG into muscle activation the first step is to remove any DC offsets or low frequency noise by high pass filtering the EMG signal. Once filtered, the signal's absolute value is taken, resulting in a rectified EMG signal. Finally, to get muscle force, the rectified EMG signals is low pass filtered because the muscle activation acts as a filter. Even though the electrical signal that passes through the muscle has frequencies above 100 Hz, the force that the muscle generates is at a much lower frequency [37]. Mechanisms that can cause this filtering includes calcium dynamics, finite amount of time for transmission of muscle action potentials along the muscle, and muscle-tendon viscoelasticity. The cut-off frequency for this last filter typically is in the range of 2 Hz – 10 Hz [37].

2.4.4 Categories of Muscle Models

Muscle models come in many varieties but generally can be split into three categories: Huxley-based biophysical models, Hill-type models, and nonparametric mathematical models [38]. Each model type has its advantages and disadvantages and makes different assumptions about the system.

Hill-type models are popular due to their relative simplicity and accuracy at modeling the system. The Hill-type model usually consists of masses, springs, dampers, and contractile elements [39]. One benefit of Hill-type models is that they can easily incorporate the force-length and force-velocity relationships [37]. However, these models are based on the output behavior and make no reference to the well understood cross-bridge mechanics causing this behavior.

Huxley-based biophysical models are the most complex as they incorporate the microscopic muscle behavior of muscle to model the macroscopic behavior [37]. They explore the chemical reactions required for myosin head attachment. Calcium ion concentration tends to be the most common independent variable as it effects the formation of cross-bridges [1]. The complexity of these models means they can provide good descriptors of the muscle contractile dynamics. Unfortunately, this complexity makes these types of models unusable for control due to their high computationally requirements [37].

Finally, there are nonparametric mathematical models, which are often considered non-physiological because they are often free of any physical meaning. This makes it difficult to gather any intuition about the system for understanding or modeling purposes. Nonparametric mathematical models can either be linear or non-linear. The advantage of linear models is the simplicity, but this comes at a cost as they often struggle to represent the non-linear behavior of muscle. Non-linear models can capture all these non-linear muscle behaviors. When choosing the type of model for your system it is important to consider the model complexity. Too many parameters in a model can lead to overfitting and it's generally better to keep the model as simple as possible [37]. The models used for this thesis fall into this last category, due to their advantages in computational efficiency, and are based around Hammerstein cascade models.

2.4.5 Hammerstein Models

The activation dynamics discussed above capture the active properties of the muscle and are almost uniformly represented by a Hammerstein model structure [40]. The Hammerstein model is a block structure comprising a static nonlinearity followed by a linear dynamic element. The benefits of breaking the system into blocks is that the individual blocks may correspond to different natural phenomena which can lead to a better understanding of the system. As early as 1967, the Hammerstein model was used to describe muscle behavior [41]. The widespread use of the Hammerstein model for activation dynamics is due to its correspondence with biophysics: the static nonlinearity represents the isometric recruitment curve (IRC); the static gain relation between stimulus activation level and steady-state output torque when the muscle is held at a fixed length. The linear dynamics represent the muscle contraction dynamics, which combined with the IRC gives the overall torque generated [40].

Chapter 3: Literature Review

With the general background covered, we can now take a deeper look at the current state of facial reanimation. This section provides an overview of hemi-facial palsy, current treatments, and their limitations. It concludes with a survey of the history of the development of facial reanimation devices that use facial pacing and provides the rationale for this thesis.

3.1 Facial Palsy

Facial palsy is a condition that involves weakness of the facial muscles, mainly resulting from temporary or permanent damage to cranial nerve VII (facial nerve) on one side of the face. The facial nerve and associated musculature are integral to blinking, support of nasal breathing, oral phase of eating, speech production, and emotional expression [42]. When the facial nerve does not function properly or is missing, the facial muscles do not receive the input signals needed for correct function. Causes of facial palsy include Bell's palsy, neurological conditions, Lyme disease, otic infections, post-surgical insult, tumors, traumatic injury, and stroke [43]. Bell's palsy, the most common cause of facial paralysis, occurs with a lifetime incidence of one in sixty and an annual incidence of 15-30 per 100,000 population [44-46]. Luckily, about 85% of Bell's palsy patients improve within 3 weeks of onset; most individuals either regain normal function or have only mild residual facial weakness [44].

The symptoms of facial palsy can vary from person to person and range in severity from mild weakness to total paralysis. In more severe cases, facial palsy goes beyond just a cosmetic disfigurement and can diminish the quality of life in many dimensions and lead to permanent disabilities. When acquired, the insult to the facial nerve typically induces acute flaccid facial palsy (FFP). In the flaccid state, absence of frontalis muscle function results in ptosis of the brow that obscures vision [47]. Without the ability to blink, vision loss may occur due to damage from corneal dryness [48]. Nasal obstruction and mouth leakage result from an inability to keep nasal passages open and mouth closed [49]. Dysarthria and distorted facial expressions negatively affect both spoken and non-verbal communications [2]. Finally, individuals may experience facial pain, altered taste, and intolerance to loud noises [44].

In contrast to neurons of the central nervous system, lower motor neurons retain capacity for regeneration of their axonal processes. Depending on the severity of the facial nerve damage and therapeutic intervention, recovery of functional movement may be complete, absent, or disordered, resulting in a movement disorder known as post-paralytic facial palsy (PPFP) [50]. PPFP includes facial muscle hypertonicity and synkinesis caused by disordered or aberrant regeneration of motor neurons following high grade facial nerve insult. Facial synkinesis is abnormal or involuntary activation of facial muscles with voluntary or spontaneous expression. Fig. 3-1 shows that the ultimate clinical course of facial palsy can yield either FFP, PPFP, or a combination of the two [4].



Figure 3-1: Hemifacial Palsy; (left) Left-sided flaccid facial palsy (FFP), (right) Left-sided post-paralytic facial palsy (PPFP) as a result of aberrant regeneration of the facial nerve following high-grade insult [4].

3.2 Current Treatments

The goal of current facial palsy treatments is to restore muscle tone and function, social interaction, and quality of life. In general, the treatment timeline can vary depending on the specific case, the cause of the facial palsy and the physician. As such, the procedures and timelines outlined below provide a general idea of what occurs but might not necessarily cover all scenarios.

It is incumbent upon the treating clinician to establish a diagnosis for the underlying cause of facial palsy. There are many possible causes of facial palsy, often needing different treatment

methods. To determine the correct course, it is useful to classify the cases of facial palsy into five management domains based on timing and status of the facial nerve and musculature. These five categories include: acute FFP, FFP with potential for spontaneous recovery, FFP with viable facial musculature and low potential for spontaneous recovery, FFP without viable facial musculature, and PPFP [47]. Therapeutic intervention may include pharmaceutical agents, corneal protective measures, physical therapy, chemo-denervation agents, fillers, and a myriad of surgical procedures [47].

In cases where the nerve continuity is believed to be intact, the patient might be categorized as FFP with potential for spontaneous recovery. Facial tone and movement are expected to return within 6-12 months and patients will likely benefit from physical therapy, corneal protective measures, and selective chemo-denervation [47].

If there is no sign of recovery after 6-12 months or the patient was categorized as having low potential for spontaneous recovery and/or unviable facial musculature, surgery may be considered in the form of nerve grafts/transfers. These dynamic procedures routinely take 9-18 months to become effective and require rigorous rehabilitation [51]. Three of the most common dynamic reanimation procedures are cross-facial nerve grafts, hypoglossal nerve transfers and masseteric nerve transfers [42].

The cross-facial nerve graft uses the opposite, viable facial nerve to power the affected paralyzed side. The nerve graft is usually harvested from the sural nerve in the lower leg. This sensory nerve is used because it is long and using it for grafting purposes has little downside on lower leg function. The nerve graft is attached to the facial nerve on the healthy side and then is tunneled underneath the skin and above the upper lip to be connected to the same nerve branch on the paralyzed side. Nerve regeneration is slow (1mm/day), so a cross nerve graft can take up to 9 months to reach the paralyzed side of the face [42]. The benefits of this procedure are that it can create truly spontaneous, emotive movement. However, the results are variable. Sometimes all the axons do not make it across. Other pitfalls are weakening of the healthy side and a lack of power on the paralyzed side [52].

The hypoglossal nerve innervates muscles of the tongue. Hypoglossal nerve transfers to the main trunk of the facial nerve can restore adequate resting tone to the paralyzed face, however it does not restore symmetric movement [42]. Furthermore, this procedure is more challenging and is associated with significant patient morbidity. Ipsilateral tongue paralysis can develop leading to difficulties with speech and swallowing [13].

The masseteric nerve is stimulated during clenching of the teeth. Masseteric nerve transfers to branches of the facial nerve are a reliable technique for targeted smile restoration but lack spontaneity and resting tone. This procedure is seen as an improvement over the hypoglossal nerve transfer due to lower patient morbidity, ease of access to the nerve, and that the masseteric movement to elicit a smile (clenching teeth) has been suggested to be more natural than using tongue movement to elicit a smile [42, 53].

Finally, if surgery is delayed too much, or the initial surgeries are unsuccessful, the muscles on the paralyzed side can become unreceptive to neural stimulation. In adults, this occurs around 24 months after hemifacial palsy first occurs [47]. In this case, the surgical interventions include static facial suspensions and muscle transfers. A free muscle transfer is usually performed where the surgeon takes a small thin segment of a muscle from the inner thigh (gracilis muscle), moves it to the paralyzed side of the face and connects it to local nerves and blood vessels. It can then take 6 – 12 months before the muscle becomes active and contracts.

Overall, these existing strategies fail to adequately and reliably restore spontaneous facial function or natural emotional expression [4, 13]. The proposed neuroprosthetic device for facial reanimation will have some advantages over the procedures discussed above. Theoretically, the device should address the issues associated with the cross-facial nerve graft, the hypoglossal nerve transfer, and the masseteric nerve transfer. The facial reanimation device should be able to consistently produce symmetrical movements (including resting tone), with minimal patient morbidity, and without having to wait for months to see if the procedure was effective thus reducing the chance that the muscle on the paralyzed side becomes unreceptive to stimulus. Even in cases of long-term facial palsy, the device could be implanted during the free muscle transfer surgery to improve the outcome. Furthermore, the device will be able to address the

issue of any undesirable facial activity through the implementation of a high frequency alternating current (HFAC) as a neural blockade. Overall, the device will provide improved control and flexibility for addressing the condition of hemifacial palsy.

3.3 Facial Reanimation

Facial pacing is a facial reanimation technique proposed to restore the symmetry of facial movement which has been lost due to unilateral facial palsy [5]. The main idea of facial pacing is to measure the muscle activity from the healthy side with electromyography (EMG) and use this to activate the muscles on the paralyzed size through functional electrical stimulation (FES).

The idea of facial pacing has been around for a long time and there have been some promising results with regard to the techniques feasibility. In 1986, it was demonstrated that an electrical circuit could detect the voltages generated by facial muscle contraction and then trigger a corresponding stimulus in synchrony [54]. As discussed previously, a major issue with facial palsy is the inability to blink which can lead to damage of the eye and partial or complete blindness. Consequently, restoring the ability to blink was a focus of early facial pacing research. In 1997, it was demonstrated that a facial pacing device could restore normal appearing blinking in rabbits through functional electrical stimulation with no adverse after-effects [55]. These results supported the hypothesis that electrical stimulation could restore the function of paralyzed facial muscles. In a recent study using rats, Attiah et al. developed and tested a model of closed-loop FES based facial reanimation in the setting of unilateral facial palsy. This demonstrated that protraction of whiskers varied with stimulation parameters and that closed-loop, contralateral-triggered FES was feasible for human facial reanimation [13]. It was noted that there were two main limitations in the study. First, Attiah et al. had difficulty in finding a durable placement of electrodes in the intrinsic muscle. Due to the location and size of the muscles, the implantation location of electrodes varied and may have led to variable results. The second limitation was that muscle retraction was not actively controlled but accomplished through passive retraction. This was done because their experimental set-up could not accurately capture the whisker retraction movement [13]. More recently, Jowett et al. demonstrated a proof of principle for rehabilitation of hemifacial palsy using an implanted neuroprosthetic device [4]. Epimysial and nerve cuff electrodes were implanted in the faces of Wistar rats. The

relationship between the EMG and facial displacements was modeled and compared with measured displacements. The muscle was treated as a nonlinear system and the relationship between the EMG and muscle force was modeled as Hammerstein system, a static nonlinearity followed by a dynamic linear element. Overall, the implanted devices were well tolerated, and facial displacements were predicted with a variance accounted for exceeding 96% [4]. All these previous studies demonstrate that a facial reanimation device is feasible and would benefit those suffering from unilateral facial palsy. Recent advances in technology have opened the door for building a FES facial reanimation device. The benefits of FES, including maintaining muscle structure and even reversing atrophy, suggest that even a limited implant could restore some dynamic function and maintain muscle health in patients [56].

3.4 Rationale and Objective

Proper facial expression is necessary for social interactions [57, 58]. The disruption of this function, as is the case with facial palsy, can lead to many functional, esthetic, communication, and psychological problems [2, 3]. As the preceding review has shown, current treatments for facial palsy are lacking and yield limited results. Techniques that achieve functional reanimation are desirable but have been limited by the lack of effective control mechanisms for denervated or aberrantly re-innervated facial muscles. Recent advances in technology have made facial pacing feasible. Previous work has demonstrated that the facial reanimation device proposed in this thesis is feasible and could drastically improve the acute and long-term management of facial palsy.

In the proposed facial reanimation device, conductive polymer electrodes (CPEs) will record EMG from the healthy side facial musculature. This will be the input to a signal acquisition and generator platform (SAP) which will use a signal processing algorithm to determine the stimulus to be delivered to distal nerve branches via implantable nerve cuff electrodes (NCEs) on the paralyzed side. This functional electrical stimulation (FES) will be supplemented with a high frequency alternating current (HFAC) that will act as a neural blockade to stop any aberrant movements. Fig. 3-2 shows a schematic diagram of the facial reanimation device.

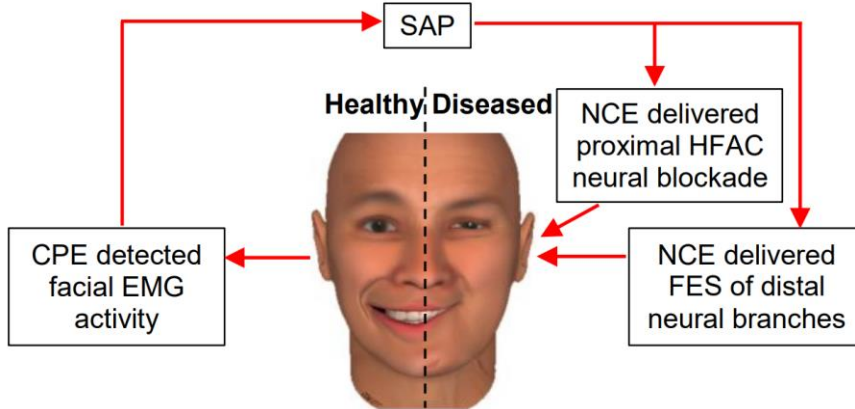


Figure 3-2: Schematic of the Proposed Facial Reanimation Device; Healthy side EMG is detected with conductive polymer electrodes (CPEs) and used as an input to a signal acquisition and generator platform (SAP). The SAP uses processing algorithms to determine the stimulus required to create symmetrical movement on the paralyzed side. Alongside a high frequency alternating current (HFAC), the stimulus is applied to the paralyzed side through nerve cuff electrodes (NCEs).

To build the signal processing algorithms, the relationship between EMG, stimulus, and muscle force in facial muscles must be modeled. Although the background information about muscle behavior is well known, the relationships of EMG, stimulus, and muscle force are less clear. These relationships must be modeled to develop a facial reanimation control system (FRCS). The FRCS can be thought of as the signal processing algorithms of the SAP that determine the stimulus required based on an EMG input. Developing and understanding these models will be a major step towards building the proposed facial reanimation device.

Fig. 3-3 shows that to build the FRCS the goal is to create an EMG response system (ERS) and a stimulus response system (SRS) that model the healthy and paralyzed sides of the face, respectively. The ERS models the relation between an EMG input, $E(t)$, and healthy displacement output, $Pos_H(t)$. The SRS models the relation between the stimulus amplitude modulation input, $A(t)$, and paralyzed displacement output, $Pos_P(t)$. The FRCS will include the ERS followed by the inverse of the SRS, SRS^{-1} , to model the relation between $E(t)$ from the healthy side and $A(t)$ to the paralyzed side. Since the goal of the FRCS is to have $Pos_P(t)$ equal $Pos_H(t)$, the SRS^{-1} switches the input and output of the SRS so that $Pos_H(t)$ is the input and $A(t)$ is the output. This Master's thesis project will use simulation to build and test these models.

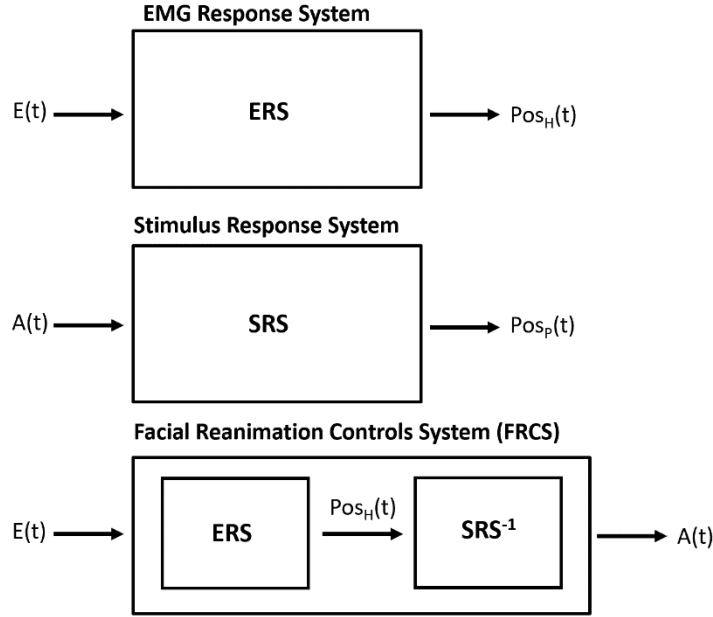


Figure 3-3: Proposed Models for Control of a Neuroprosthetic Device for Hemifacial Reanimation; (top) EMG response system (ERS): An input electromyography signal, $E(t)$, is modeled to an output displacement, $Pos_H(t)$, on the healthy side of the face. (center) Stimulus response system (SRS): An input stimulus amplitude modulation signal, $A(t)$, is modeled to the output paralyzed displacement, $Pos_P(t)$. (bottom) Facial reanimation control system (FRCS): By coupling the ERS with the SRS⁻¹, an $E(t)$ signal from the healthy side of the face is modeled to an $A(t)$ output signal required to reproduce the displacement on the contralateral paralyzed side.

First, we built a healthy side simulation model that simulated the EMG, $E(t)$, and healthy displacement, $Pos_H(t)$, resulting from a neural input. We will refer to this simulation model as the ERS simulation. The simulated $E(t)$ and $Pos_H(t)$ signals were then used to identify the ERS in Fig. 3-3. The methods and results of building and testing the ERS model are covered in Chapter 4. Once it was established that we could predict displacement from EMG, we built a paralyzed side simulation model that predicted the paralyzed side position change, $Pos_P(t)$, resulting from a stimulus amplitude modulation input, $A(t)$. This simulation model will be referred to as the SRS simulation. The $A(t)$ and $Pos_P(t)$ were used to identify the SRS in Fig. 3-3. The methods and results of building and testing the SRS model are covered in Chapter 5. Finally, the FRCS was built by identifying the SRS^{-1} and combining it with the ERS. The methods and results of building and testing the FRCS are covered in Chapter 6.

Although simulation studies might not be as robust as actual experiments, they can still demonstrate a proof of concept. The models identified from simulated data will still be able to show the relationship between the EMG, stimulus, and displacement that would also be seen in

Simulation Studies of Functional Electrical Stimulation for Facial Reanimation
Patrick Brebner

models identified with experimental data. Understanding these relations is key to providing insight into the dynamics of facial muscle and building the proposed facial reanimation device.

Chapter 4: Methods & Results – EMG Response System (ERS)

The ERS required for the FRCS must predict the healthy-side displacement, $\text{Pos}_H(t)$, associated with an EMG signal, $E(t)$. This chapter describes the process of building and evaluating the ERS which involved the following steps:

1. Build an ERS simulation model that generates $E(t)$ and $\text{Pos}_H(t)$ signals from a neural command input,
2. Simulate the signals associated with different movements,
3. Identify an ERS model relating $E(t)$, as input, to $\text{Pos}_H(t)$, as output,
4. Evaluate the performance of the estimated ERS models.

The results indicate that it is possible to identify accurate ERS models with signals of reasonable record length in the presence of noise.

4.1 Methods: EMG Response System

The ERS simulation model discussed in this section represents the healthy side of the face. The model takes a neural command train as its input and generates simulated $E(t)$ and $\text{Pos}_H(t)$ signals. This ERS simulation model has four main components:

1. Generate the neural input,
2. Transform the neural input to $E(t)$,
3. Transform the neural input to muscle force,
4. Use the muscle force to predict $\text{Pos}_H(t)$.

Two different input signals were generated to test the model and produce the simulated outputs required for ERS model identification.

4.1.1 ERS Simulation Model

Neural Input

The first step in building the ERS simulation was to generate the neural command input. In practice, this neural input translates into the number of active motor units and their firing rate. As discussed in the background section, changing the number of active motor units and/or

varying their firing rate is how the central nervous system (CNS) controls the force produced by a muscle.

The neural input is the command required to produce a desired displacement, with larger movements requiring a stronger and/or higher frequency neural input signal. Therefore, we simulated the neural input based on a desired movement signal with the amplitude and frequency of the neural input being dependent on the amplitude of the desired movement. Trains of square wave signals were used to represent the neural input for this model. The neural input was modelled as a pulse train whose amplitude represents the fraction of motor units used from 0 to 1, and whose frequency represents the average firing rate of the motor neurons recruited. Since the desired displacement ranged from 0 mm to 10 mm, the percentage of motor units used (amplitude) of the neural input was determined by multiplying the desired displacement amplitude by 100. Likewise, the frequency of the neural input was determined by multiplying the desired displacement amplitude by 14,000 to get a frequency range between 0 and 140 Hz. This is a reasonable frequency range for the neural input based on previous research of motor unit firing frequency and recruitment [1]. Equation 4-1 shows this procedure with $D(t)$ representing the desired displacement signals amplitude.

$$\text{Neural Input}(t) = \max(100D(t) \times \text{Square}(2\pi \times 14,000D(t) \times t), 0)$$

Equation 4-1: Calculating Neural Command Input Signal.

Thus, the larger the movement required, the larger the frequency and amplitude of the neural input. This simulates natural muscle recruitment and force summation where an increase in muscle force is achieved by increasing stimulus frequency and amplitude. The higher frequency results in muscle tetanus and the increased magnitude recruits more and larger motor units to produce more force output. Figs. 4-1a and 4-1c show the desired displacement and resulting neural input for four simple movements. Figs. 4-1b and 4-1d show the increase in frequency from the desired displacement to the neural command input for each movement.

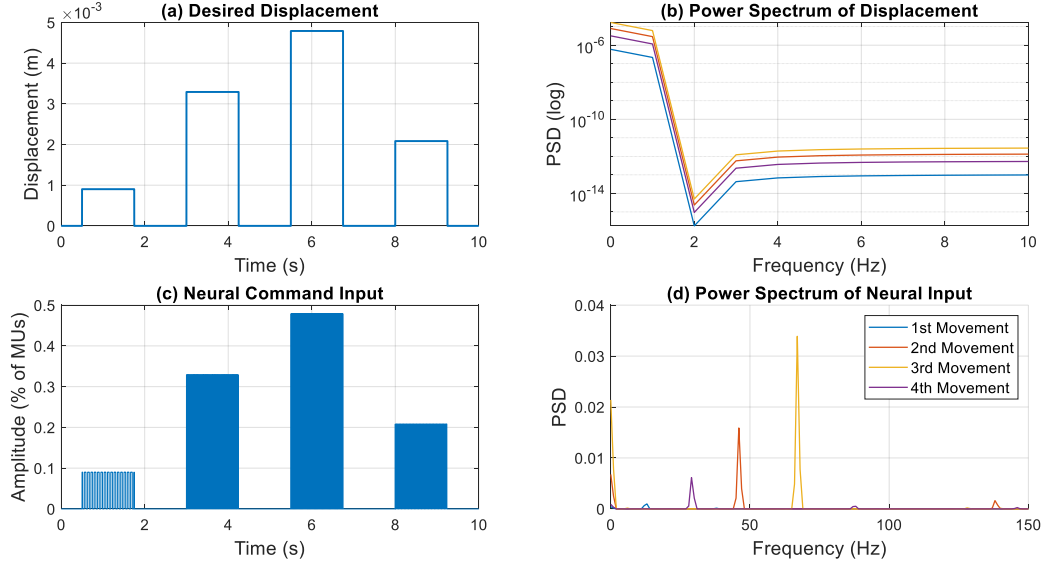


Figure 4-1: Transition from Desired Displacement to Neural Input for a Simple Movement.

EMG

EMG was generated by multiplying the neural input by a Gaussian noise signal band limited to 10 - 500 Hz. This band was chosen since it represents that of a typical EMG signal. Fig. 4-2 shows the Simulink subsystem that generates the simulated EMG, $E(t)$.

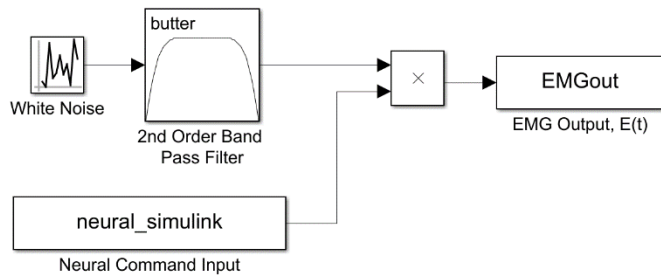


Figure 4-2: EMG Simulation (Simulink).

Neural Input – Force Simulation

The neural input-force subsystem, which generates muscle force from the neural command input, was designed to replicate the muscle activation dynamics. It has been shown that in many muscles, that the relationship between neural input and muscle force during an isometric contraction can be represented by a low pass filter [59, 60]. Therefore, we used a 2nd order low pass Butterworth filter with a cut-off frequency of 2 Hz to simulate muscle force. This cut-off

frequency is consistent with previous studies [59]. A Butterworth filter was used due to its good balance between the smoothness of the passband/stopband and the rate of transition. Finally, the model includes a half wave rectifier since muscles can only generate positive forces. Fig. 4-3 shows the Simulink subsystem that simulates muscle force from a neural command input.

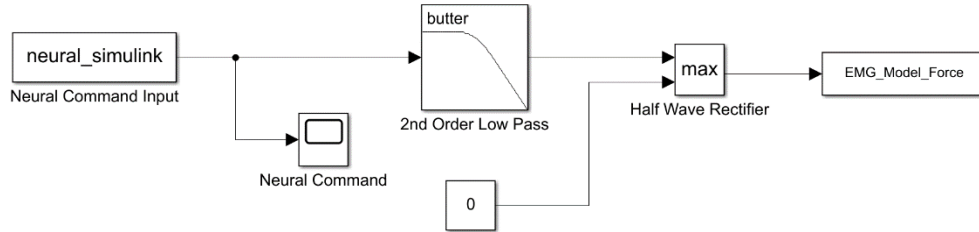


Figure 4-3: Force Simulation (Simulink).

Figs. 4-4a and 4-4c show the transition muscle force response to the neural input for four simple movements. Figs. 4-4b and 4-4d show the decrease in frequency from the neural command input to the muscle force that results from the muscles low pass dynamics.

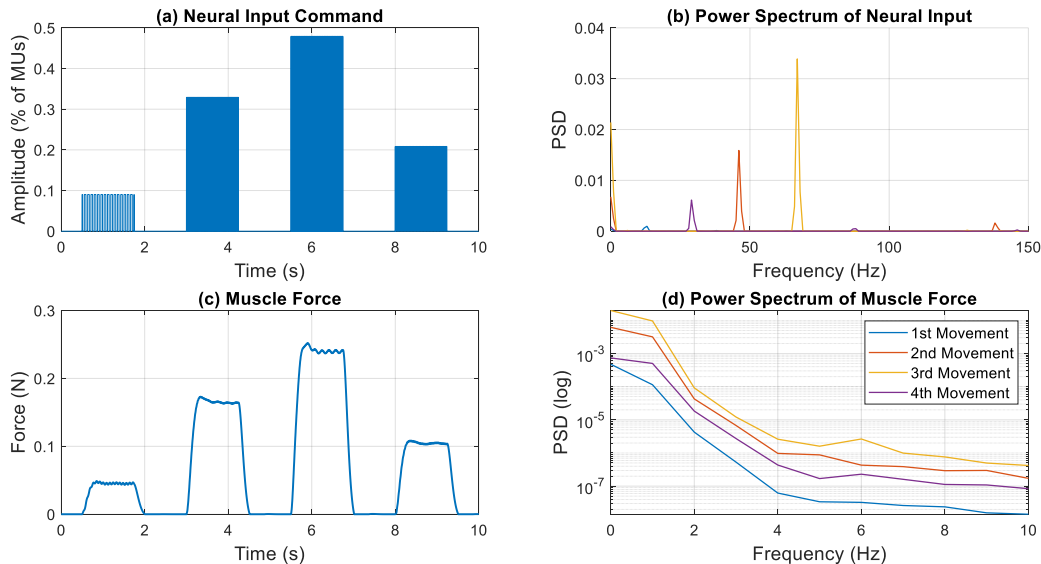


Figure 4-4: Transition from Neural Input to Muscle Force for a Simple Movement.

Muscle Load Model (Mass-Spring-Damper)

To predict the $\text{Pos}_H(t)$ resulting from the muscle force we used a mass-spring-damper muscle load model. The mass, spring constant and damping coefficient of the facial muscle model were based

on a previous paper and were estimated as 0.9 g, 52.025 N/m and 6 Ns/m, respectively [61]. These values produced a realistic displacement output from the mass-spring-damper model. However, since the properties of muscle naturally change during contraction, a more realistic approach would be to have the spring constant scale with the muscle force. The larger the muscle contraction the stiffer the muscle becomes. This would be more accurate physiologically but would add nonlinear behavior during large contractions. For this reason, the elastic properties of the muscle were held constant for this model. Fig. 4-5 shows the Simulink subsystem that simulates $\text{Pos}_H(t)$ from muscle force.

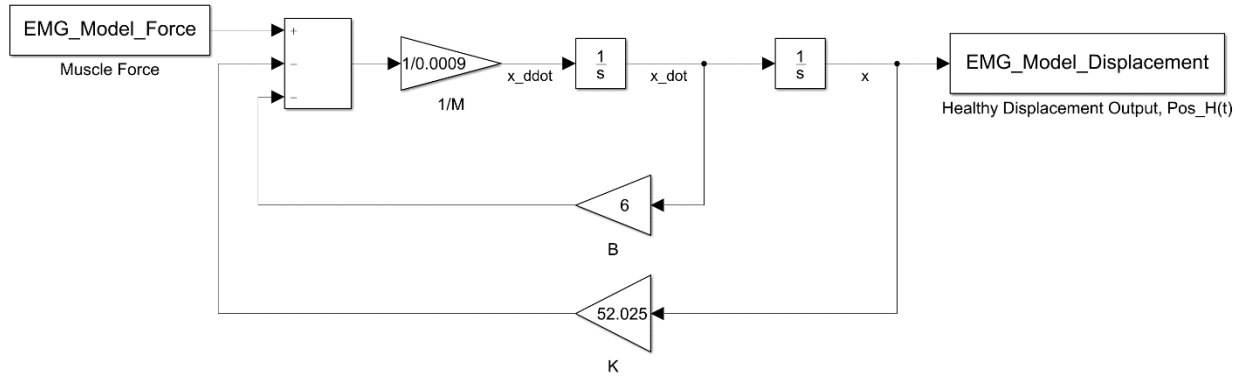


Figure 4-5: Healthy Displacement Simulation (Simulink).

Combining these subsystems together we created an ERS simulation model that outputs EMG, $E(t)$, and healthy displacement, $\text{Pos}_H(t)$, signals resulting from a neural command input. The ERS simulation was built in MATLAB/Simulink. Fig. 4-6 shows the full ERS simulation model.

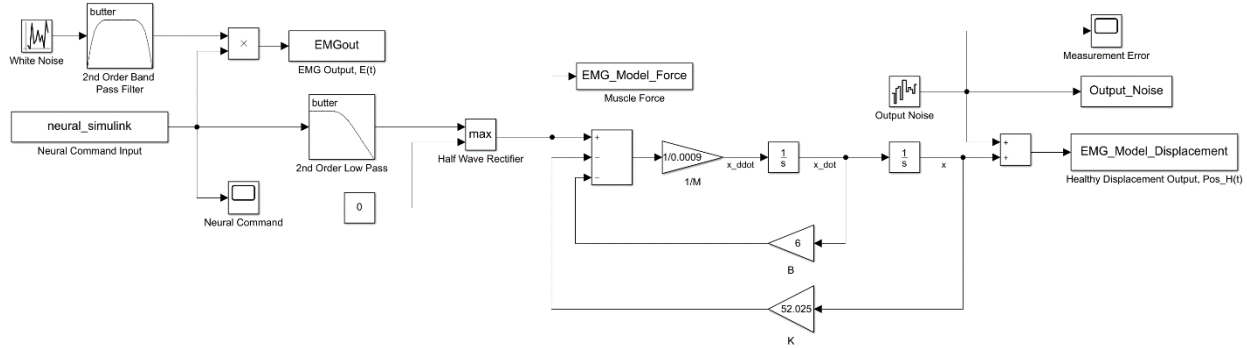


Figure 4-6: ERS Simulation Model (Simulink).

4.1.2 Input Signals

Two types of displacement input signals were used to identify and test the ERS model: Pseudo Random Binary Sequence (PRBS) signals and “physiological” signals. A PRBS signal is a deterministic signal with broad-band properties that switches between two set values. At each designated switching time the signal may either switch or stay the same with equal probability. When generating a PRBS, there are two parameters to be specified: the two values the PRBS switches between, known as the range, and the minimum time for which the value of the signal does not change, known as the clock period. The PRBS used for this model has a range of 0 mm to 10 mm and the clock period of 100 milliseconds. We modified the PRBS by having the maximum value of the range change randomly every 10 seconds to a value between 0 and 10 mm. This signal was used to identify an ERS model over a wide range of movement amplitudes.

Fig. 4-7 shows an example of this modified PRBS waveform used for the ERS model.

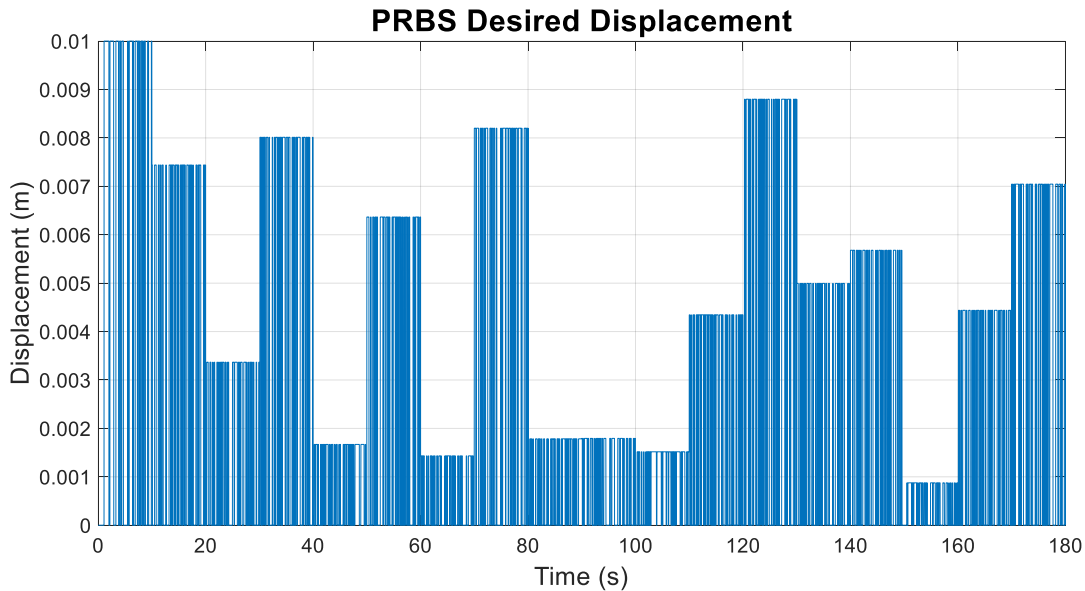


Figure 4-7: Typical Modified PRBS Displacement for the ERS Model.

The PRBS signals provide a rich input for identification but do not represent a real-world scenario. During tactile exploratory behavior, rats sweep their whiskers back and forth in a rapid, rhythmic motion called whisking [62]. Rats can vary whisking amplitude and velocity, and contact with an object strongly affects subsequent whisking motions [63]. A previous facial reanimation study using rat models saw whisking frequencies up to 6 Hz with amplitudes ranging from 0 mm to 20 mm [13]. The “physiological” signal was created to simulate these types of spontaneous movements with parameters within these ranges. Thus, the “physiological” displacement input was comprised of trains of square pulses with amplitudes and pulse repetition frequencies that changed randomly every 10 seconds. The random amplitude was taken from a uniform distribution from 0 mm to 10 mm. The random repetition frequencies were sampled from a normal distribution truncated between 0 and 1.8 Hz with constant pulse widths of 550 milliseconds. A goal of using this signal type was to determine if there was a limit to the number of movements (pulses) required to estimate a model accurately. Therefore, through multiple trials the number of movement pulses were decreased to determine if there was a limit. Fig. 4-8 shows an example of the “physiological” displacement used for the ERS model.

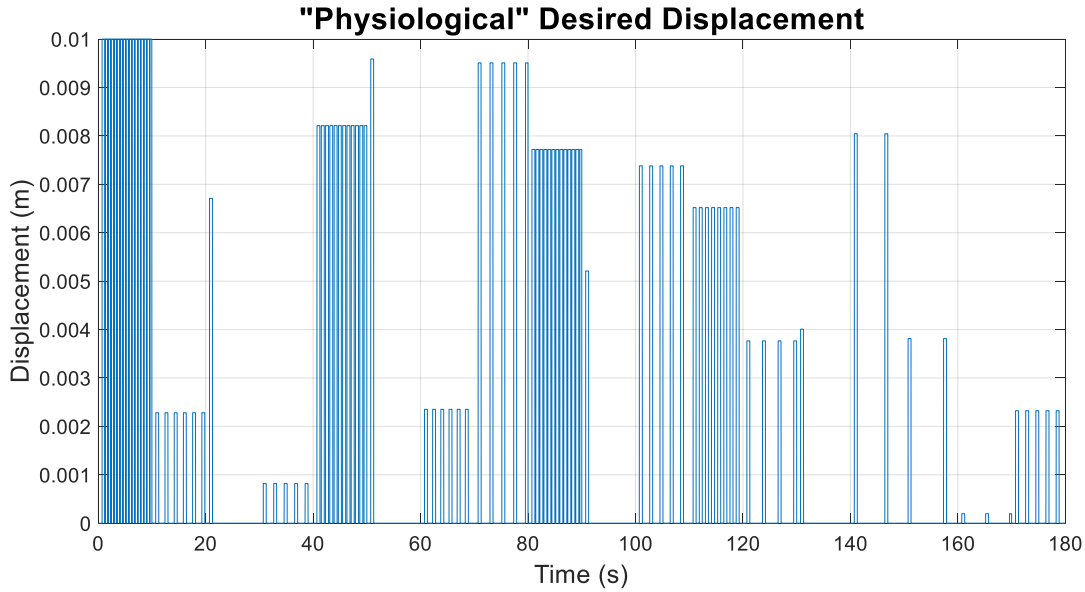


Figure 4-8: Typical "Physiological" Displacement for the ERS Model.

4.1.3 ERS Model Identification

Finally, with the ERS simulation model completed and an $E(t)$ and $\text{Pos}_H(t)$ signal generated in response to the neural command input, we could identify the ERS model needed for the FRCS. For the ERS, a Hammerstein model was identified between the $E(t)$ signal and $\text{Pos}_H(t)$ signal using an iterative identification method developed by Hunter and Korenberg known as the HK method [64]. This was implemented using the MATLAB nonlinear identification (NLID) toolbox developed by Dr. Kearney [65].

4.2 Results: EMG Response System

4.2.1 Simulation and Identification with PRBS Inputs

Fig. 4-9 shows a typical trial with a desired displacement PRBS and the resulting neural command and muscle force. Fig. 4-9b and 4-9d show the power spectrum of the desired displacement PRBS and neural command, respectively. The power spectrum of the desired displacement PRBS illustrates that the dominate frequencies were between the 0 - 10 Hz values and that the power dips at the 10 Hz value and the subsequent harmonic frequencies. The neural command power spectrum shows the location of dominant frequencies between 0 and 140 Hz. As expected, Fig. 4-9e shows that the force signal mirrored the neural command signal.

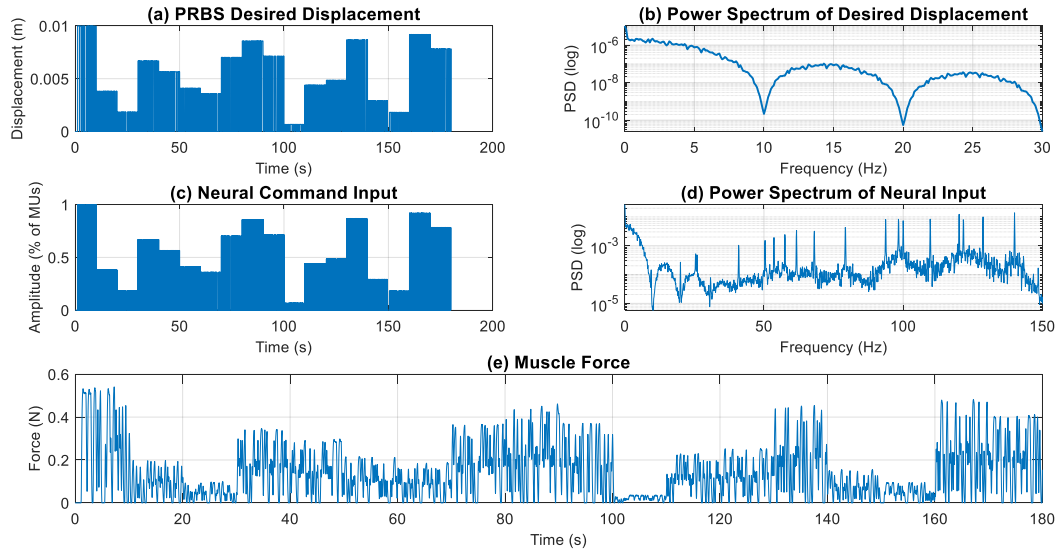


Figure 4-9: PRBS Input for ERS Simulation; (a) Desired displacement, (b) Power spectrum of desired displacement, (c) Neural command input, (d) Power spectrum of neural command, (e) Muscle force.

The outputs of the ERS simulation are $E(t)$ and $\text{Pos}_H(t)$. Fig. 4-10 shows the resulting $\text{Pos}_H(t)$ and $E(t)$ signal.

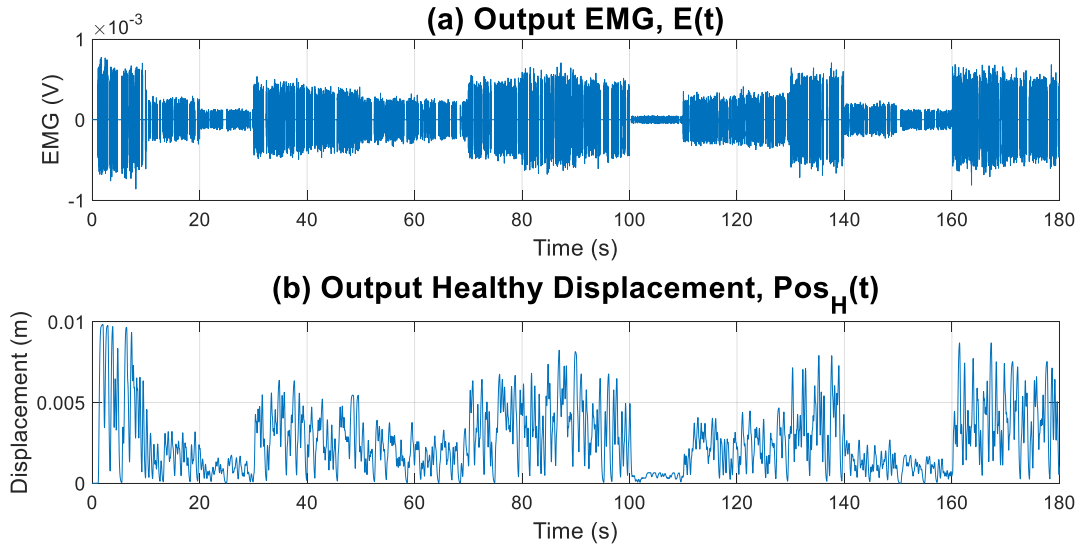


Figure 4-10: Output Healthy Displacement, $\text{Pos}_H(t)$, and EMG, $E(t)$, resulting from a PRBS Input.

The next step was to identify a Hammerstein model between $E(t)$, as input, and $\text{Pos}_H(t)$, as output. Fig. 4-11a shows the static nonlinearity estimated for the Hammerstein model. The static

nonlinearity resembles a full wave rectifier up until the values marked with a red dashed line. Beyond these limits the estimate of the nonlinearity becomes unreliable due to the lack of input data. Fig. 4-11b shows the probability distribution of the input $E(t)$ signal; there were many data points in the middle of the distribution which resulted in a robust estimation of the nonlinearity for those input values. Beyond the red dashed lines there were very few input data points which leads to the unreliable part of the model in Fig. 4-11a. Values within this limit are considered “high-quality”. In general, when the input $E(t)$ signal has a smaller amplitude range this limit decreases. In these cases, the model can become unreliable for many potential input values. This is an important point when designing the input to make sure the distribution of the $E(t)$ adequately covers the required range of input values.

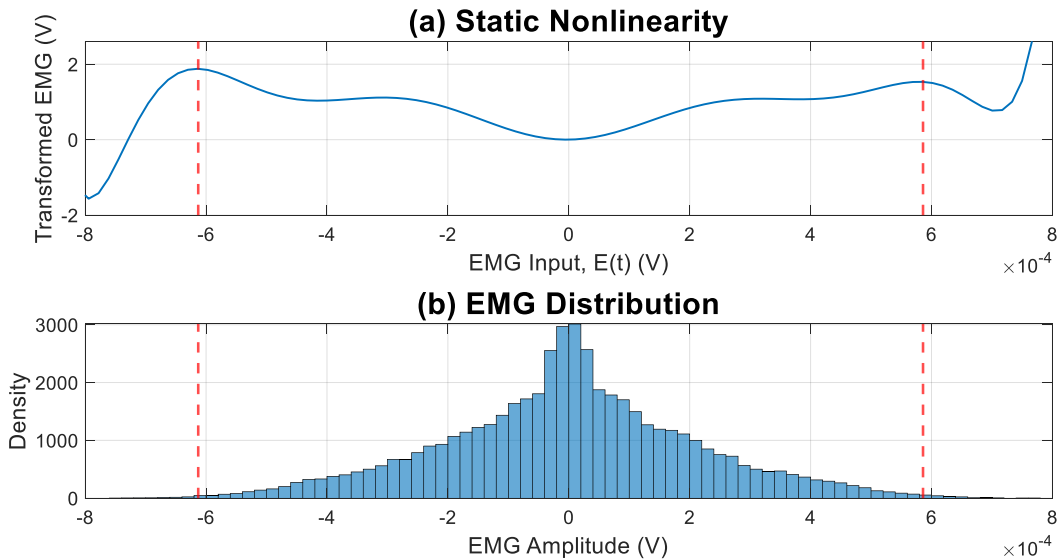


Figure 4-11: Static Nonlinearity of Identified Hammerstein Model compared to Input EMG, $E(t)$, Distribution.

Fig. 4-12 shows the full Hammerstein model estimate that includes a static nonlinearity followed by a dynamic linear element. For the static nonlinearity, only high-quality values were plotted. The identified model has a structure similar to that predicted with a full wave rectifier as the input nonlinearity followed by a low pass filter.

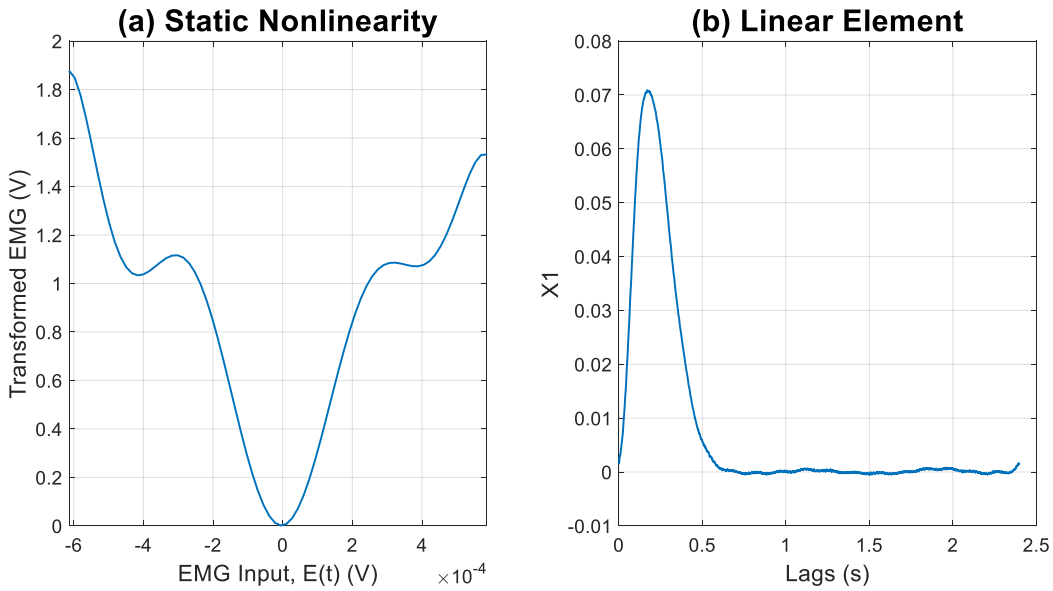


Figure 4-12: ERS Hammerstein Model Identified from PRBS Input.

This Hammerstein model achieved a variance accounted for (VAF) of 97.5%. Fig. 4-13 illustrates this high accuracy by superimposing the predicted and observed $\text{Pos}_H(t)$.

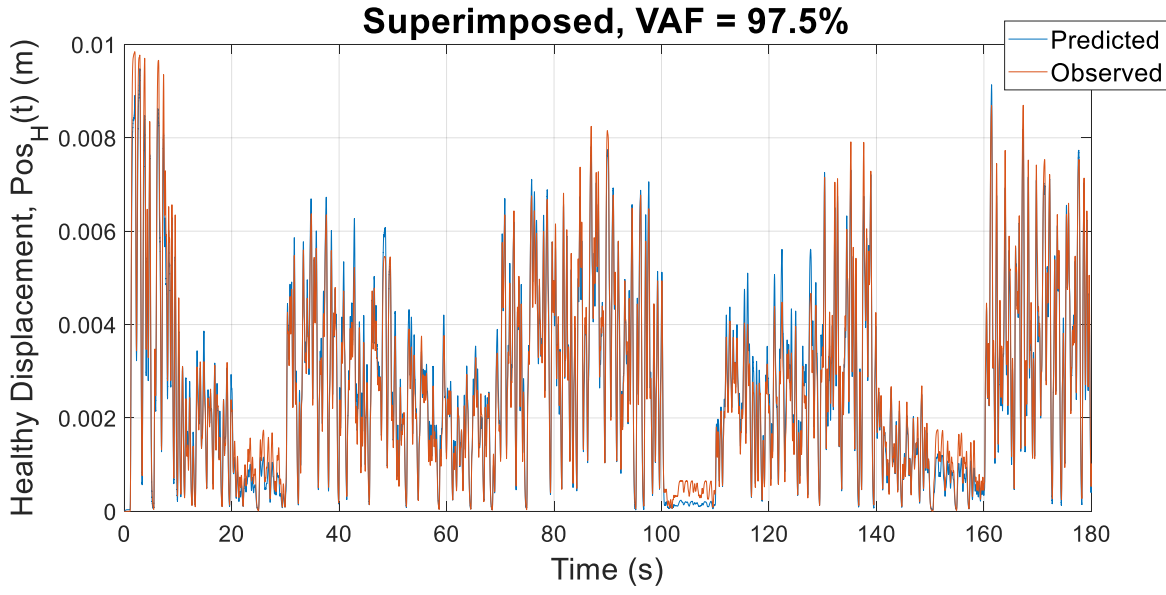


Figure 4-13: Accuracy of ERS Hammerstein Model Identification.

Fig. 4-14 examines the residuals of the model identification. Fig. 4-14b shows the residual probability distribution; the residuals are relatively evenly spaced around the zero value. This indicates that the errors of the model were generally small and were evenly distributed in the

positive and negative direction. Fig. 4-14c shows the power spectrum of the residuals and indicates that the residuals are not white but besides a spike near 0 Hz, there was no other frequency with significant power.

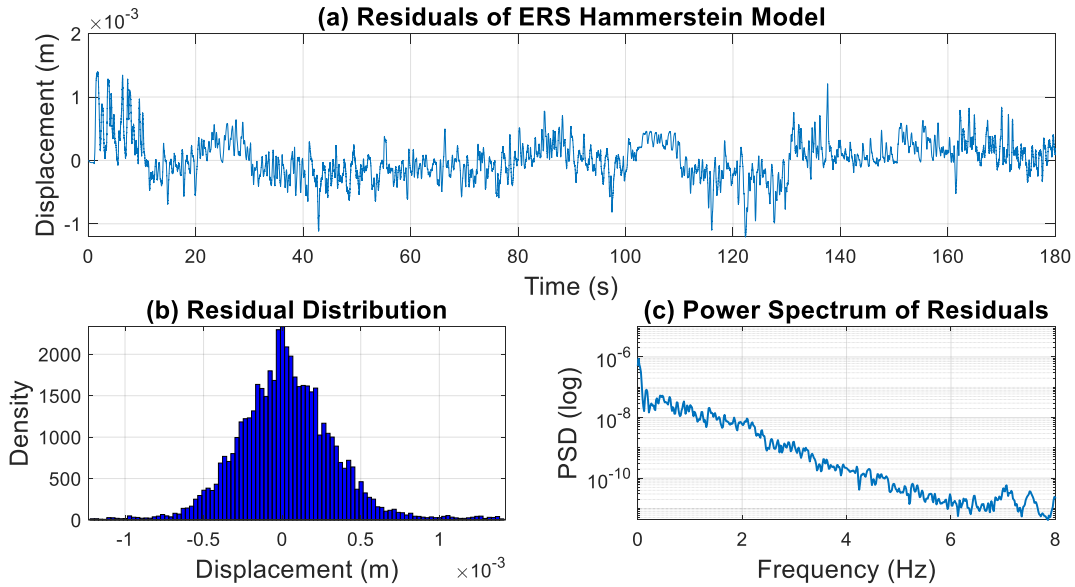


Figure 4-14: Residual Analysis of Model Identification Results.

4.2.2 Simulation and Identification with “Physiological” Input

The results of the previous input signal demonstrated that we can successfully identify the ERS model using a wide band PRBS input. This section determines if we can successfully identify the ERS model from a signal resembling that expected in experimental trials. Fig. 4-15 is an example of this “physiological” desired displacement and the corresponding neural command input and muscle force. The power spectrum of the desired displacement signal in Fig. 4-15b shows that the dominate frequencies were between 0 and 1.8 Hz. The neural command power spectrum in Fig. 4-15d shows the dominant frequency values were between 0 and 140 Hz. Once again, Fig. 4-15e shows that the force signal mirrored the neural command signal.

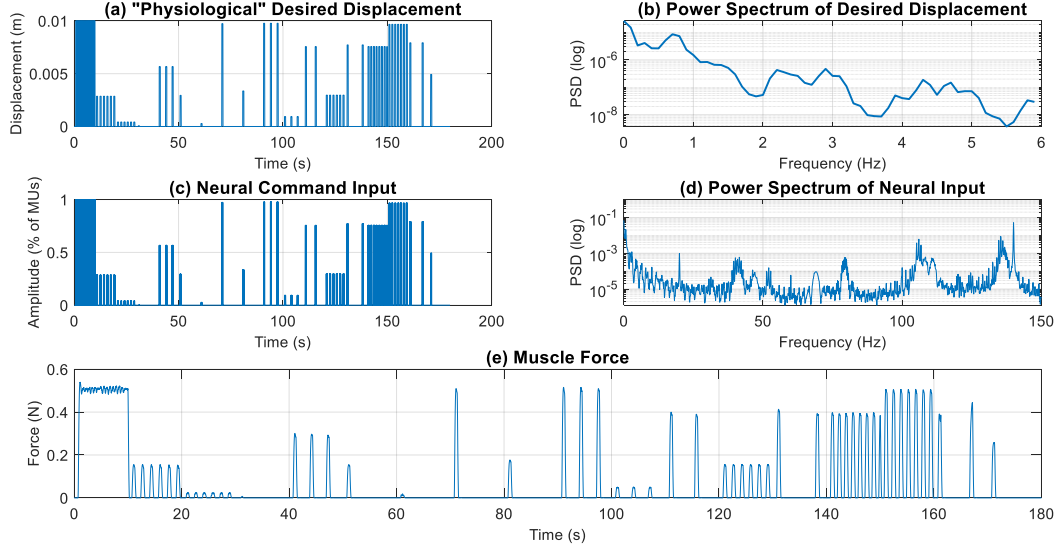


Figure 4-15: “Physiological” Input for ERS Simulation; (a) Desired displacement, (b) Power spectrum of desired displacement, (c) Neural command input, (d) Power spectrum of neural command, (e) Muscle force.

Fig. 4-16 shows the $\text{Pos}_H(t)$ and $E(t)$ signals resulting from the simulation. With the individual pulses the relationship between the two signals is clearer. Larger $E(t)$ pulses in Fig. 4-16a, which also had a higher frequency, produced a larger $\text{Pos}_H(t)$ in Fig. 4-16b.

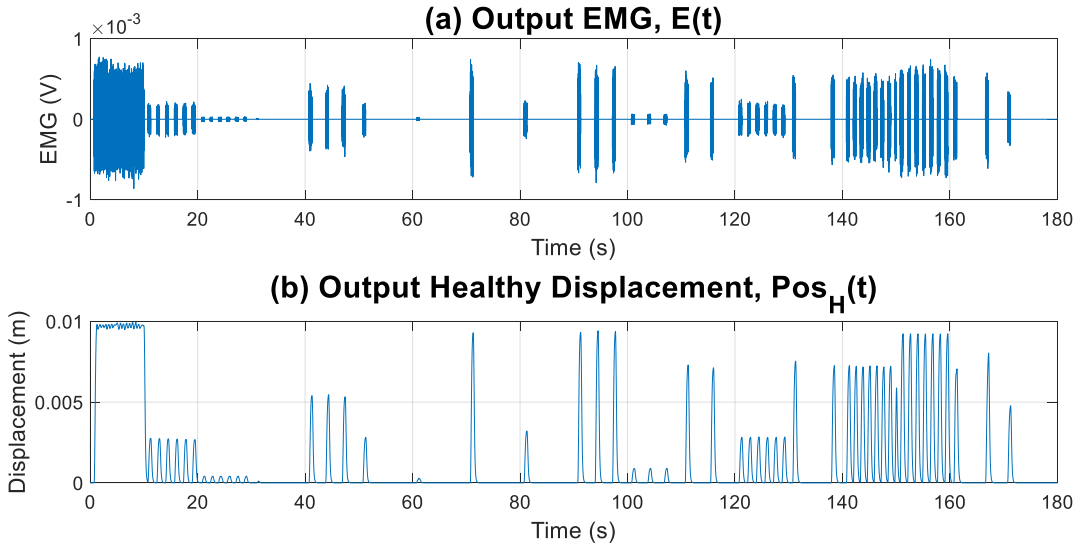


Figure 4-16: Output Healthy Displacement, $\text{Pos}_H(t)$, and EMG, $E(t)$, resulting from a “Physiological” Input.

Fig. 4-17 shows the Hammerstein model identified between $E(t)$, as input, and $\text{Pos}_H(t)$, as output. The static nonlinearity shows only the “high-quality” results, which were determined in

the same way as the previous model. Once again, the model resembled a full wave rectifier followed by a low pass filter.

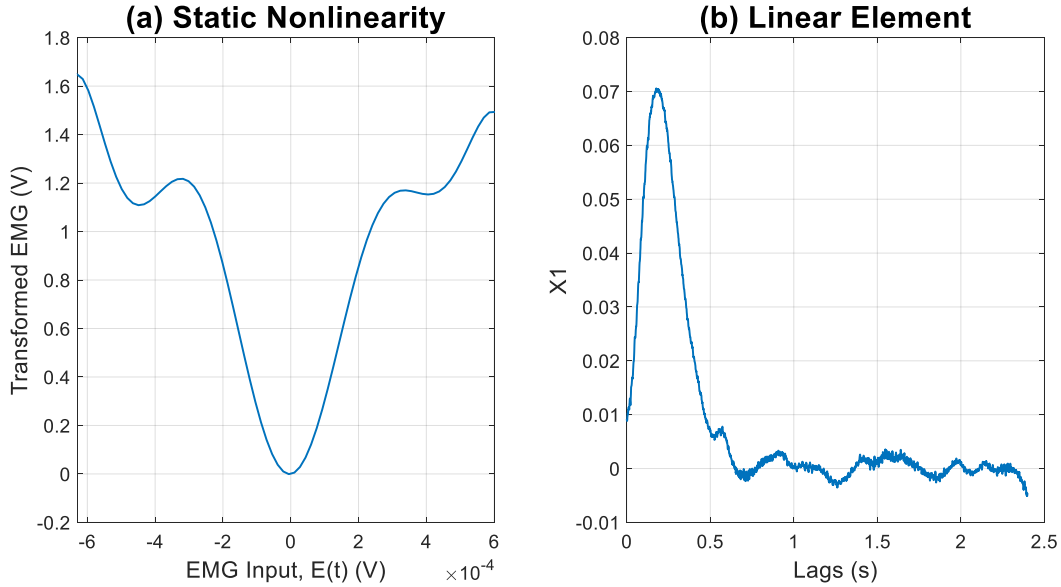


Figure 4-17: ERS Hammerstein Model Identified from “Physiological” Input.

Fig. 4-18 shows the accuracy results of the model identification. This model achieved a VAF of 99.2% for the “physiological” example.

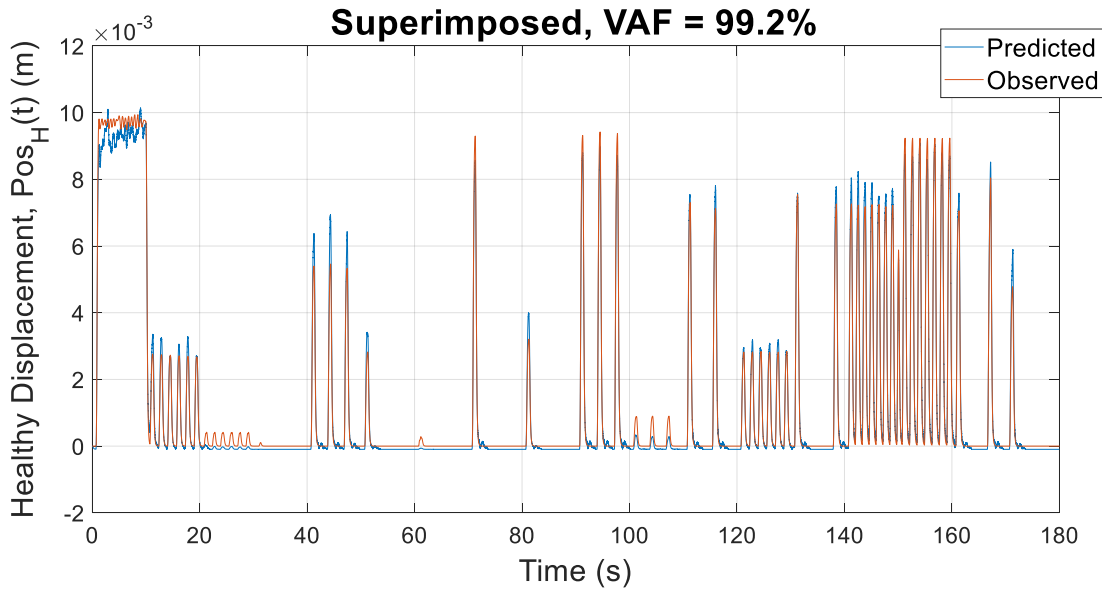


Figure 4-18: Accuracy of Model Identification.

Fig. 4-19 shows that the residuals were also acceptable considering the type of input. The residual distribution in Fig. 4-19b is concentrated around zero and relatively evenly distributed in both the positive and negative direction. There is a slight offset when predicting a displacement of zero that is illustrated by the much larger bin in the distribution. The power spectrum of the residuals in Fig. 4-19c was not white and shows that the model errors were generally concentrated in lower frequencies.

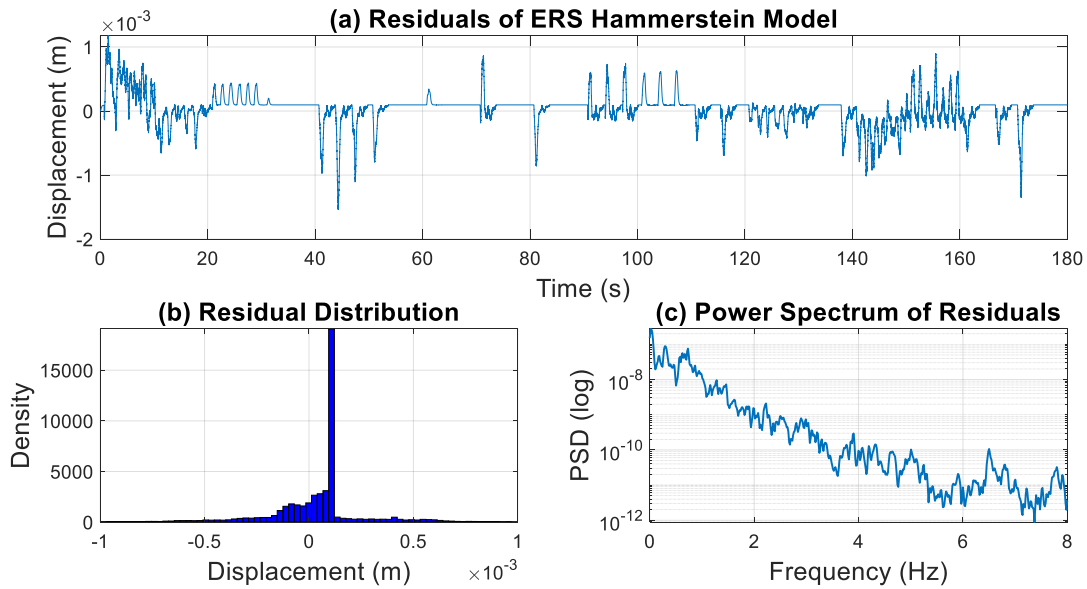


Figure 4-19: Residual Analysis of Model Identification.

Finally, Fig. 4-20 compares the two identified ERS models from Figs. 4-12 and 4-17, illustrating that both models had similar structure for the nonlinear and linear elements.

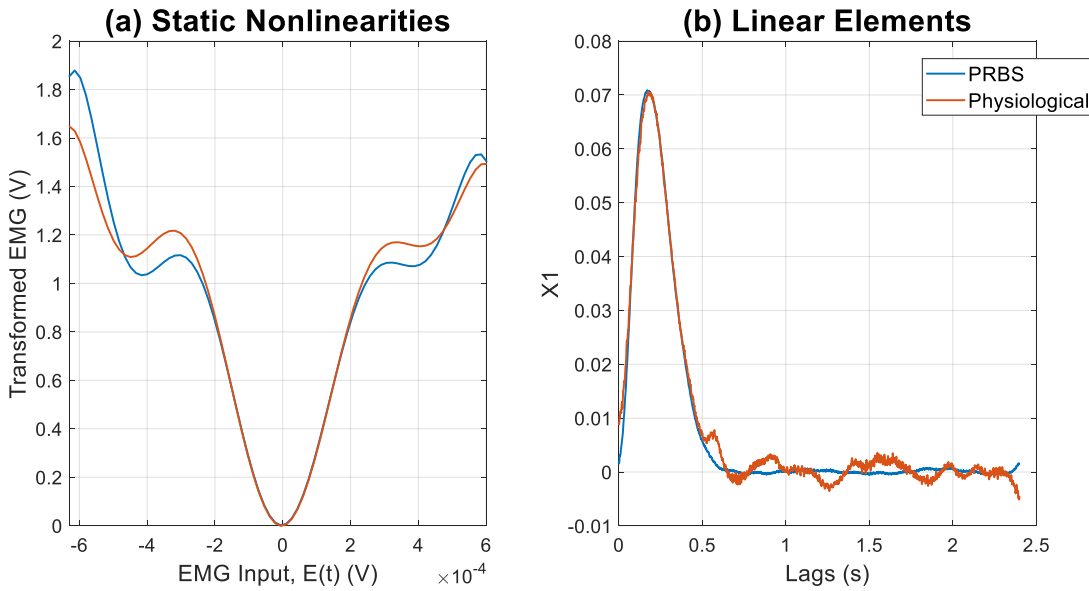


Figure 4-20: Comparison of ERS Hammerstein Models Identified from Different Input Types.

4.2.3 ERS Model Validation

To validate the identified ERS models, the models were used to predict the movements generated in response to input realizations different than those used to identify the model. Models identified with both types of input signals were tested. First, a model was tested with another realization of the same type of signal used to identify the model. Then, the model was tested with the other signal type not used for the model identification.

First, the ERS model identified from the PRBS signal was validated. When used to predict the $\text{Pos}_H(t)$ of another realization of the PRBS signal the model performed very well. Fig. 4-21 shows the model achieved a VAF of 97.7% for this validation trial with residuals similar to those seen during model identification with a PRBS input.

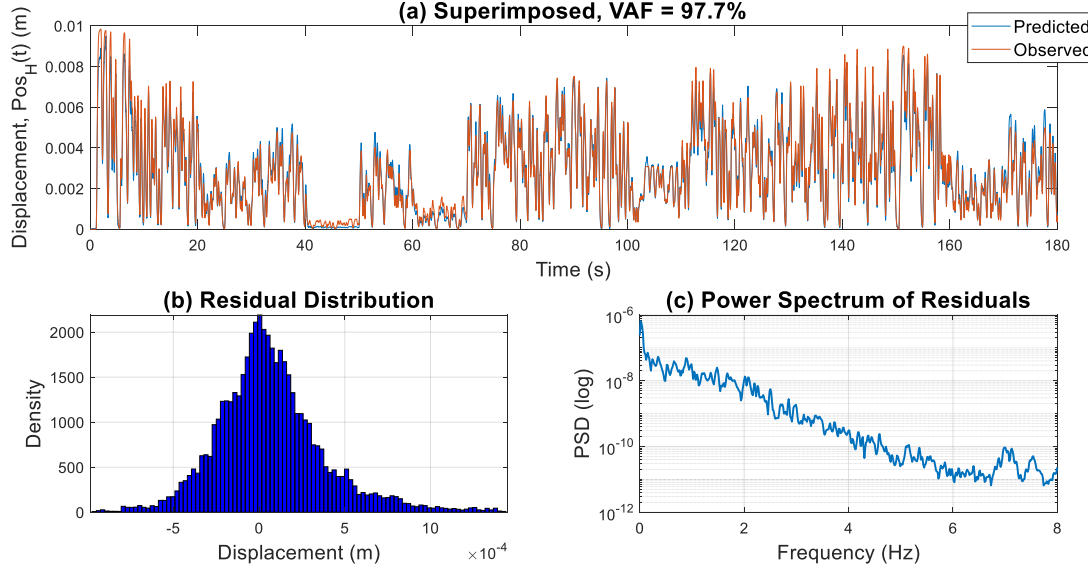


Figure 4-21: Results of PRBS identification & Validation.

When the model is used to predict the $\text{Pos}_H(t)$ of the “physiological” input signal the model also performed well. Fig. 4-22 shows that the model achieved a VAF of 98.6% for this validation trial. This high accuracy was likely due to the wide band PRBS used to identify the model being a very rich input and covering all possible signal variations. The residual distribution shows that the errors were concentrated around zero and distributed in both the positive and negative direction.

There is only a slight increase in the distribution around 0.5 mm. The power spectrum starts high at 0 Hz and the power decreases as frequency increases with no significant spike in power.

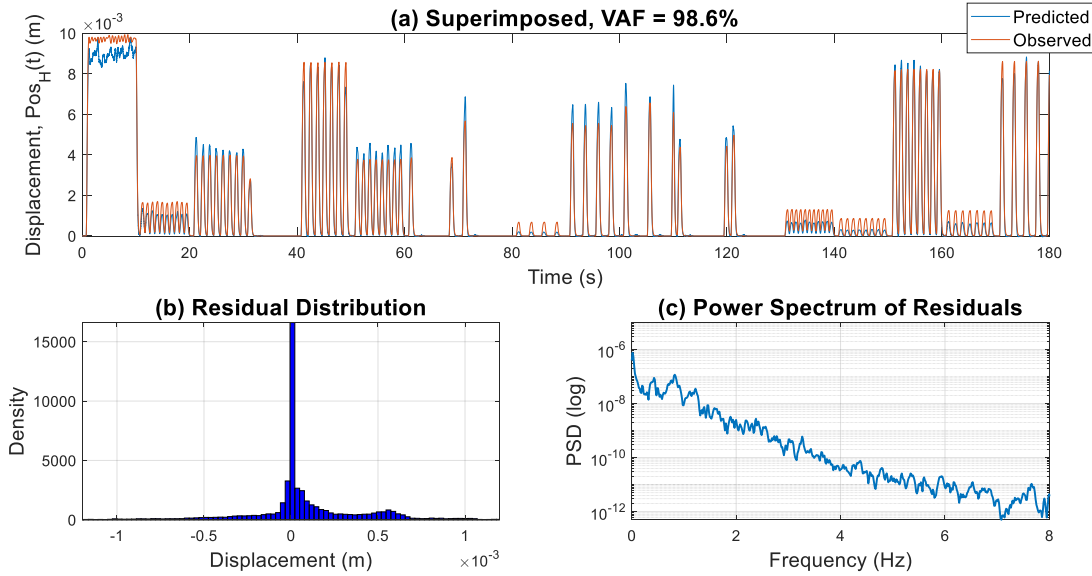


Figure 4-22: Results of PRBS identification & “Physiological” Signal Validation.

Next, the ERS model identified from the “physiological” input was validated by testing it on other realizations of the “physiological” inputs and PRBS inputs. When using the model to predict the $\text{Pos}_H(t)$ of another realization of the “physiological” input the model achieved a VAF of 98.7% for this validation trial. The residual distribution and spectrum are very similar to those seen during model identification with the “physiological” input. Fig. 4-23 shows these results.

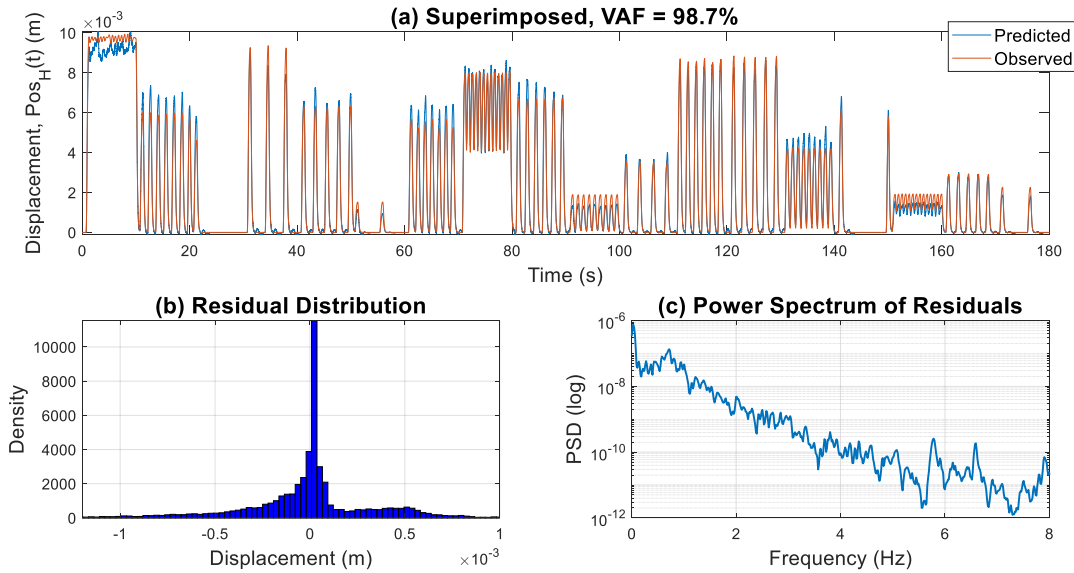


Figure 4-23: Results of “Physiological” Signal Identification & Validation.

When this model was used to predict the $\text{Pos}_H(t)$ of the PRBS signal the accuracy was still very good. Fig. 4-24 shows that the model achieved a VAF of 96.1% for this validation trial. The residual distribution shows that the errors were concentrated at zero meters generally evenly distributed in the positive and negative direction. The spectrum in Fig. 4-24c shows a spike at 0 Hz but no other significant power spikes at other frequencies.

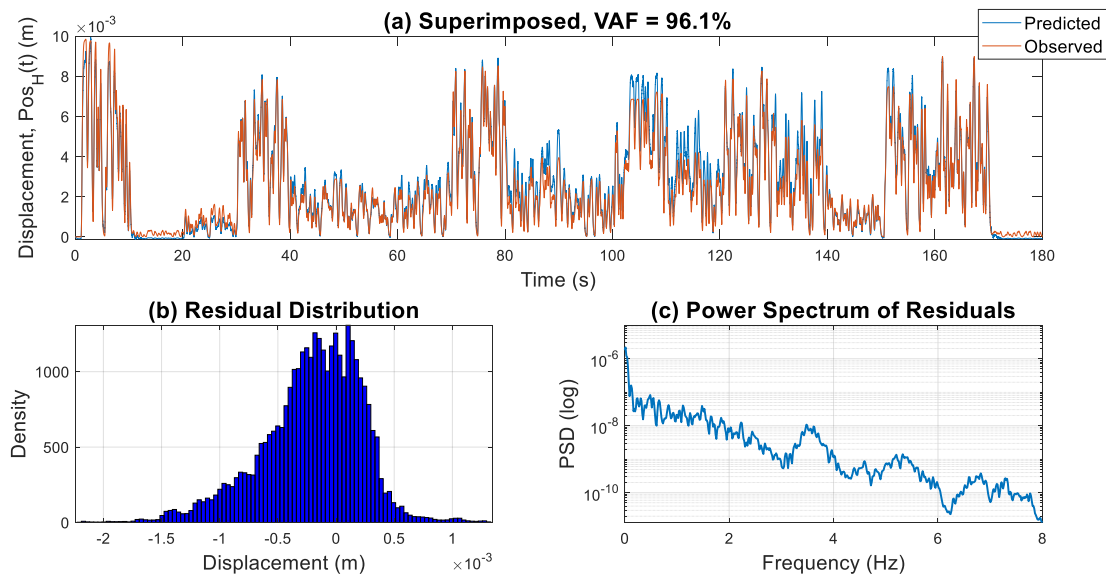


Figure 4-24: Results of “Physiological” Signal Identification & PRBS Validation.

Table 4-1 provides the VAF mean and standard deviation for each model over 30 validation trials. Overall, the ERS models performed well, regardless of the type of signal used when identifying the model. With some small exceptions, the residual distributions were concentrated around zero meters and although the spectrums of the residuals were not white, there was no significant power spikes at frequencies the models were not able to handle.

Table 4-1: Average ERS Model Accuracies during Model Validation.

ERS Model Accuracy		
Signal Used for Model Validation	Signal Used for ERS Model Identification	
PRBS	PRBS	Physiological
Physiological	$97.6 \pm 0.5\%$ VAF	$97.2 \pm 0.5\%$ VAF
	$98.7 \pm 0.2\%$ VAF	$99.0 \pm 0.2\%$ VAF

4.2.4 Input Signal Limitations

There were some limits on the signals used for ERS model identification. The input signal used for identification needs to contain enough information to accurately identify the model. First, the signal used for model identification needs to contain the full range of possible input amplitudes. If the model is identified with a signal not containing the full range of inputs, the model accuracy will suffer. This is demonstrated in Fig. 4-25, where constant amplitude PRBS signals of decreasing maximum amplitude were used for ERS model identification. These models were then validated with 30 realizations of “physiological” inputs to calculate the VAF mean and standard deviation. As demonstrated in the figure, when the identification signals amplitude decreased there came a point where the model performed poorly during validation. In this case, the limit was around 8.5 mm.

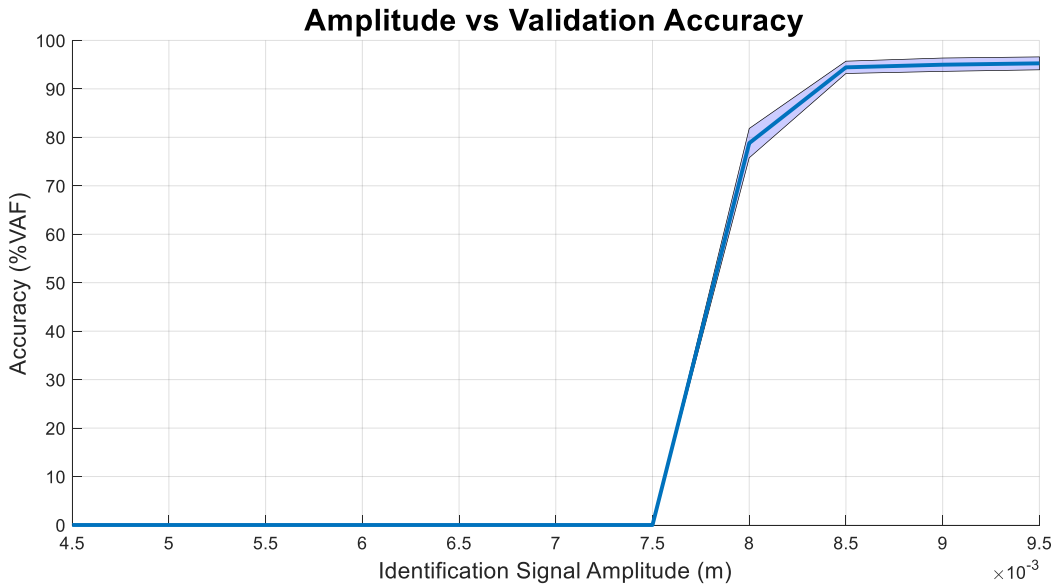


Figure 4-25: Amplitude vs Validation Accuracy; Average validation accuracy (solid blue line) and standard deviation of validation accuracy (shaded blue area).

Next, there was a minimum number of movements required to create a robust model with high and consistent validation accuracy. To quantify this, 20 modified “physiological” inputs, each with a different number of movement pulses, were used to identify ERS models. The first modified “physiological” input had only one movement pulse, with each subsequent input increasing the number of movement pulses by one. The ERS models identified from these signals were then validated with 30 realizations of “physiological” inputs in order to calculate the VAF mean and

standard deviation. Fig. 4-26 shows that the ERS model required a minimum of 2 movement pulses in the identification signal to achieve an average VAF of 95%.

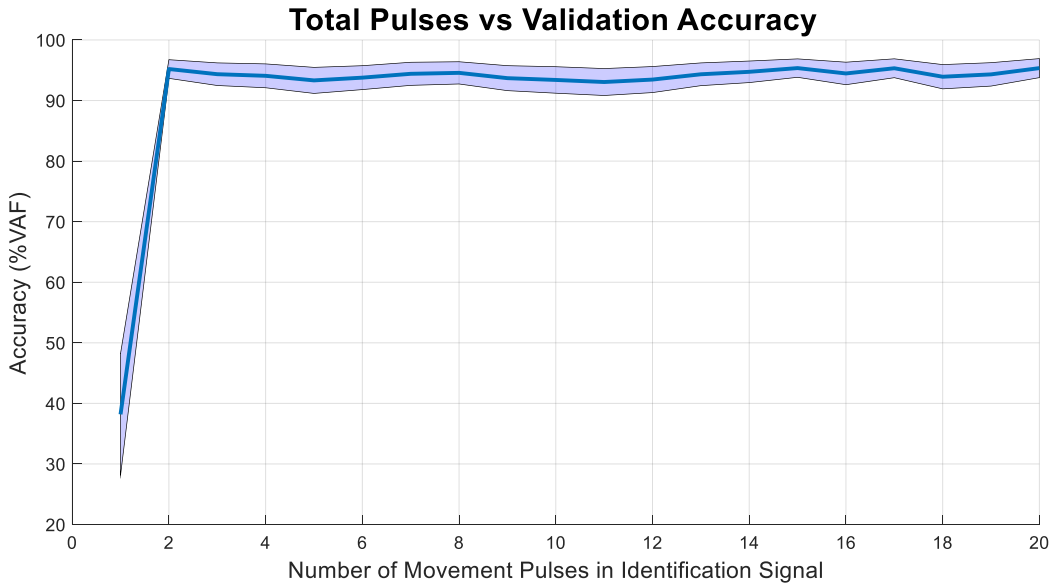


Figure 4-26: Total Pulses vs Validation Accuracy; Average validation accuracy (solid blue line) and standard deviation of validation accuracy (shaded blue area).

4.2.5 Noise and Record Length

The previous results all had no noise added to the system. In an experimental trial this is completely unrealistic. Although there are ways to mitigate noise, there will always be some present in an experimental trial. In the following results, white noise was added to the healthy displacement output, $\text{Pos}_H(t)$, to simulate measurement error. With the noise added to the simulation model we could see how much noise was acceptable while still maintaining a high ERS model accuracy.

For this experiment we examined how different levels of noise effect the accuracy of the ERS model during model validation. Two different signal types were used to identify the models used during these trials: a PRBS and a “physiological” signal. First, a “clean” $\text{Pos}_H(t)$ signal was generated from the ERS simulation model using both input types. Then, a set of ERS models were identified for each type of input, with the output noise steadily increased for each one. Fig. 4-27 shows the identification accuracy for these models. The identification accuracy was calculated by comparing the predicted $\text{Pos}_H(t)$ of the identified ERS models to the “clean” $\text{Pos}_H(t)$, before noise was added. The identification accuracy remained high for both types of models when the signal

to noise ratio (SNR) was above -16 dB with the “physiological” model having a slightly better tolerance to the added noise.

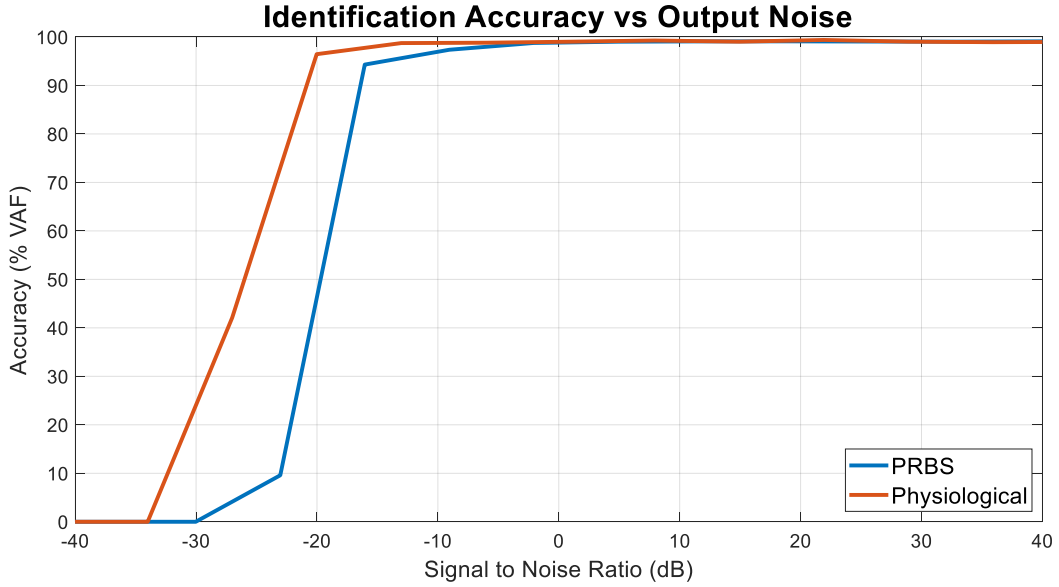


Figure 4-27: Identification Accuracy vs Output Noise for Two different Signal Types.

These identified ERS models were then validated with “physiological” signals over 30 trials. Fig. 4-28 shows the average validation accuracy of these trials. In a similar pattern to the identification accuracy, both ERS model types achieved high and consistent validation accuracies for SNR values above -16 dB.

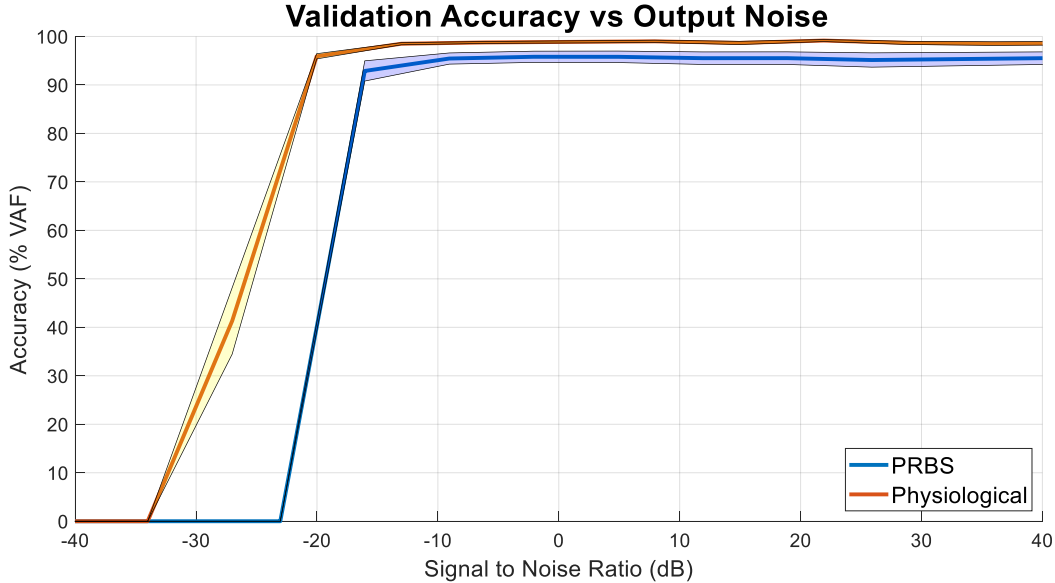


Figure 4-28: Validation Accuracy vs Output Noise for Two different Signal Types; Average identification accuracy (solid lines) and standard deviation of accuracy (shaded areas).

Next, the effects of identification signal record length on the ERS models accuracy was tested. For the following experiment, PRBS signals of increasing record length were used for model identification. These models were then validated with “physiological” signals over 30 trials to see how the identification signal record length effected the validation accuracy. Fig. 4-29 shows the average validation accuracy for these trials. The results show that the ERS model required a minimum record length of 4 seconds to achieve a high average VAF although at least 10 seconds was required to consistently achieve a VAF above 90%.

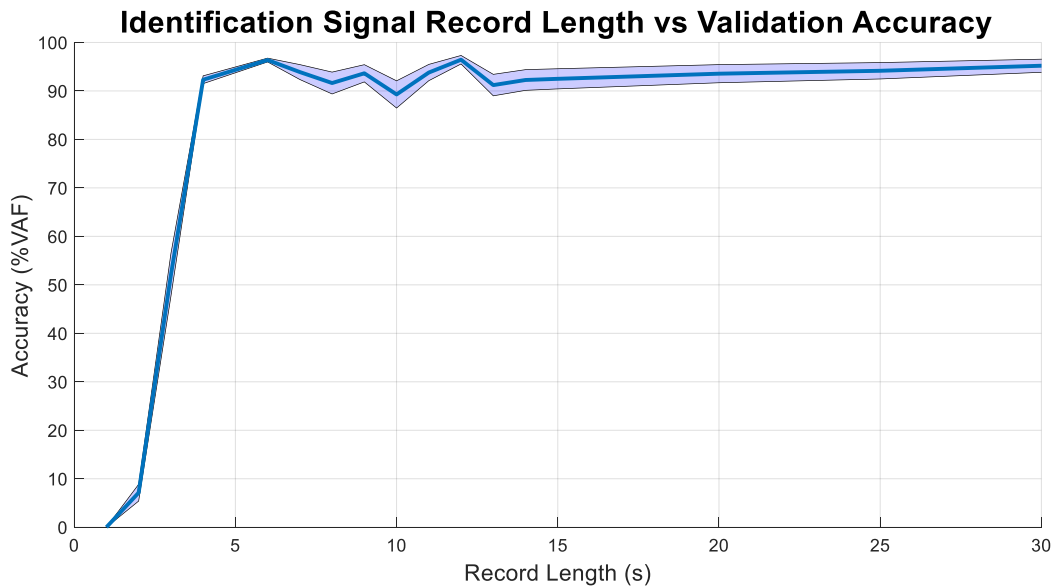


Figure 4-29: Identification Signal Record Length vs Validation Accuracy; Average validation accuracy (solid line) and standard deviation of accuracy (shaded area).

Summary

This chapter outlined a process of identifying the ERS model using simulated data. To acquire the simulated data, an ERS simulation model that represents the healthy side of the face was created that produced EMG, $E(t)$, and healthy displacement, $Pos_H(t)$, signals from various neural command inputs. The identified ERS was able to accurately estimate $Pos_H(t)$ from an input $E(t)$ signal. As long as the input $E(t)$ signals covered the full amplitude range and included at least two movement pulses, the identified ERS was robust and able to achieve high accuracy for reasonable noise levels and record lengths.

Chapter 5: Methods & Results – Stimulus Response System (SRS)

The SRS model required for the FRCS relies on the ability to predict paralyzed displacement, $\text{Pos}_P(t)$, generated in response to a stimulus amplitude modulation input, $A(t)$. This chapter covers the process of building and evaluating the SRS which involved the following steps:

1. Build a SRS simulation model that generates $\text{Pos}_P(t)$ from $A(t)$,
2. Simulate the signals associated with different movements,
3. Identify a SRS model relating $A(t)$, as input, to $\text{Pos}_P(t)$, as output,
4. Evaluate the performance of the estimated SRS models.

The results indicate that it is possible to identify accurate SRS models with signals of reasonable record length in the presence of noise.

5.1 Methods: Stimulus Response System

The SRS simulation covered in this section is intended to represent the paralyzed side of the face. The model takes the stimulus amplitude modulation signal, $A(t)$, as its input and generates the paralyzed side displacement, $\text{Pos}_P(t)$, as output. This simulation model has three main components:

1. Generation of $A(t)$,
2. Transformation of $A(t)$ to muscle force,
3. Use of the muscle force to predict $\text{Pos}_P(t)$.

Two different types of inputs were used to test the model and produce the simulated outputs required for SRS model identification.

5.1.1 SRS Simulation Model

Stimulus Amplitude Modulation Input

The first step in building the SRS simulation model was to generate an electrical stimulus emulating that used during functional electrical stimulation (FES). Stimulation is delivered as a series of electrical pulses characterized by three parameters: pulse frequency, amplitude, and duration. If the stimulation frequency is too low, the muscle responds with muscle twitches. Above a certain stimulation frequency, the muscle responses overlap and summate to generate a smooth contraction. As discussed in the background section, FES stimuli are usually pulse trains

with a frequency of 20 to 50 Hz, with 12 to 15 Hz as the typical minimum required for summation of muscle twitches [8, 66]. The strength of muscle contraction may also be increased by increasing the number of motor units activated. This is achieved by increasing the stimulus pulse amplitude. In most neuroprostheses, the strength of the muscle contraction is controlled by modulating the pulse amplitude while the stimulus frequency is held constant at a value low enough to avoid muscle fatigue while also high enough to enable muscle tetanus [11, 66]. Therefore, to meet these requirements, we chose a stimulus waveform to be monophasic 50 Hz sinusoid and modulated its amplitude. Since the 50 Hz is constant, the input to our SRS simulation model was a stimulus amplitude modulation signal, $A(t)$. $A(t)$, which is based on a desired displacement signal, was passed into the model where it was multiplied by a 50 Hz sine wave and half wave rectified to get the monophasic 50 Hz stimulus.

For these simulations, the desired displacement signals had an amplitude ranging from 0 mm to 20 mm. This was done in order to accurately estimate the nonlinearity of the system, as will be explained further in the input signals section of this chapter. $A(t)$ was generated by multiplying the desired displacement amplitude by 170 so that the maximum potential voltage of $A(t)$, and subsequently the electrical stimulus, was between 0 and 3.4 volts. These values were somewhat arbitrary. As covered in the background section, the idea with stimulus amplitude is to provide a voltage large enough to achieve the desired motion but small enough to avoid tissue damage or stimulation of pain sensing nociceptors [13]. It has been shown with animal models of facial paralysis that stimuli up to 6.5 volts could achieve the desired movement without signs of discomfort [55]. Therefore, our voltage of 3.4 is within this range but the actual voltage used for facial pacing would need to be determined during experimental trials.

Amplitude Modulation – Force Simulation

Fig. 5-1 shows the Simulink implementation of the stimulus amplitude modulation input, $A(t)$, to muscle force part of the SRS simulation. After simulating the electrical stimulus from $A(t)$, the simulation model generates muscle force using a model based on that described by Bobet and Stein [67]. The model has a LNL structure comprising a cascade of a first order low pass filter (filter 1), a saturation non-linearity, and a second first order low pass filter (filter 2). The components of the model can be linked to underlying mechanisms in the muscle. The first filter

reflects calcium release and reuptake, the static non-linearity reflects the calcium binding by troponin, and the second filter represents the crossbridge dynamics [67]. This model produced results with a low error ($6.3 \pm 0.7\%$ of maximum stimulated force (MSF)) when used to estimate the ankle dorsiflexing torques produced during isometric contractions for a variety of stimulus trains [68].

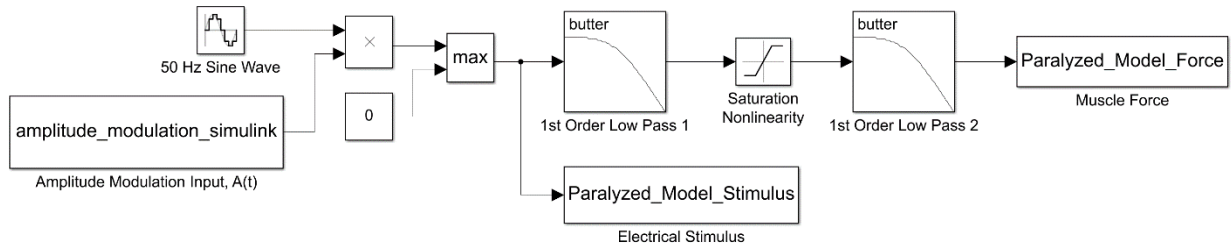


Figure 5-1: Force Simulation (Simulink).

Fig. 5-2 shows $A(t)$, the electrical stimulus, and muscle force generated by the SRS simulation model for a simple movement.

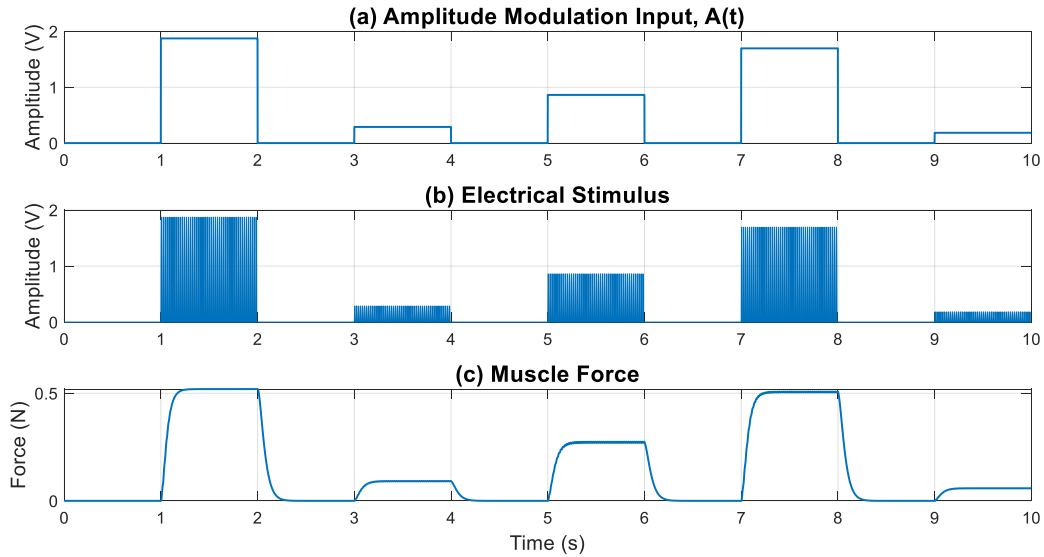


Figure 5-2: Transition from Stimulus Amplitude Modulation Input, $A(t)$, to Muscle Force for a Simple Movement.

Muscle Load Model (Mass-Spring-Damper)

The load model for the SRS simulation was the same mass-spring-damper subsystem used in the ERS simulation. Thus, the mass, spring constant, and damping coefficient were 0.9g, 52.025 N/m

and 6 Ns/m, respectively [69]. Fig. 5-3 shows the Simulink subsystem that simulated the muscle force to paralyzed displacement, $\text{Pos}_P(t)$, portion of the SRS simulation model.

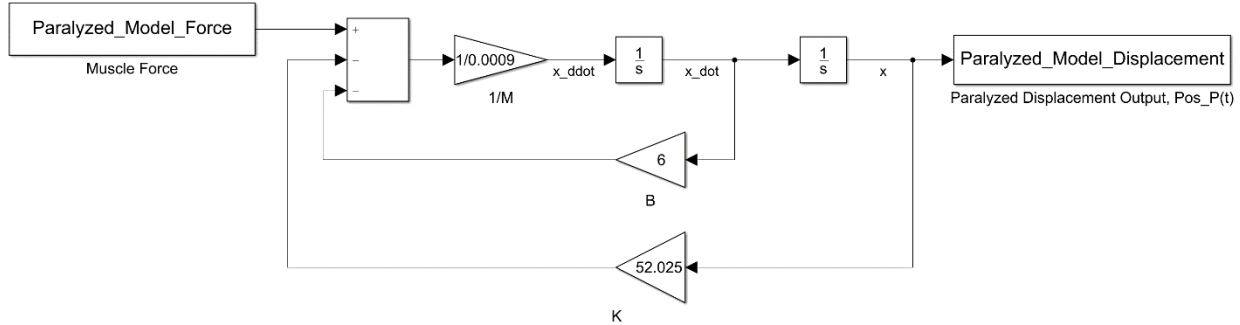


Figure 5-3: Paralyzed Displacement Simulation (Simulink).

Combining the two subsystems created the complete SRS simulation that generated paralyzed displacement, $\text{Pos}_P(t)$, from the stimulus amplitude modulation input, $A(t)$. Fig. 5-4 shows the Simulink diagram for the full SRS simulation model.

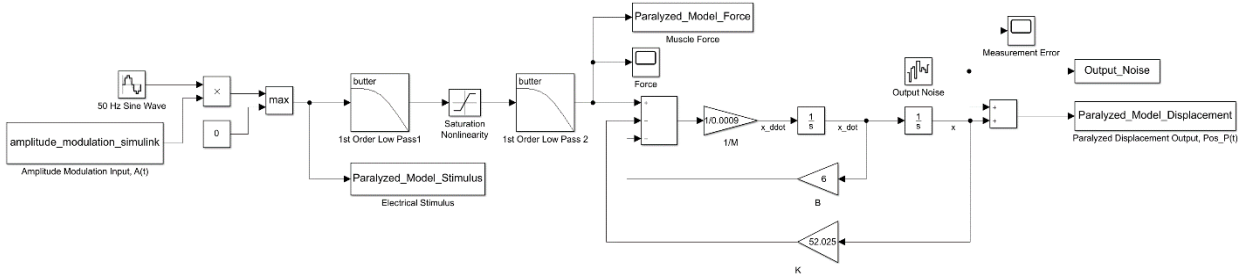


Figure 5-4: SRS Simulation Model (Simulink).

5.1.2 Input Signals

The displacement input signals for the SRS model were similar to those of the ERS model. Once again, we used a modified PRBS input and a “physiological” input. The main difference of the SRS signals was that the maximum potential amplitude was increased to 20 mm. The reason for using a larger desired displacement amplitude than the ERS was due to the saturation nonlinearity of the SRS simulation model. In order to estimate this saturation nonlinearity a larger input was required. Fig. 5-5 shows an example of the modified PRBS waveform for the SRS model.

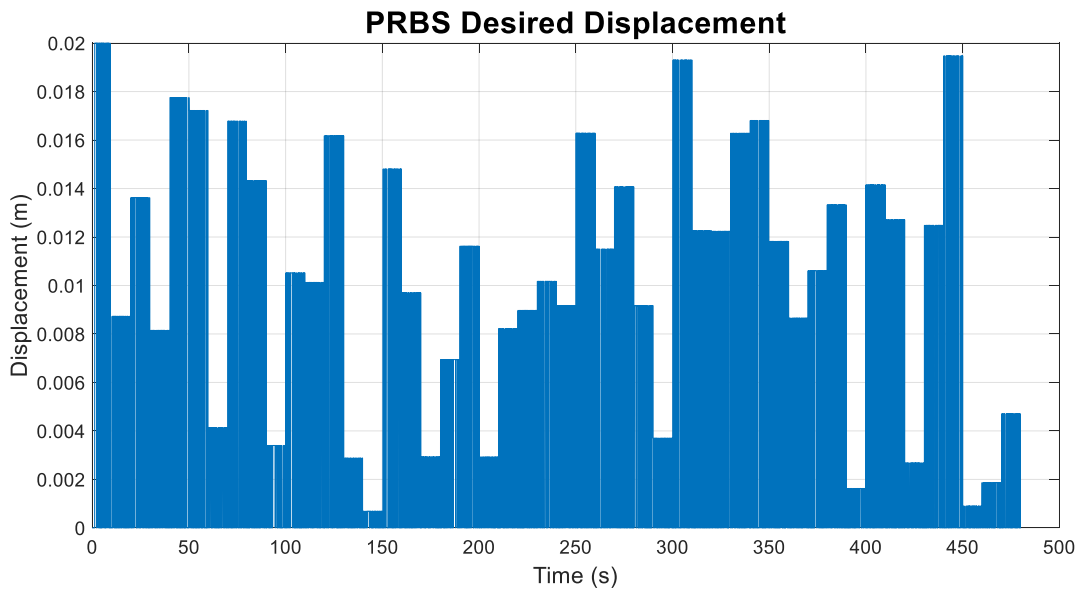


Figure 5-5: Typical Modified PRBS Displacement for the SRS Model.

Once again, a “physiological” input was created to simulate the types of spontaneous and random movements expected in experimental trials with rat models. For the “physiological” input of the SRS model, the random frequencies were sampled from a normal distribution truncated between 0 and 2.1 Hz. The pulse width of the desired displacement was held constant at 450 milliseconds. Fig. 5-6 shows an example of the “physiological” input for the SRS model.

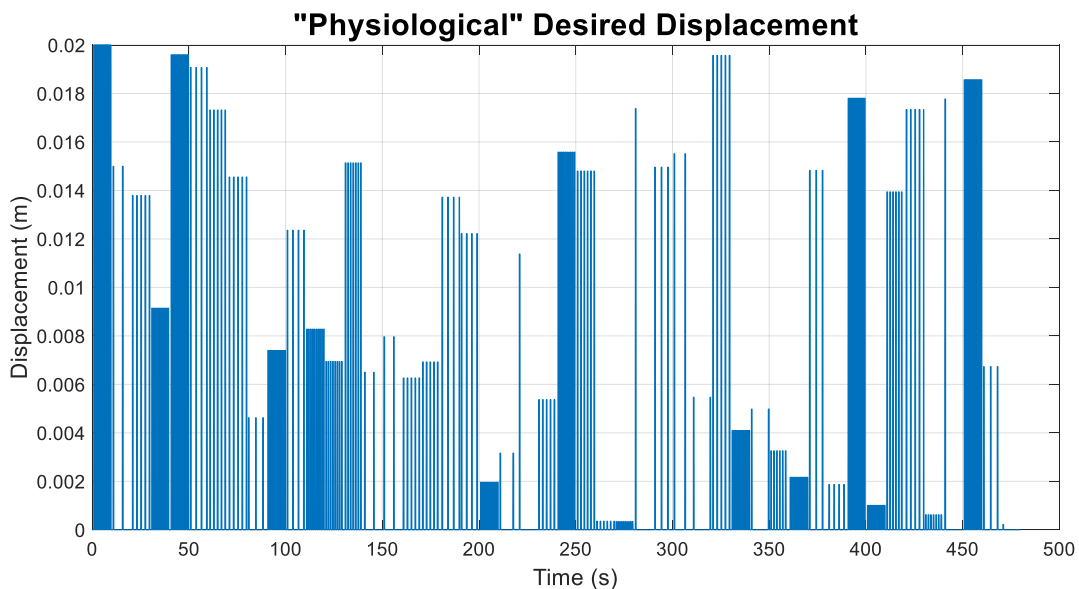


Figure 5-6: Typical “Physiological” Displacement for the SRS Model.

5.1.3 Model Identification

With the SRS simulation completed and a paralyzed displacement signal, $\text{Pos}_P(t)$, generated in response to a stimulus amplitude modulation input, $A(t)$, we could identify the SRS model needed for the FRCS. For the SRS, a Wiener model was identified between $A(t)$ and $\text{Pos}_P(t)$ using an iterative identification method developed by Hunter and Korenberg known as the HK method [64]. This was implemented using the MATLAB NLID toolbox developed by Dr. Kearney [65].

5.2 Results: Stimulus Response System

5.2.1 Simulation and Identification with PRBS Inputs

Fig. 5-7 shows an example of the desired displacement, stimulus amplitude modulation input, $A(t)$, muscle force, and output paralyzed displacement, $\text{Pos}_P(t)$, for a typical trial of the SRS simulation model with a PRBS input.

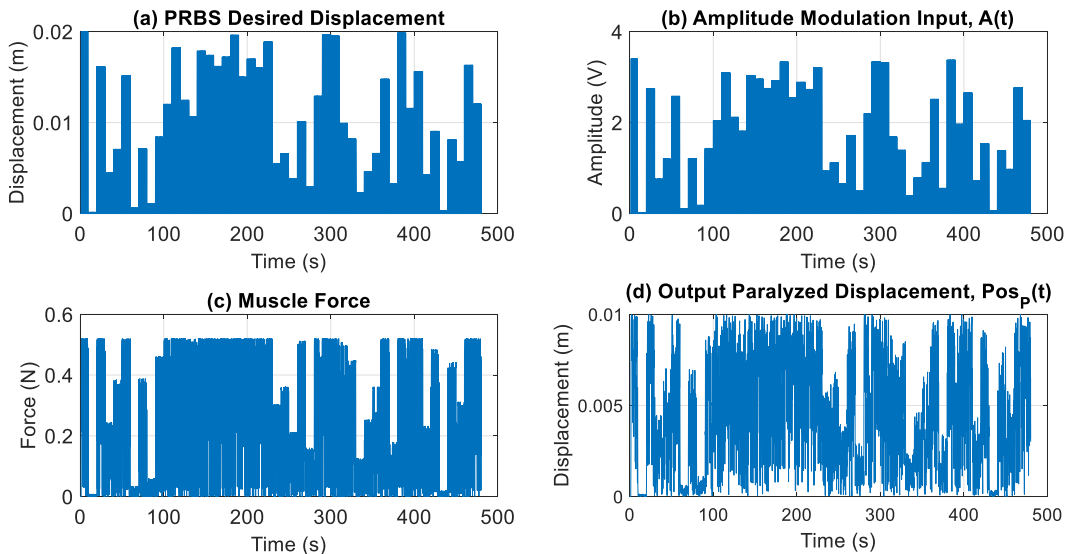


Figure 5-7: PRBS Signal for the SRS Simulation; (a) Desired displacement, (b) Stimulus amplitude modulation input, $A(t)$, based on desired displacement, (c) Muscle force, (d) Output paralyzed displacement, $\text{Pos}_P(t)$.

With a simulated $\text{Pos}_P(t)$, the next step was to identify the SRS model between the $A(t)$ and $\text{Pos}_P(t)$.

Fig. 5-8 shows the Wiener model identified between $A(t)$ and $\text{Pos}_P(t)$ from Fig. 5-7. The model consists of a linear element followed by a static nonlinearity. The linear element in Fig. 5-8a resembles a low pass filter while the static nonlinearity in Fig. 5-8b appears roughly linear for

low inputs/output but begins to saturate as it approaches a paralyzed displacement output, $\text{Pos}_P(t)$, of 10 mm.

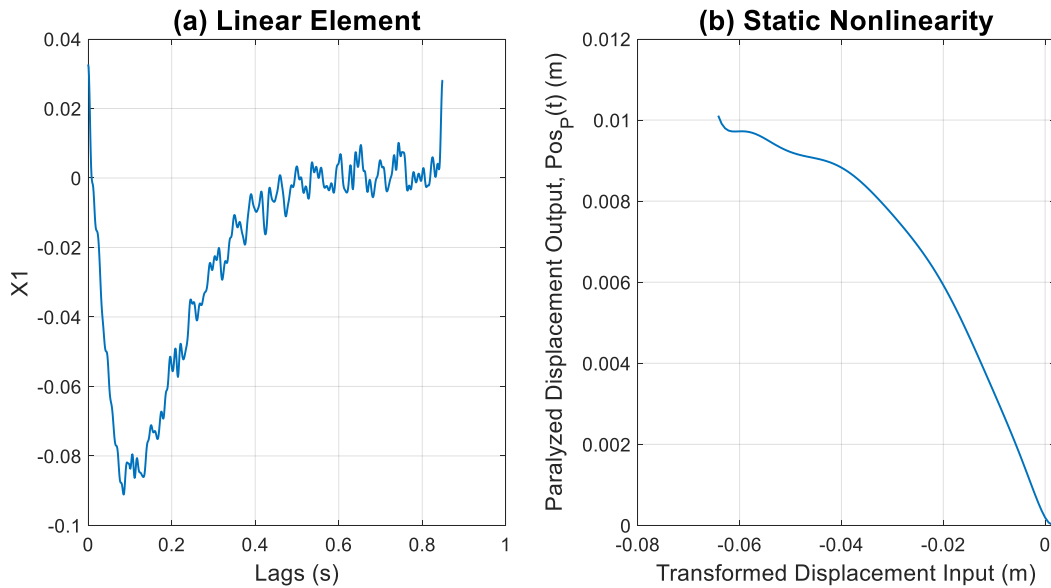


Figure 5-8: Identified SRS Wiener Model using a PRBS Input.

The identified Wiener model performed well when used to predict $\text{Pos}_P(t)$ from $A(t)$, as Fig. 5-9 shows, with a VAF of 97.7%.

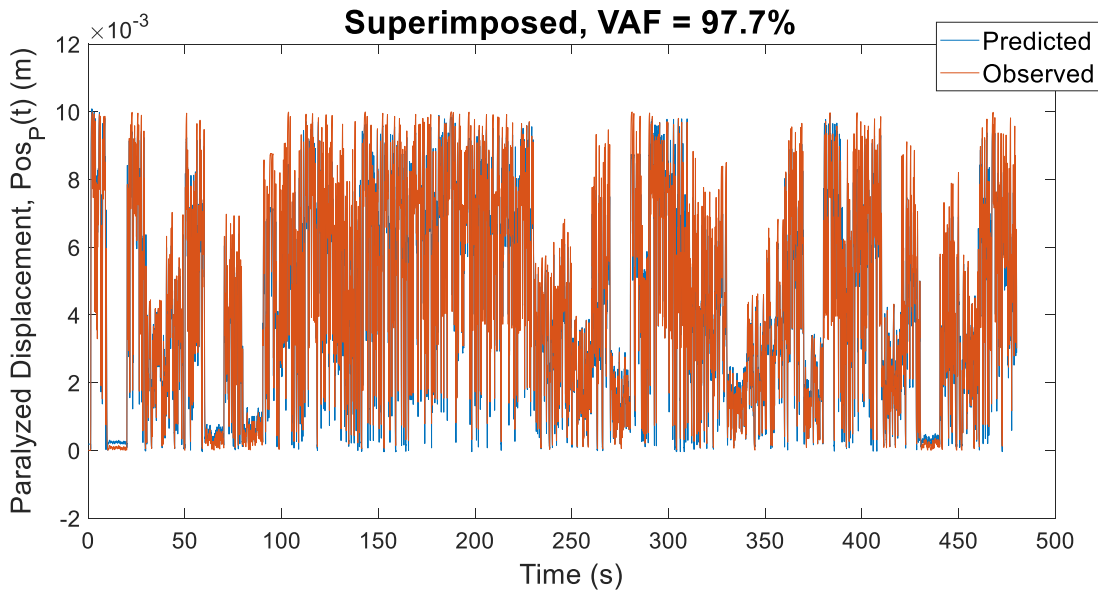


Figure 5-9: Accuracy of Model Identification.

Fig. 5-10 examines the residuals of the SRS model. Fig. 5-10b shows the residual probability distribution was concentrated around zero and relatively evenly distributed in both directions. Fig. 5-10c shows the power spectrum of the residuals which illustrates that the errors were concentrated at low frequencies. Besides a power spike near 0 Hz, there was no other frequency with significant power.

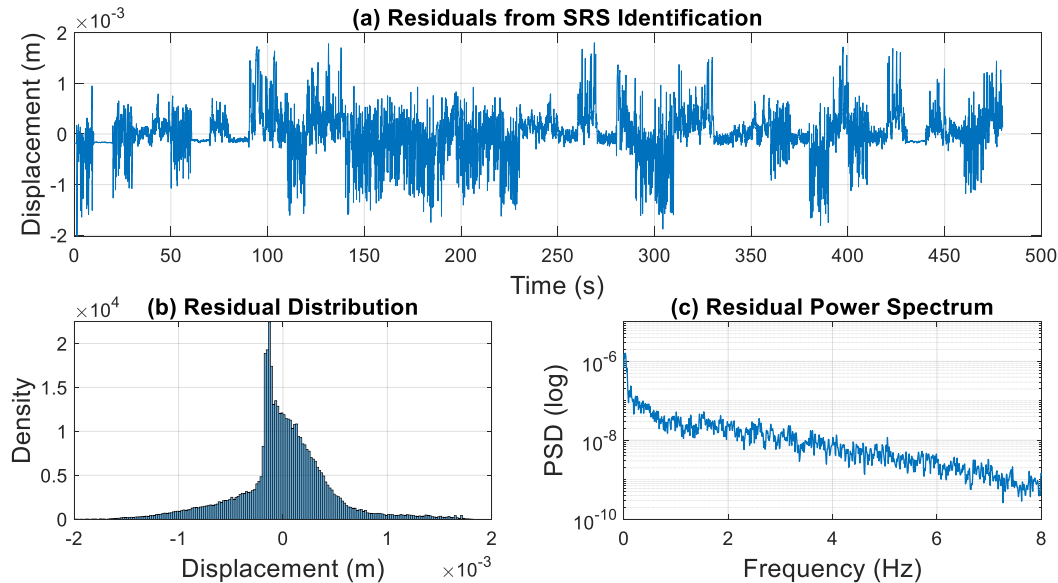


Figure 5-10: Residual Analysis of Model Identification.

5.2.2 Simulation and Identification with “Physiological” Inputs

Fig. 5-11 shows an example of the desired displacement with the resulting stimulus amplitude modulation input, $A(t)$, muscle force and output paralyzed displacement, $P_{\text{osp}}(t)$, of the SRS simulation for a typical trial with a “physiological” input.

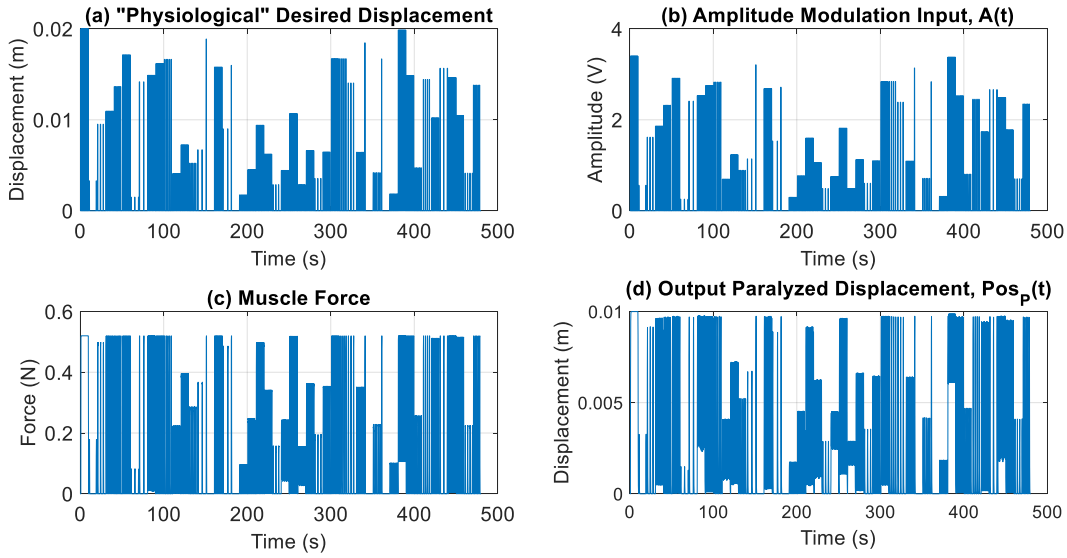


Figure 5-11: "Physiological" Signal for SRS Simulation; (a) Desired displacement, (b) Stimulus amplitude modulation input, $A(t)$, based on desired displacement, (c) Muscle force, (d) Output paralyzed displacement, $Pos_P(t)$.

Fig. 5-12 shows the identified Wiener model between $A(t)$ and $Pos_P(t)$ in Fig. 5-11. This model has a similar structure as the model identified with a PRBS input. The linear element in Fig. 5-12a resembles a low pass filter while the static nonlinearity in Fig. 5-12b appears roughly linear for low inputs/outputs but begins to saturate as it approaches a paralyzed displacement output, $Pos_P(t)$, of 10 mm.

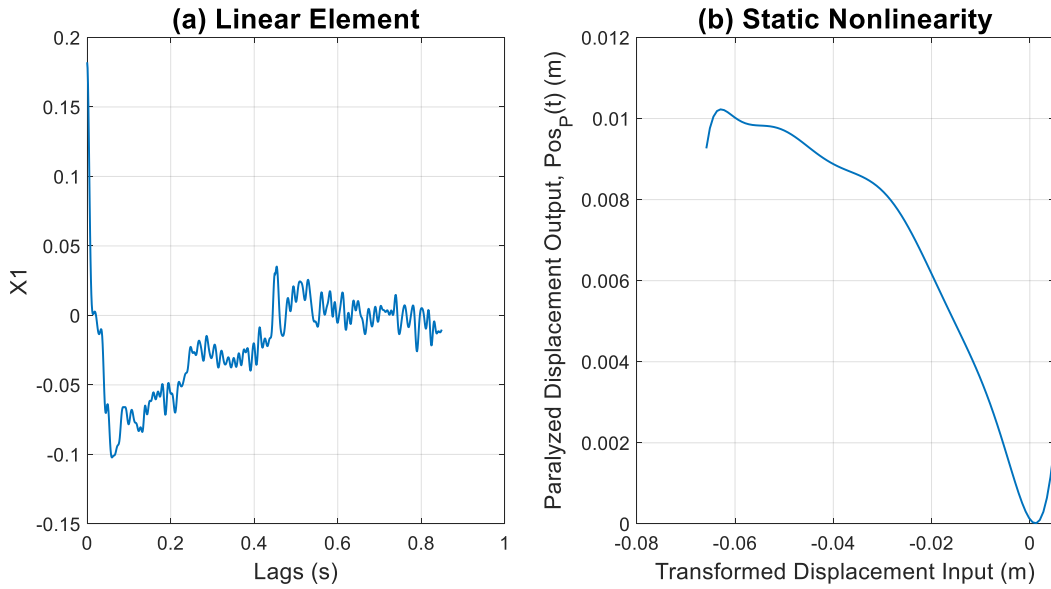


Figure 5-12: Identified SRS Wiener Model using a "Physiological" Input.

The identified Wiener model performed well when used to predict the $\text{Pos}_P(t)$ from $A(t)$. Fig. 5-13 shows that the identified model achieved a VAF of 98.6% for this example.

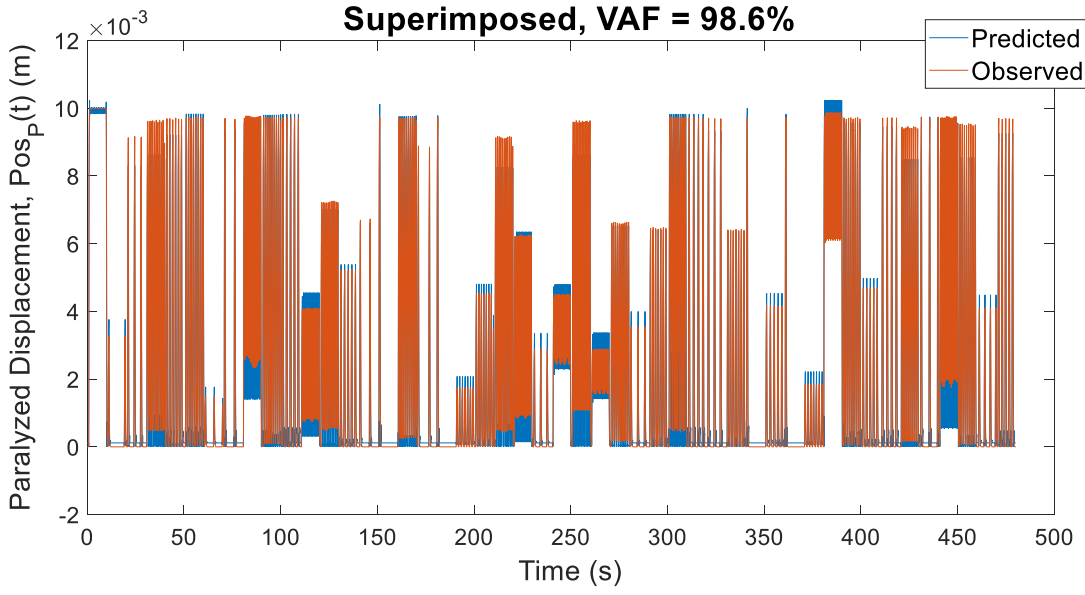


Figure 5-13: Accuracy of Model Identification.

Fig. 5-14 examines the residuals of the model. Fig. 5-14b shows the residual probability distribution was centered around zero but indicates with the largest bin that the model prediction had a consistent offset when predicting a displacement of zero. This can be seen when

referring back to the superimposed displacements in Fig. 5-13. Fig. 5-14c shows the power spectrum of the residuals with a spike at 0 Hz but then levels off and is almost white up until 3 Hz.

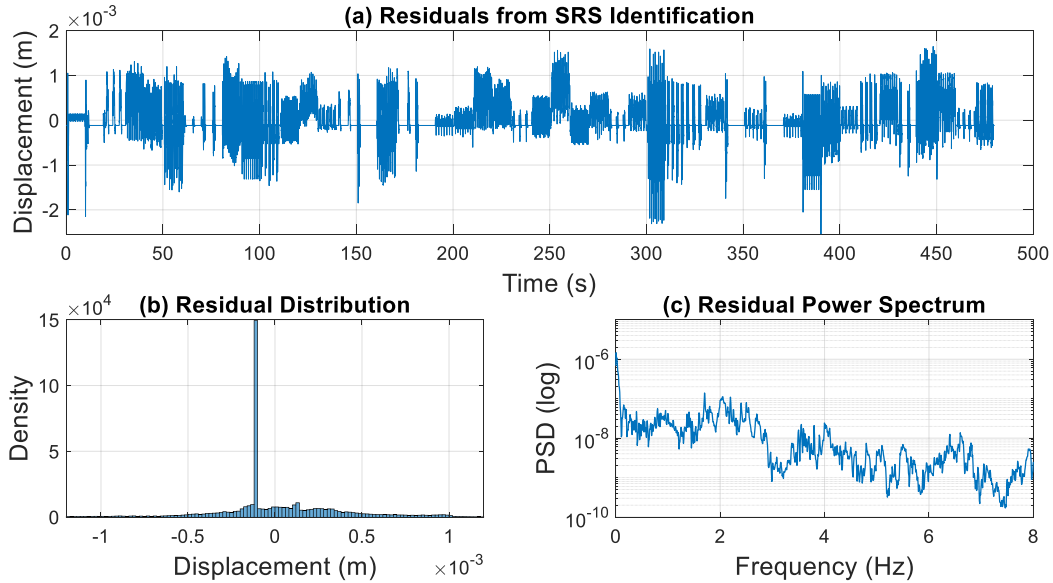


Figure 5-14: Residual Analysis of Model Identification.

Finally, Fig. 5-15 compares the two identified SRS models from Figs. 5-8 and 5-12 illustrating that both models had similar structure for the linear and nonlinear elements.

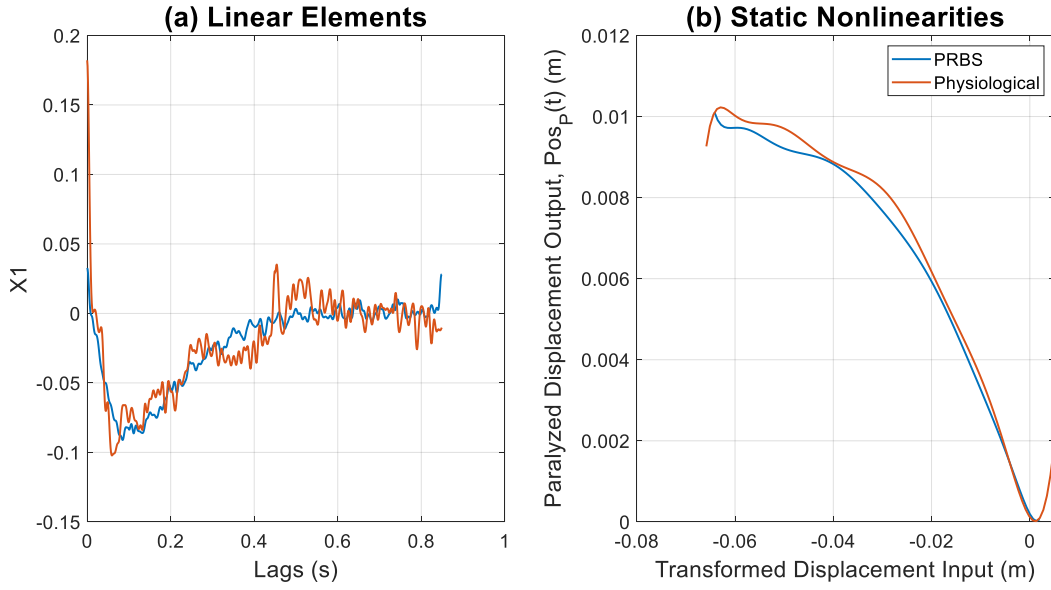


Figure 5-15: Comparison of SRS Wiener Models Identified from Different Input Types.

5.2.3 Model Validation

To validate the identified SRS models, the models were used to predict the movements generated in response to an input realization different than that used to identify the model. SRS models identified with both types of input signals were tested. First, a model was tested with another realization of the same type of signal used to identify the model. Then, the model was tested with the other signal type not used for the model identification.

First, the SRS model identified from the PRBS was validated. When used to predict $\text{Pos}_P(t)$ of another realization of the PRBS signal the model achieved a VAF of 97.6%. Fig. 5-16 shows the results of this validation trial with residuals similar to those seen during model identification with a PRBS input.

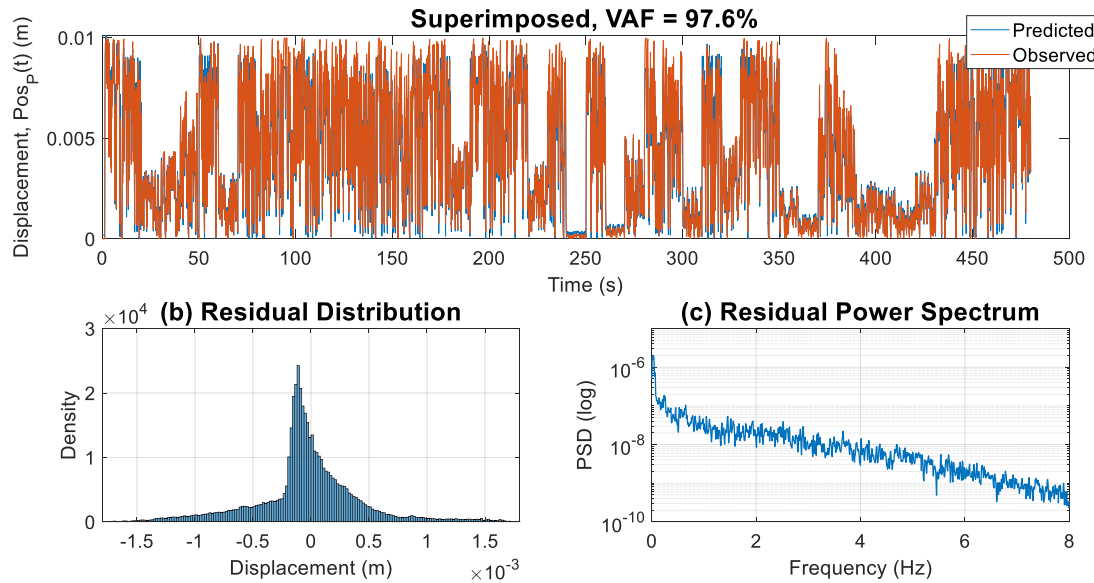


Figure 5-16: Results of PRBS identification & Validation.

When this model was used to predict $\text{Pos}_P(t)$ of a “physiological” signal it achieved a VAF of 97.7%. Fig. 5-17 shows the results for this trial. Since the PRBS input used to identify the model was a rich input, the model was very robust, which lead to a high validation accuracy even when the input signal was different. The residual distribution shows the constant offset of the model when predicting a zero meter displacement. The spectrum in Fig. 5-17c shows that there is a spike near 0 Hz but levels off and is almost white up until 3 Hz.

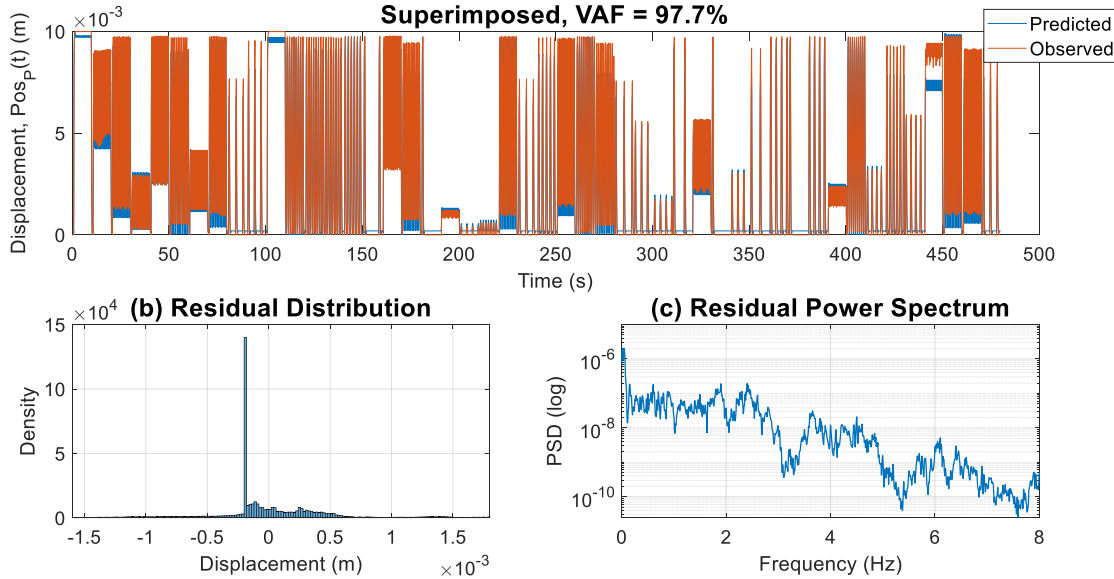


Figure 5-17: Results of PRBS identification & “Physiological” Signal Validation.

Next, the SRS model identified with the “physiological” input was validated. When using the model to predict $\text{Pos}_P(t)$ of another realization of the “physiological” input the model achieved a VAF of 98.3%. Fig. 5-18 shows the results of this trial. These results were very similar to those seen during the model identification with a “physiological” input.

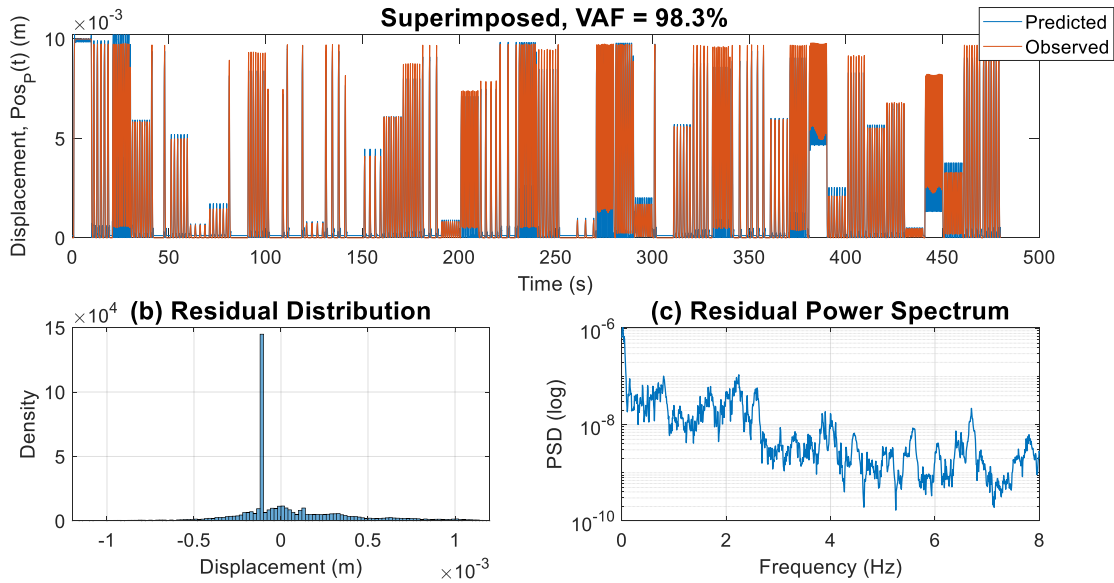


Figure 5-18: Results of “Physiological” Signal Identification & Validation.

Fig. 5-19 shows that when this model was used to predict $\text{Pos}_P(t)$ of a PRBS input signal the model achieved a VAF of 95.5%. The residual distribution shows the errors were evenly distributed around zero meters. The spectrum of the residuals shows that there is a power spike near 0 Hz and no other significant power spike at other frequencies.

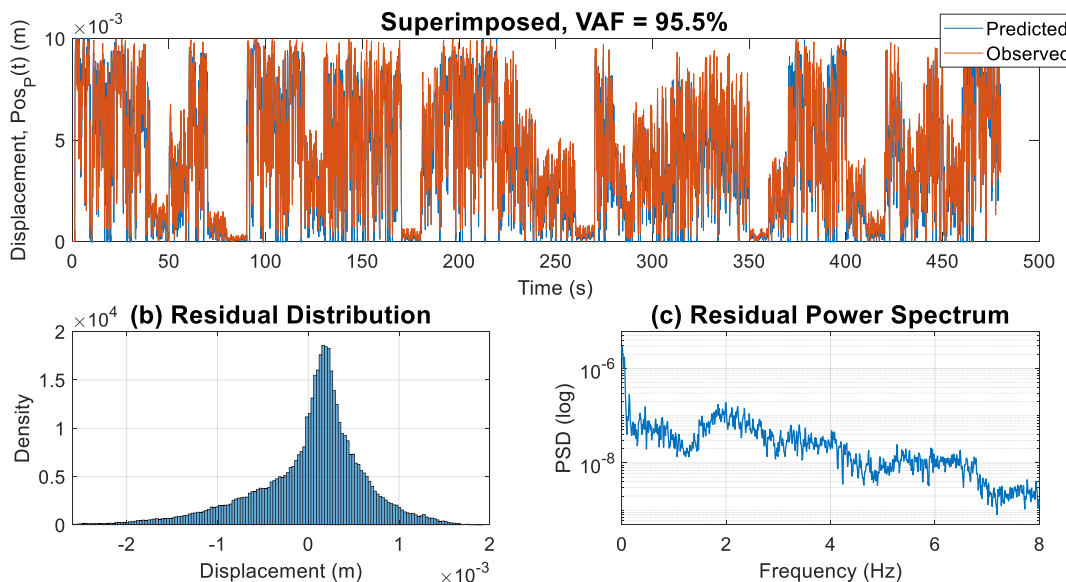


Figure 5-19: Results of “Physiological” Signal Identification & PRBS Validation.

Table 5-1 provides the VAF mean and standard deviation for each model over 30 validation trials. Overall, the SRS models performed well, regardless of the type of signal used when identifying the model. In general, the residual distributions were centered around zero. The exception to this is the offset seen when trying to predict a “physiological” displacement. The residual spectrums are not white but besides a spike near 0 Hz, there were no other frequencies with significant power.

Table 5-1: Average Model Accuracies during Model Validation.

SRS Model Accuracy		
	Signal Used for SRS Model Identification	
Signal Used for Model Validation	PRBS	Physiological
PRBS	$97.6 \pm 0.5\%$ VAF	$96.3 \pm 0.7\%$ VAF
Physiological	$98.5 \pm 0.3\%$ VAF	$98.7 \pm 0.4\%$ VAF

5.2.4 Input Signal Limitations

Once again, there were some limits on the signals used for SRS model identification. It was important that the amplitude of the input signal used for model identification covered the full range of potential input values. This is demonstrated in Fig. 5-20, where constant amplitude PRBS signals of decreasing maximum amplitude were used for SRS model identification. These models were then validated with 30 realizations of “physiological” inputs in order to calculate the VAF mean and standard deviation. As demonstrated in the figure, when the identification signal amplitude decreased there came a point where the SRS model performed poorly during validation. In this case, the limit was around 18.5 mm.

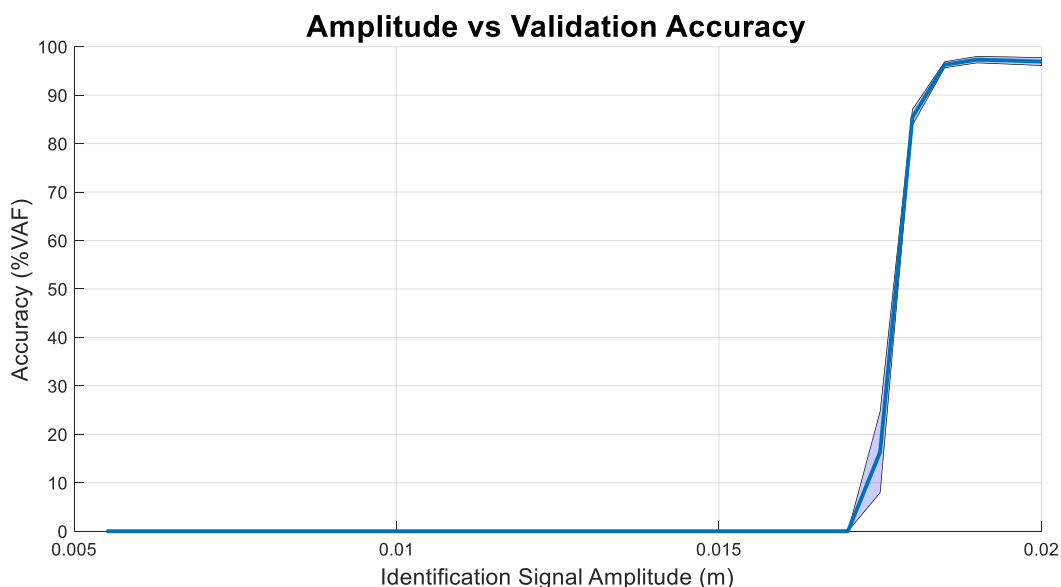


Figure 5-20: Amplitude vs Validation Accuracy; Average validation accuracy (solid blue line) and standard deviation of validation accuracy (shaded blue area).

Another area of concern was the minimum number of movements required to create a robust model with high and consistent validation accuracy. To quantify this, 30 modified “physiological” inputs, each with a different number of movement pulses, were used to identify SRS models. The first modified “physiological” input had only one movement pulse, with each subsequent input increasing the number of movement pulses by one. The SRS models identified from these signals were then validated with 30 realizations of “physiological” inputs to calculate the mean VAF and its standard deviation. Fig. 5-21 shows that the SRS model required a minimum of 25 movement pulses in the identification signal to achieve an average VAF of 86%.

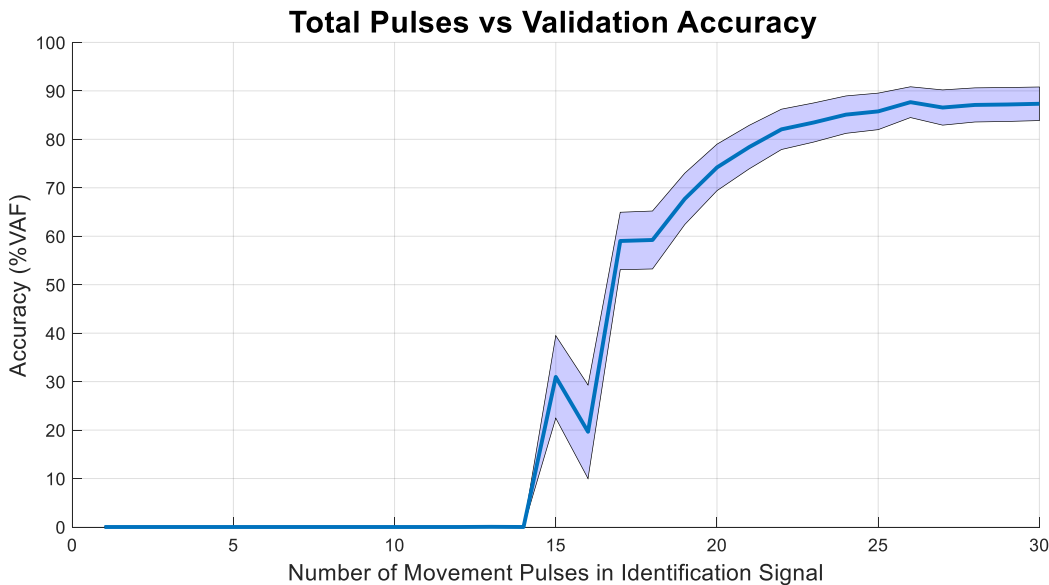


Figure 5-21: Total Pulses vs Validation Accuracy; Average validation accuracy (solid blue line) and standard deviation of validation accuracy (shaded blue area).

5.2.5 Noise and Record Length

Once again, we wanted to test the SRS model when white noise was added to the output, simulating measurement error. With the noise added to the SRS simulation model we could determine how much noise was acceptable while still maintaining a high SRS model accuracy.

For this experiment we examined how different levels of noise effect the accuracy of the SRS model during model validation. Two different signals were used to identify the SRS models used during these trials: a PRBS and a “physiological” signal. First, a “clean” $\text{Pos}_P(t)$ signal was generated from the SRS simulation model using both input types. Then, a set of SRS models were identified for each type of input, at steadily increasing levels of output noise. Fig. 5-22 shows the identification accuracy for these models. The identification accuracy was calculated by comparing the predicted $\text{Pos}_P(t)$ of the identified SRS models to the “clean” $\text{Pos}_P(t)$, before noise was added. The identification accuracy remained high for both types of models, only beginning to drop off below a signal to noise (SNR) of -16 dB, with the “physiological” model having slightly better tolerance to the added noise.

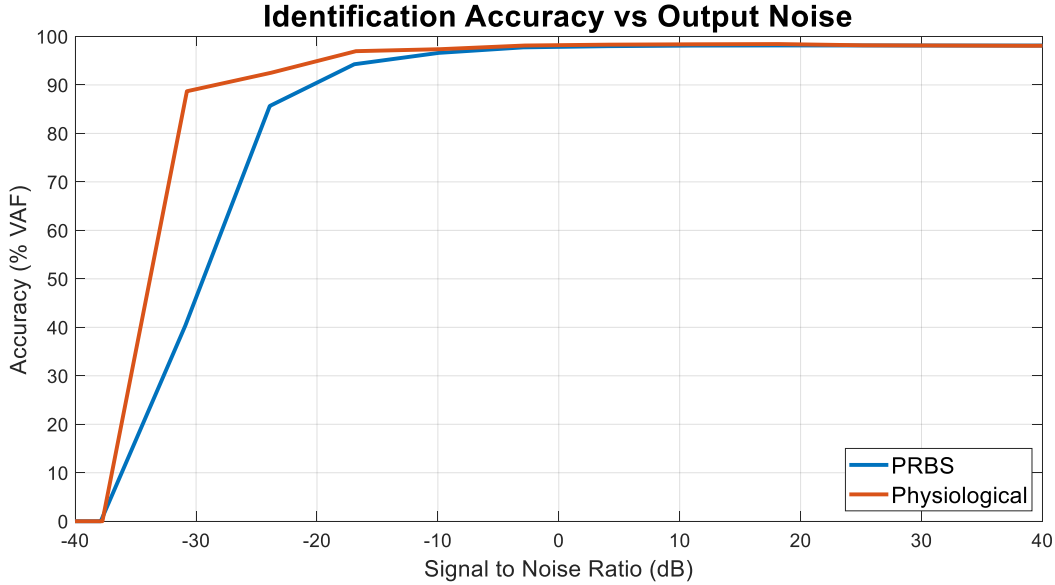


Figure 5-22: Identification Accuracy vs Output Noise for Two different Signal Types.

These identified SRS models were then validated over 30 trials with “physiological” signals. Fig. 5-23 shows the average validation accuracy of these trials. Similar to the identification accuracies, both model types achieved high validation accuracies for SNR values above -16 dB indicating that the models were very tolerant to output noise.

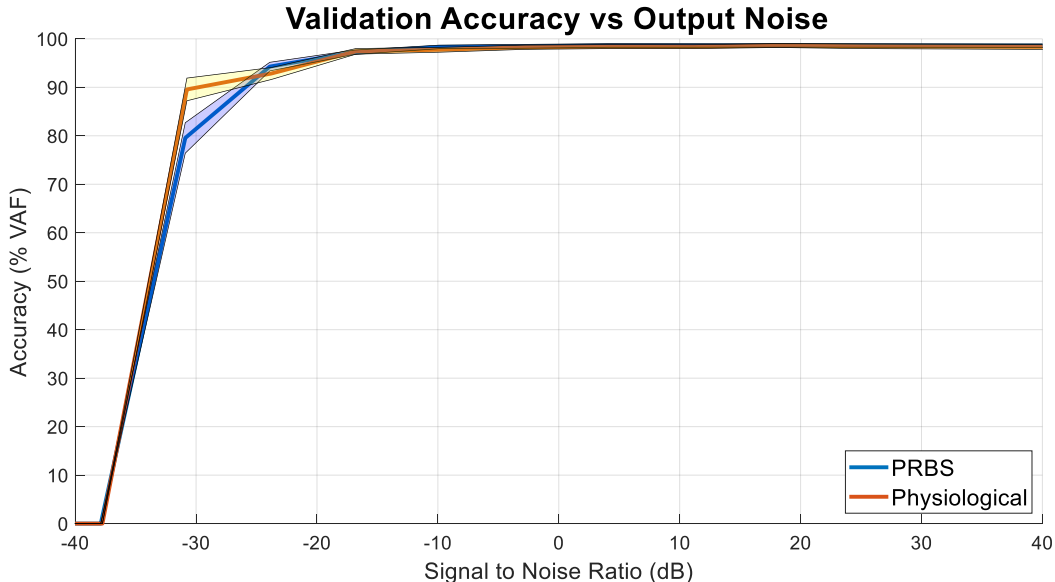


Figure 5-23: Validation Accuracy vs Output Noise for Two different Signal Types; Average validation accuracy (solid lines) and standard deviation of accuracy (shaded areas)

Next, the effects of the identification signals record length on the SRS models accuracy was tested. For the following experiment, PRBS signals of increasing record length were used for SRS model identification. These models were then validated with “physiological” signals over 30 trials to see how the identification signals record length effected the validation accuracy. Fig. 5-24 shows the average validation accuracy for these trials. The results show that the SRS model required a minimum record length of 13 seconds to achieve an average VAF of 96%.

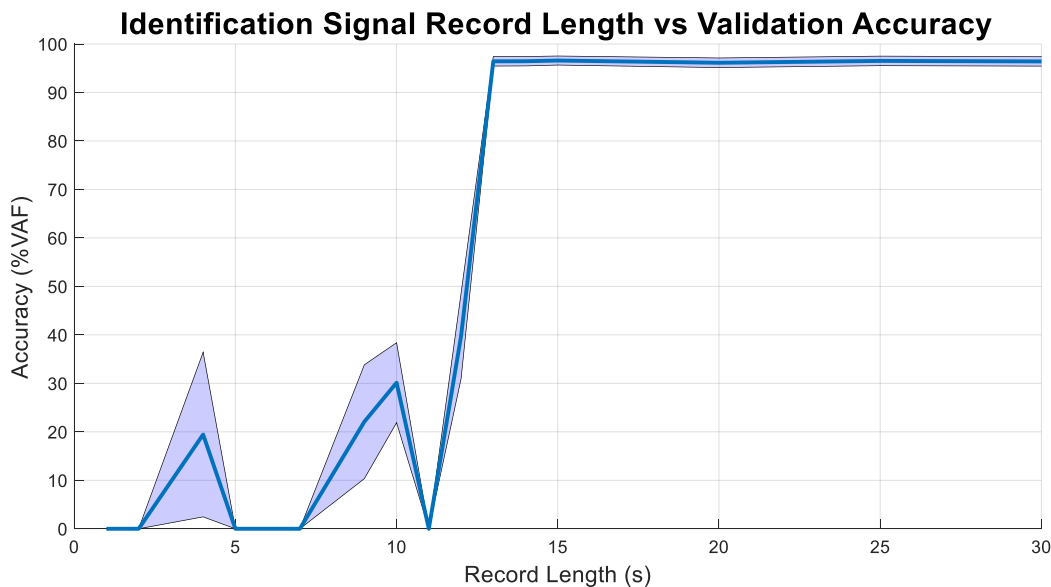


Figure 5-24: Identification Signal Record Length vs Validation Accuracy; Average validation accuracy (solid line) and standard deviation of accuracy (shaded area)

Summary

This chapter outlined a process of identifying the SRS using simulated data. To acquire the simulated data, a SRS simulation model that represents the paralyzed side of the face was created that produced paralyzed displacement signals, $\text{Pos}_P(t)$, from various stimulus amplitude modulation inputs, $A(t)$. The identified SRS was able to accurately estimate the $\text{Pos}_P(t)$ from $A(t)$. As long as the $A(t)$ signals covered the full amplitude range and included at least 25 movement pulses, the identified SRS was robust and able to achieve high accuracy for reasonable noise levels and record lengths.

Chapter 6: Methods & Results - Facial Reanimation Control System

The previous chapters developed two models: the EMG response system (ERS) which models an EMG input, $E(t)$, to a healthy displacement output, $Pos_H(t)$, and represents the healthy side of the face; and the stimulus response system (SRS) which models a stimulus amplitude modulation input, $A(t)$, to a paralyzed displacement output, $Pos_P(t)$, and represents the paralyzed side of the face. This section describes how the identified ERS and SRS were combined to create a facial reanimation control system (FRCS). It also describes simulation studies of its performance.

6.1 Methods: Facial Reanimation Control System

The ERS and SRS models identified from “physiological” inputs were used to build the FRCS since only these models are what would be available in practice.

Fig. 6-1 shows a typical ERS model identified from a “physiological” input.

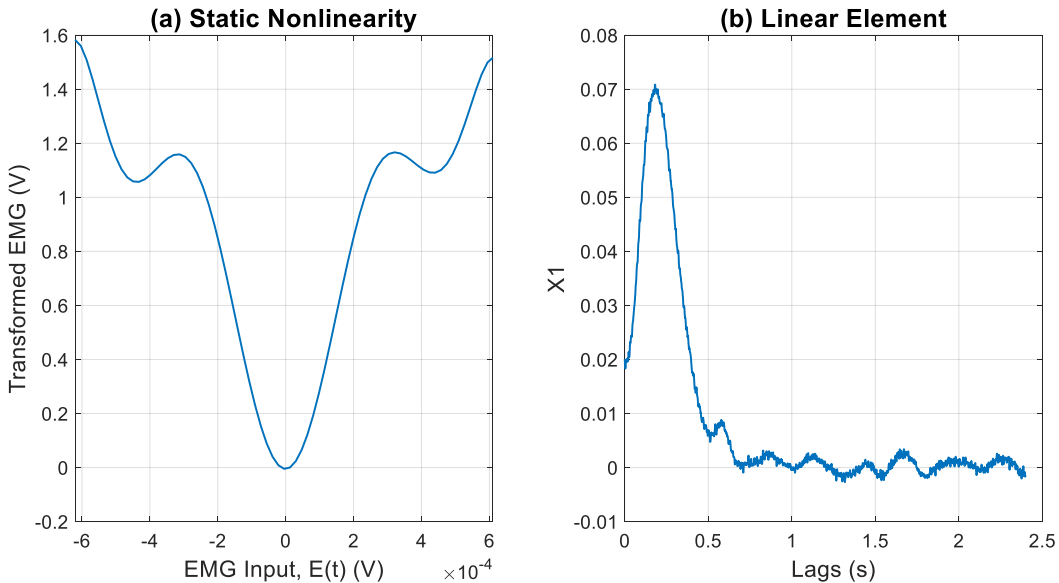


Figure 6-1: Identified Hammerstein ERS for “Physiological” Input.

Fig. 6-2 shows a typical SRS model identified from a “physiological” input.

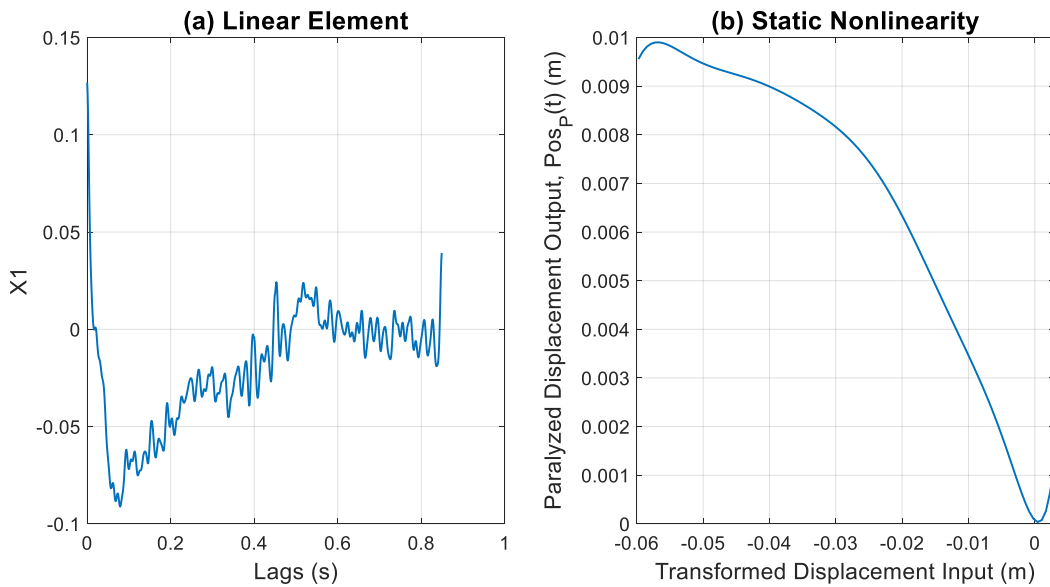


Figure 6-2: Identified Wiener SRS for the “Physiological” Input.

Fig. 6-3 shows a block diagram of the FRCS combined with the SRS simulation model that outputs predicted paralyzed displacement, $\text{Pos}_P(t)$, from an EMG input, $E(t)$. The process to build and evaluate the FRCS proceeds as:

1. Estimate SRS^{-1} , the inverse of the SRS.
2. Use the ERS to estimate the healthy side displacement, $\text{Pos}_H(t)$, from the healthy side EMG, $E(t)$.
3. Filter this $\text{Pos}_H(t)$ with SRS^{-1} to generate the stimulus amplitude modulation signal, $A(t)$, needed to generate the same displacement on the paralyzed side.
4. Apply $A(t)$ to the SRS simulation model to generate the paralyzed displacement, $\text{Pos}_P(t)$.
5. Evaluate the performance by comparing $\text{Pos}_P(t)$ to $\text{Pos}_H(t)$.

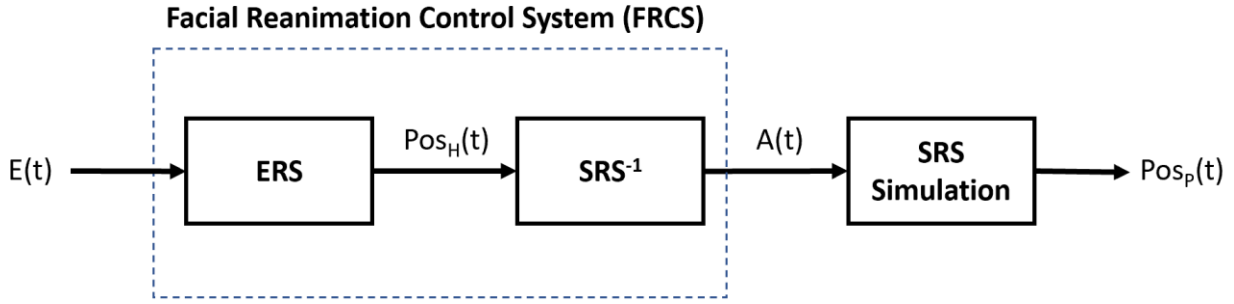


Figure 6-3: Facial Reanimation Control System; Healthy side EMG, $E(t)$, is passed through the ERS to estimate the healthy displacement, $Pos_H(t)$, which is used as the input to the SRS^{-1} to estimate the stimulus amplitude modulation signal, $A(t)$. $A(t)$ is then passed through the SRS simulation model to estimate the predicted paralyzed displacement, $Pos_P(t)$.

7.1.1 Estimating the Inverse of the Stimulus Response System (SRS^{-1})

The inverse of the SRS model, SRS^{-1} , was estimated as follows:

1. A modified PRBS signal with a maximum amplitude that randomly changed every 10 seconds to a value between 0 and 3.4 was passed through the identified SRS model to generate a simulated output. A variable amplitude signal was used to excite the full range of the SRS static nonlinearity to estimate it accurately. Fig. 6-4 shows this amplitude modulation input, $A(t)$, and resulting paralyzed displacement, $Pos_P(t)$, for a typical simulation trial.

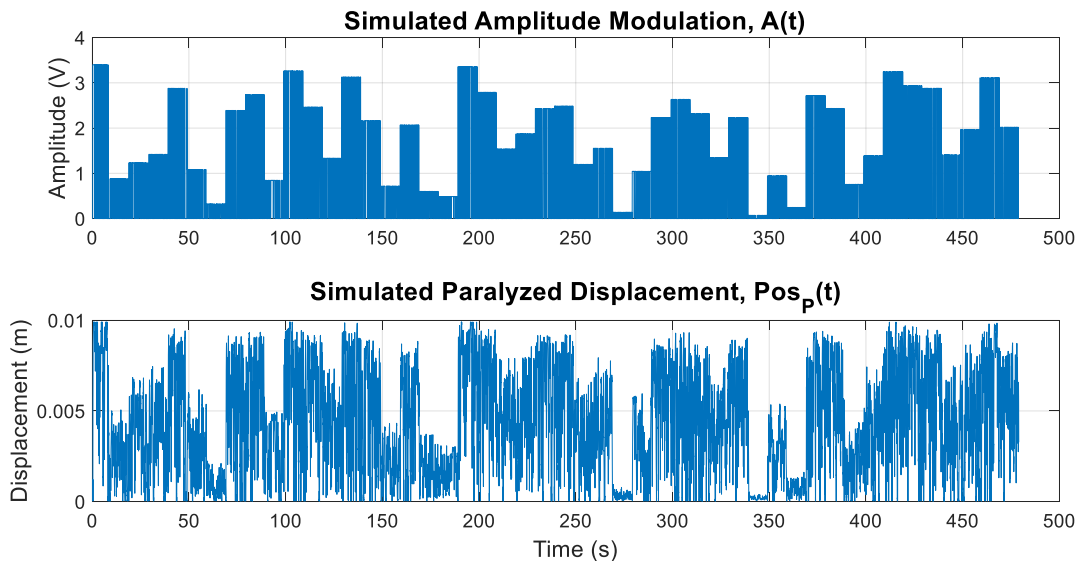


Figure 6-4: Simulated Amplitude Modulation, $A(t)$, and Simulated Paralyzed Displacement Signal, $Pos_P(t)$ used to Identify SRS^{-1} .

2. The SRS⁻¹ was estimated using $\text{Pos}_P(t)$, as the input, and $A(t)$, as the output. Four possible model structures for the SRS⁻¹ were evaluated: a LNL model, a Hammerstein model, a Wiener model, and a linear IRF model. Since we are reversing the input/output relation, we estimated two-sided models for SRS⁻¹.
3. The performance of different estimates of SRS⁻¹ were evaluated in terms of their VAF with both the identification data and with validation data. The validation signals were different realizations of $\text{Pos}_P(t)$ and $A(t)$ as shown in Fig. 6-4.

7.1.2 Facial Reanimation Control System Output

The FRCS was tested by applying various EMG signals, $E(t)$, into the system and examining the outputs. To do this, we used the ERS simulation model to generate $E(t)$ signals for various “physiological” inputs. Once $E(t)$ was generated, the process of testing and evaluating the FRCS follows the process outlined in Fig. 6-3:

1. $E(t)$ was passed through the identified ERS to get healthy displacement, $\text{Pos}_H(t)$, which was then used as the input to the SRS⁻¹ to get the stimulus amplitude modulation signal, $A(t)$.
2. The resulting $A(t)$ was passed through the SRS simulation model to get an estimate of predicted paralyzed displacement, $\text{Pos}_P(t)$.
3. The VAF between $\text{Pos}_P(t)$ and $\text{Pos}_H(t)$ was used to evaluate the accuracy for the FRCS.

This process was repeated for 100 realizations of $E(t)$ to get an average performance of the FRCS.

6.2 Results: Facial Reanimation Control System

Inverse Model Structure

When identifying the SRS⁻¹ structure, one of the parameters required is the number of lags (NLags) in the IRF(s) of the model. Larger values of NLags will produce higher accuracy at a cost of computational efficiency and can result in modeling the noise of the system. For the SRS⁻¹ we iterated through various NLags and looked at the identification and validation accuracy. Fig. 6-5 shows these accuracies compared to NLags for the Hammerstein SRS⁻¹. We can see that there are two elbows at 400 and 800 Nlags where there is a significant change in the rate of accuracy improvement. We wanted to choose a NLags that is a good balance between accuracy and

computational efficiency. Therefore, 400 NLags was a good choice as the rate of accuracy improvement slows down significantly above 400 NLags.

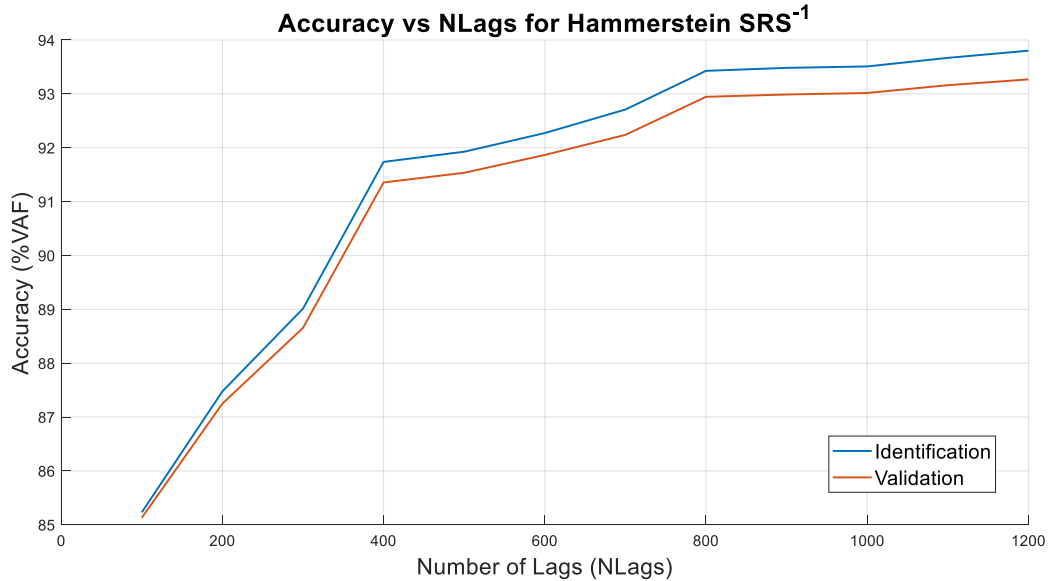


Figure 6-5: Accuracy vs Number of Lags (NLags) for the Hammerstein SRS^{-1} .

Table 6-1 compares the performance of the four model structures tested for use as the SRS^{-1} . The number of free parameters for each structure was the sum of the NLags in the IRF(s) and the order of the static nonlinearity. The model identification VAF is the accuracy achieved during model identification. The model validation VAF is the accuracy of the identified model when tested on signals not used for identification.

Table 6-1: Variance Accounted For (VAF) achieved during SRS^{-1} Identification and Model Validation Trials.

	LNL	Hammerstein	Wiener	Linear IRF
# of Free Parameters	411	410	410	400
Model Identification VAF (mean ± std)	$91.5 \pm 0.3\%$	$91.5 \pm 0.3\%$	$86.2 \pm 0.8\%$	$80.4 \pm 1.0\%$
Model Validation VAF (mean ± std)	$91.3 \pm 0.6\%$	$91.3 \pm 0.6\%$	$82.6 \pm 1.4\%$	$78.2 \pm 2.1\%$

The Hammerstein model performed significantly better than the Wiener or IRF model. The Hammerstein and LNL model had the same performance as the input linear element of the LNL had little effect on the model, essentially making it a Hammerstein model. Furthermore, the Hammerstein model had fewer free parameters than the LNL model. Consequently, we opted to

focus our efforts on the two-sided Hammerstein model. Fig. 6-6 shows an example of a two-sided Hammerstein model identified for the SRS^{-1} .

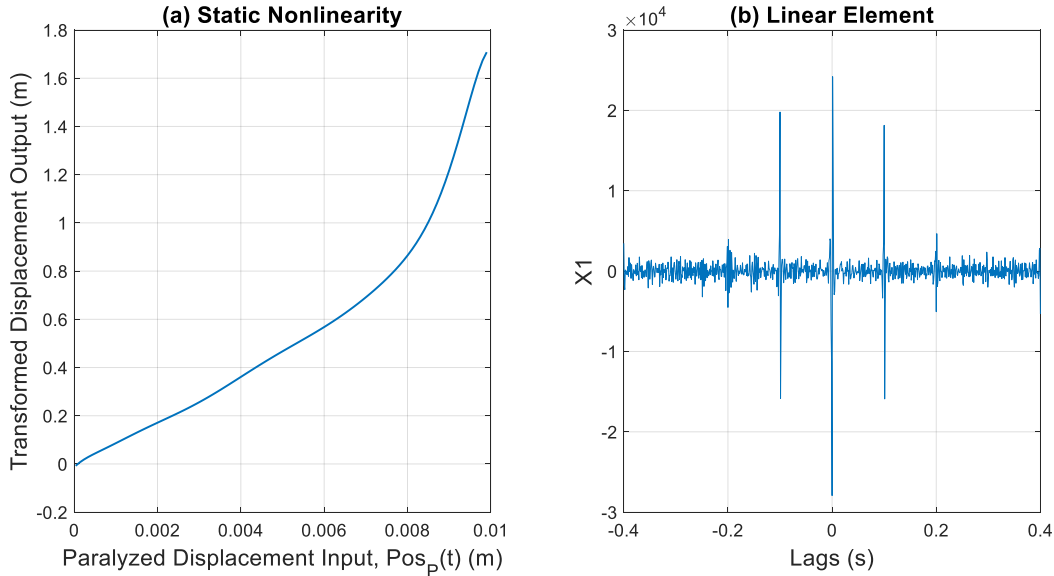


Figure 6-6: Example of a Two-Sided Hammerstein Model used as the SRS^{-1} .

6.2.1 Estimating the Inverse of the Stimulus Response System (SRS^{-1})

Fig. 6-7 shows the signals used to identify the SRS^{-1} , the estimated two-sided Hammerstein model, the identification results, and the residuals. The identification achieved a VAF of 90.3%.

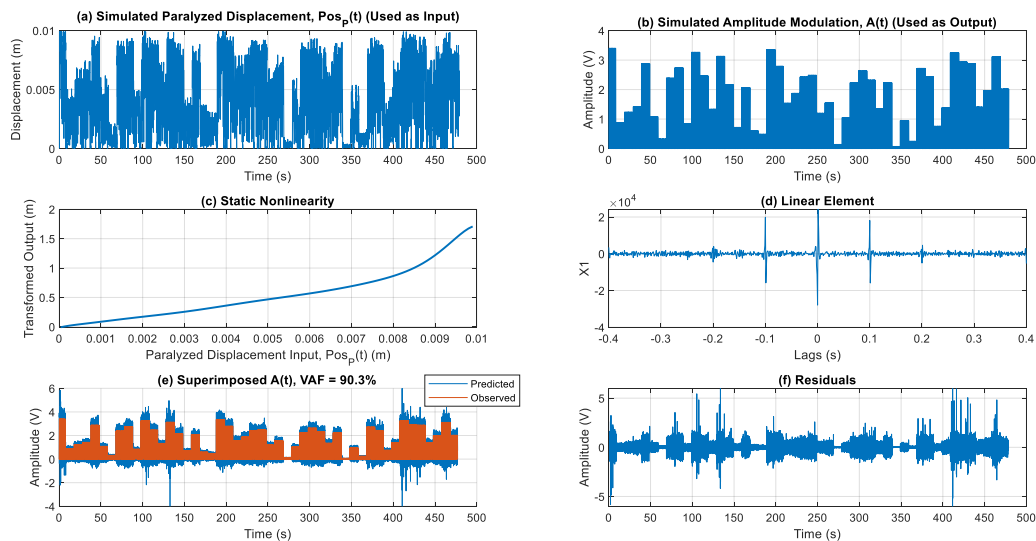


Figure 6-7: Identification of SRS^{-1} Two-Sided Hammerstein Model from SRS Model Data.

Validation trials of the two-sided Hammerstein SRS⁻¹ model demonstrated that the model performed very well on signals not used for identification. Fig. 6-8 shows an example validation trial that achieved a VAF of 91.2%. The two-sided Hammerstein SRS⁻¹ achieved a mean of 91.3% with a standard deviation of 0.6% over 100 validation trials.

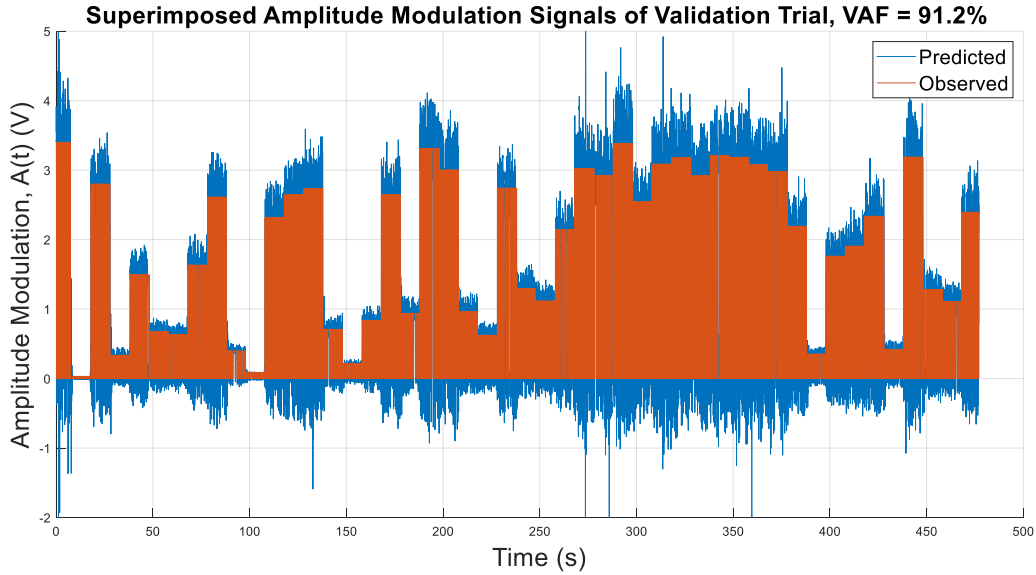


Figure 6-8: Superimposed Predicted and Observed Stimulus Amplitude Modulation Signals, $A(t)$, for a Typical Validation Trial using the Two-Sided Hammerstein SRS⁻¹ Model.

Fig. 6-9 shows the residuals between the predicted and observed $A(t)$ signals in Fig. 6-8. The distribution in Fig. 6-9b shows that the errors were distributed evenly about zero. The power spectrum of the residuals, shown in Fig. 6-9c, shows that the power was low at frequencies less

than 3 Hz and increased up until a power spike at 6.7 Hz. This indicates that the model struggled less with low frequency values.

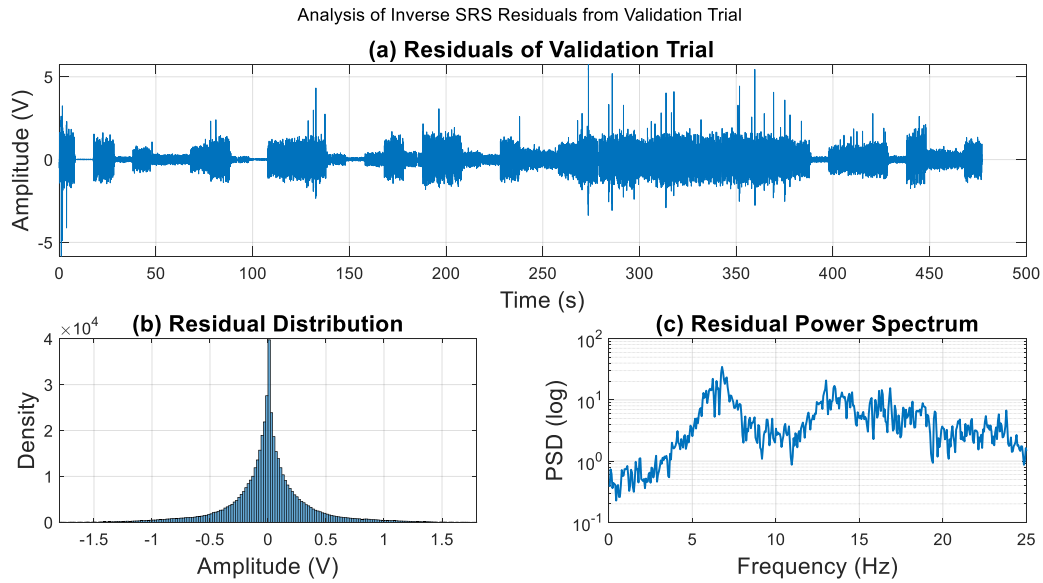


Figure 6-9: Residual Analysis of Validation Trial.

6.2.2 Facial Reanimation Control System Output

To evaluate the FRCS, we compared the predicted paralyzed displacement, $\text{Pos}_P(t)$, to the healthy displacement, $\text{Pos}_H(t)$, and calculated the VAF. Fig. 6-10 shows an example of the desired displacement signal used to generate $E(t)$ from the ERS simulation, the resulting $\text{Pos}_H(t)$ and $\text{Pos}_P(t)$. $\text{Pos}_H(t)$ and $\text{Pos}_P(t)$ are superimposed in Fig. 6-9d and the VAF between $\text{Pos}_H(t)$ and $\text{Pos}_P(t)$ was calculated as 98.7% for this version of the FRCS.

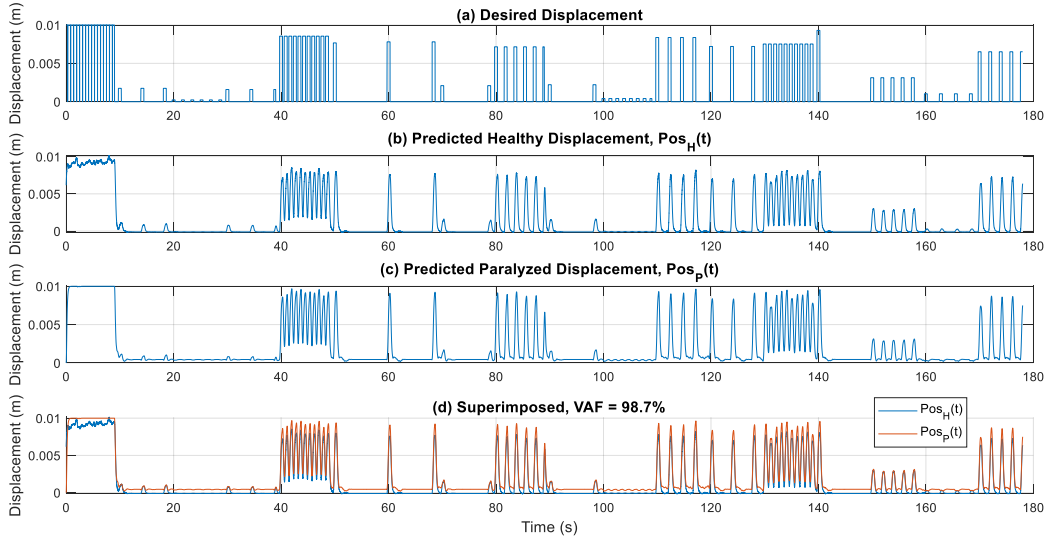


Figure 6-10: Facial Reanimation Control System Response to a “Physiological” Signal.

The FRCS performed consistently well for multiple SRS⁻¹ estimates. To demonstrate this, 10 versions of the FRCS were built, each with a different estimate of the SRS⁻¹ identified with a unique realization of $\text{Pos}_P(t)$ and $A(t)$. Each FRCS version was then validated by using it to predict $\text{Pos}_P(t)$ from 100 realizations of $E(t)$ and calculating the VAF between the predicted $\text{Pos}_P(t)$ and $\text{Pos}_H(t)$. Table 6-2 shows the VAF mean and standard deviation over these 100 trials for all 10 versions of the FRCS.

Table 6-2: VAF Mean and Standard Deviation of Multiple Facial Reanimation Control Systems over 100 Trials.

FRCS Model	1	2	3	4	5	6	7	8	9	10
VAF mean (%)	98.5	98.5	98.6	98.8	98.7	98.6	98.6	98.6	98.7	98.7
VAF Std (%)	0.3	0.4	0.3	0.1	0.2	0.3	0.3	0.3	0.3	0.3

Fig. 6-11 shows residuals between $\text{Pos}_H(t)$ and $\text{Pos}_P(t)$ of Fig. 6-10. The residuals in Fig. 6-11a were estimated by subtracting $\text{Pos}_P(t)$ from $\text{Pos}_H(t)$. Their residual distribution in Fig. 6-11b shows that the errors between these two signals had a negative offset. This means that the $\text{Pos}_P(t)$ was consistently larger than $\text{Pos}_H(t)$ which can be clearly seen in Fig. 6-10d. This offset is quite small and so it doesn't dramatically impact the VAF of the model. The spectrum in Fig. 6-11c shows that the errors were concentrated in low frequencies with the power dropping 92.7% from 0 Hz to 2 Hz.

Simulation Studies of Functional Electrical Stimulation for Facial Reanimation
Patrick Brebner

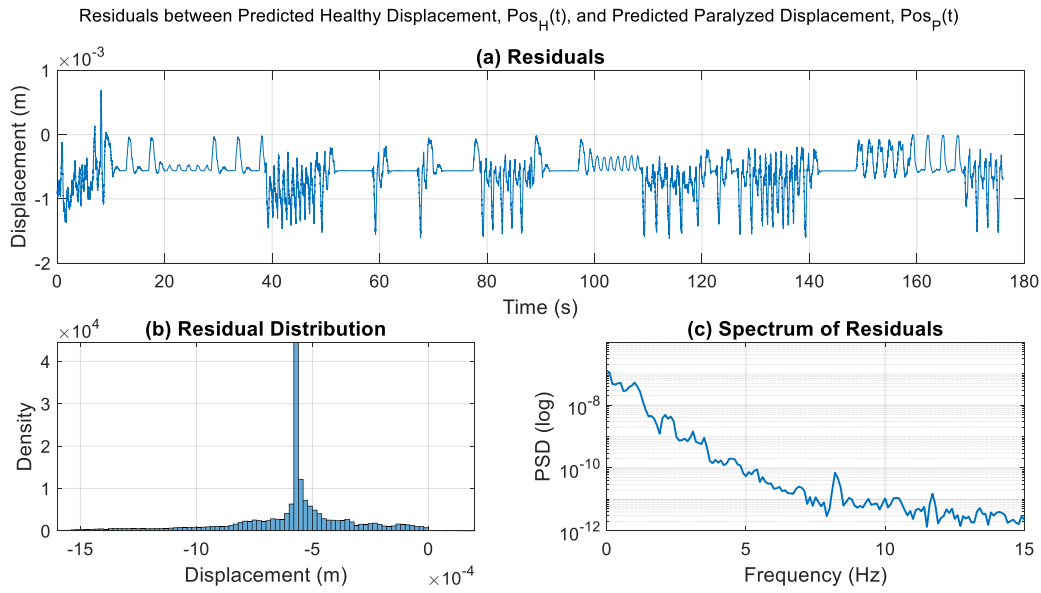


Figure 6-11: Analysis of the Residuals between Healthy Displacement, $Pos_H(t)$, and Predicted Paralyzed Displacement, $Pos_P(t)$.

To determine if there was a consistent frequency dependent error in the models, we looked at the coherence between $Pos_H(t)$ and $Pos_P(t)$. We know that the “physiological” displacements the FRCS is trying to predict are mainly in the range of 0 to 1.8 Hz. Fig. 6-12 shows coherence between $Pos_H(t)$ and $Pos_P(t)$ from 0 to 5 Hz. As expected, the coherence is very high up until 1.5 Hz and then drops to just below 0.9 by 1.8 Hz. This indicates that the results had no significant consistent frequency dependent errors below 1.8 Hz.

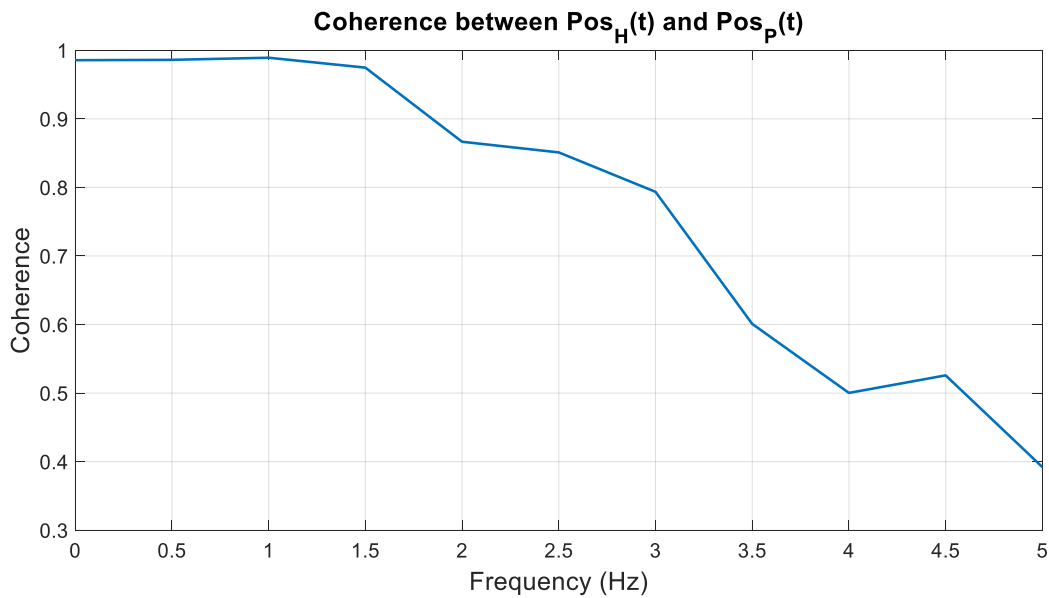


Figure 6-12: Coherence between Healthy Displacement, $\text{Pos}_H(t)$, and Predicted Paralyzed Displacement, $\text{Pos}_P(t)$.

Chapter 7: Discussion & Conclusion

Although the technique of facial pacing has the potential to drastically improve the acute and long-term treatment of facial palsy, the relationship between EMG, electrical stimulus, muscle force and displacement needs to be fully understood and modeled to implement such a technique. The work in this thesis addresses this problem, creating a suitable control system for the proposed facial reanimation device. The facial reanimation control system (FRCS) developed in this thesis was able to reliably predict a paralyzed displacement, $\text{Pos}_P(t)$, with high accuracy and coherence when compared to the healthy displacement, $\text{Pos}_H(t)$. The results of this thesis are a big step towards the realization of the proposed facial reanimation device.

We found that the ERS simulation model, which was based on muscle activation dynamics, produced a realistic $\text{Pos}_H(t)$ from a neural command input. Furthermore, the EMG simulation produced a reasonable input signal for ERS identification. As expected, the ERS was identified as a Hammerstein model with a full-wave rectifier as the nonlinearity and a low pass filter as the linear element. Using a Hammerstein model as the ERS achieved a 97.5% and 99.2% identification accuracy when using a PRBS and “physiological” input, respectively. When tested with signals not used for identification the model still achieved an average accuracy above 97%, indicating that the identified models were able to handle a wide range of inputs. However, there were some limitations for the inputs used to identify the models. Making sure that the signals used for identification were robust enough was proven by analyzing the effects of identification signal amplitude and number of movements over the record length on validation accuracy. It was shown that if the desired displacement amplitude of the identification signal was only 1.5 mm lower than the maximum potential amplitude, the identified ERS model would perform significantly worse when tested with other signals that utilized the full range. For the number of movement pulses in the identification signal over the record length, the ERS was able to handle a low number of movements, achieving a 95% validation accuracy with only 2 movement pulses. In general, these results are promising as it’s reasonable to assume that a properly designed experiment would be able to create data covering the full range of inputs with at least 2 movements over the record length. Finally, the effects of record length and output noise on the identified ERS were minimal. The ERS model had high validation accuracies at record lengths

above 4 seconds and SNRs above -16 dB, which is once again acceptable for an experimental trial. Overall, the results indicate that we could successfully identify an ERS model between EMG and $\text{Pos}_H(t)$ that could be used in the FRCS.

We found that the SRS simulation model, based on the model of Bobet and Stein, produced a realistic $\text{Pos}_P(t)$ from a stimulus amplitude modulation input, $A(t)$. For the identified SRS, a Wiener model achieved a 97.7% and 98.6% identification accuracy for the PRBS and “physiological” inputs, respectively. When tested with signals not used for identification the model still achieved an average 96% validation accuracy, indicating that the model was able to handle a wide range of inputs. The residuals of the model show a small offset when predicting a “physiological” displacement. The spectrum of the residuals was not white but besides a power spike near 0 Hz, there was no other frequency with a significant residual power. As with the ERS model, there were some limitations on the input signals used for identification. It was shown that if the desired displacement amplitude of the identification signal was only 1.5 mm lower than the maximum potential amplitude, the identified SRS model would perform significantly worse when tested with other signals that utilized the full range. For the number of movements in the identification signal over the record length, the SRS was not as robust as the ERS model as it required at least 25 movement pulses to achieve a high accuracy. Finally, the effects of record length and output noise on the identified SRS were minimal. The SRS model had high validation accuracies at all record lengths above 13 seconds and all SNRs above -16 dB. It would be reasonable to assume that an experimental trial would be able to accommodate these limitations on the identification input and noise. Overall, the results indicate that we could successfully identify an SRS model between $A(t)$ and $\text{Pos}_P(t)$ that could be used in the FRCS.

The ERS and SRS^{-1} were combined to create the FRCS. We only used the ERS and SRS models identified from “physiological” inputs to build the FRCS since these inputs are what would be available in practice. When identifying the SRS^{-1} , we found that a two-sided Hammerstein with 400 lags in the IRF was the best model structure due to its high accuracy and computational efficiency over the LNL model. We found that the FRCS, using the Hammerstein SRS^{-1} , was very robust and consistently achieved a validation accuracy above 98%, regardless of input. Analyzing the residuals between the $\text{Pos}_P(t)$ and $\text{Pos}_H(t)$ of the FRCS show that the $\text{Pos}_P(t)$ was consistently

larger than the $\text{Pos}_H(t)$. However, this offset was small enough that it had little effect on the VAF of the model. The residual spectrum shows that the errors in the model were concentrated in frequencies around 6.7 Hz and there was very little power in frequencies below 3 Hz. Finally, there was a high coherence between the $\text{Pos}_P(t)$ and $\text{Pos}_H(t)$ up until 1.8 Hz indicating no frequency dependent errors below his frequency. These results are promising as the “physiological” movements being predicted by the FRCS were mainly under 1.8 Hz. Overall, these results strongly indicate that the FRCS is an accurate representation of facial paralysis and can accurately produce $\text{Pos}_P(t)$ that would match $\text{Pos}_H(t)$. The FRCS developed in this thesis will be useful as a reference for when experimental data is available.

Thesis Limitations

The results of this thesis are promising, although there are still some areas that could lead to potential errors. The two main limitations of the thesis are the simulation models and the simulated data they produce. For both simulation models, estimating the parameters of the spring-mass-damper muscle model was challenging. There are not many sources specifically for facial muscle, and for the few sources available, the results can vary widely based on the techniques used to determine the spring constant and damping coefficient. Therefore, the estimates of these parameters used in this thesis are generalizations. Furthermore, although this thesis project mainly focused on modeling the isometric contraction it is important to understand that there is further complexity that could be incorporated into the model. It is important to note that initially focusing on a model for isometric contractions is not a waste of time. Isometric models are a perfect foundation upon which to build a non-isometric one [70]. Another simulation model weakness is the simulation of the EMG from neural input. The technique used to generate the EMG from neural input is very simple. There are more accurate ways to simulate the EMG, however these require knowledge of the muscle fiber positions relative to the detecting electrode, the distribution of muscle fibers among the motor units of a muscle, and the firing times of individual motor units [32, 33]. Since this information is difficult to get, we opted for the simpler method of EMG simulation. These limitation in the simulation models lead to limitations in the simulated data. In physiologically based systems, simulated data is difficult to generate in a way that accurately represents the complexity of the movement in real world data. There are

almost always too many factors to consider to create completely realistic data. On top of that, when trying to emulate data from animal models, there is likely going to be some unpredictable randomness in the behavior of the signal. Overall, these limitations of the thesis stem from the difficult task of having to simulate a physiological system. If we had access to experimental data, the previously mentioned problems would be eliminated as we would not need to make so many assumptions about the behavior and properties of muscle.

Recommendation for Future Work

These simulation trials assumed that we had only isometric contractions where the muscle length is assumed constant throughout the contraction. As covered in the background section, we know that muscle of changing length behaves differently. There are force-length and force-velocity relationships that were not modeled in our simulation models. This could be achieved by having the parameters of the mass-spring-damper muscle load model change depending on muscle length and velocity of contraction. Including this in the model would add some additional nonlinear behavior to the model but would be a more realistic representation of muscle behavior. Furthermore, the simulated model was kept at 1 degree of freedom (DOF) for simplicity. A next step might include repeating the same process for a multiple DOF model of the facial muscles.

If we were to get access to experimental data, we could take what we have learned in this thesis and use it to identify the ERS and SRS models with real data. This data would enable us to build a FRCS that could be implemented in the proposed facial reanimation device intended for rat models. Once completed, the next step for the control system would be to incorporate the high frequency alternating current (HFAC) required to suppress aberrant movement in the facial reanimation device.

Conclusion

In conclusion, the goal of this thesis was to develop a facial reanimation control system (FRCS) for use in the proposed facial reanimation device. The device uses EMG signals from the healthy side muscle activity to drive electrical stimulation required to create symmetrical movement on the paralyzed side. The FRCS developed in this thesis takes the EMG input and determines the corresponding stimulus required.

Overall, we demonstrated that we could identify models of facial paralysis from simulated data that were robust and achieved high accuracies on signals of reasonable record length and output noise. With the simulation models we were able to generate data to: 1) Develop and validate an algorithm to predict healthy movement from simulated EMG signals, 2) Develop and validate an algorithm to predict paralyzed displacement from a stimulus amplitude modulation input, 3) Combine everything together to demonstrate how the system would work in practice. Although the simulation models might not fully capture the behavior of the system, it still demonstrates a proof of concept. The models simulated and identified in this thesis show the type of the relationship between the EMG, stimulus, and displacement that would also be seen in the experimental rat model. Understanding this relationship is key to providing insight into the dynamics of facial muscle and building the proposed prosthetic device.

References

- [1] E. R. K. J. H. S. T. M. J. S. A. Siegelbaum, *Principles of Neural Science*, 5th ed. McGraw-Hill Companies Inc, 2013.
- [2] S. E. Coulson, J. O'Dwyer N, R. D. Adams, and G. R. Croxson, "Expression of emotion and quality of life after facial nerve paralysis," *Otol Neurotol*, vol. 25, no. 6, pp. 1014-9, Nov 2004, doi: 10.1097/00129492-200411000-00026.
- [3] J. M. VanSwearingen, J. F. Cohn, J. Turnbull, T. Mrzai, and P. Johnson, "Psychological distress: linking impairment with disability in facial neuromotor disorders," *Otolaryngol Head Neck Surg*, vol. 118, no. 6, pp. 790-6, Jun 1998, doi: 10.1016/S0194-5998(98)70270-0.
- [4] N. Jowett, R. E. Kearney, C. J. Knox, and T. A. Hadlock, "Toward the Bionic Face: A Novel Neuroprosthetic Device Paradigm for Facial Reanimation Consisting of Neural Blockade and Functional Electrical Stimulation," *Plast Reconstr Surg*, vol. 143, no. 1, pp. 62e-76e, Jan 2019, doi: 10.1097/PRS.0000000000005164.
- [5] D. N. Tobey and D. Sutton, "Contralaterally elicited electrical stimulation of paralyzed facial muscles," *Otolaryngology*, vol. 86, no. 5, pp. ORL-812-8, Sep-Oct 1978, doi: 10.1177/019459987808600528.
- [6] E. Henneman and C. B. Olson, "Relations between Structure and Function in the Design of Skeletal Muscles," *J Neurophysiol*, vol. 28, pp. 581-98, May 1965, doi: 10.1152/jn.1965.28.3.581.
- [7] B. H. Zhou, M. Solomonow, R. Baratta, and R. D'Ambrosia, "Dynamic performance model of an isometric muscle-joint unit," *Med Eng Phys*, vol. 17, no. 2, pp. 145-50, Mar 1995, doi: 10.1016/1350-4533(95)91887-m.
- [8] B. M. Doucet, A. Lam, and L. Griffin, "Neuromuscular electrical stimulation for skeletal muscle function," *Yale J Biol Med*, vol. 85, no. 2, pp. 201-15, Jun 2012. [Online]. Available: <https://www.ncbi.nlm.nih.gov/pubmed/22737049>.
- [9] L. L. Baker, B. R. Bowman, and D. R. McNeal, "Effects of waveform on comfort during neuromuscular electrical stimulation," *Clin Orthop Relat Res*, no. 233, pp. 75-85, Aug 1988. [Online]. Available: <https://www.ncbi.nlm.nih.gov/pubmed/3261222>.
- [10] K. A. Sluka and D. Walsh, "Transcutaneous electrical nerve stimulation: basic science mechanisms and clinical effectiveness," *J Pain*, vol. 4, no. 3, pp. 109-21, Apr 2003, doi: 10.1054/jpai.2003.434.
- [11] N. Bhadra and P. H. Peckham, "Peripheral nerve stimulation for restoration of motor function," *J Clin Neurophysiol*, vol. 14, no. 5, pp. 378-93, Sep 1997, doi: 10.1097/00004691-199709000-00004.
- [12] L. Mesin, E. Merlo, R. Merletti, and C. Orizio, "Investigation of motor unit recruitment during stimulated contractions of tibialis anterior muscle," *J Electromyogr Kinesiol*, vol. 20, no. 4, pp. 580-9, Aug 2010, doi: 10.1016/j.jelekin.2009.11.008.
- [13] M. A. Attiah, J. de Vries, A. G. Richardson, and T. H. Lucas, "A Rodent Model of Dynamic Facial Reanimation Using Functional Electrical Stimulation," *Front Neurosci*, vol. 11, p. 193, 2017, doi: 10.3389/fnins.2017.00193.
- [14] O. Lagerquist and D. F. Collins, "Influence of stimulus pulse width on M-waves, H-reflexes, and torque during tetanic low-intensity neuromuscular stimulation," *Muscle Nerve*, vol. 42, no. 6, pp. 886-93, Dec 2010, doi: 10.1002/mus.21762.
- [15] S. D. McPhee, A. G. Bracciano, B. W. Rose, and P. American Occupational Therapy Association Commission on, "Physical agent modalities: a position paper," *Am J Occup Ther*, vol. 62, no. 6, pp. 691-3, Nov-Dec 2008, doi: 10.5014/ajot.62.6.691.

- [16] M. Ilves *et al.*, "Functional electrical stimulation for facial pacing: Effects of waveforms on movement intensity and ratings of discomfort," *Biomedical Signal Processing and Control*, vol. 60, p. 101992, 2020/07/01/ 2020, doi: <https://doi.org/10.1016/j.bspc.2020.101992>.
- [17] S. Coupaud, H. Gollee, K. J. Hunt, M. H. Fraser, D. B. Allan, and A. N. McLean, "Arm-cranking exercise assisted by Functional Electrical Stimulation in C6 tetraplegia: a pilot study," *Technol Health Care*, vol. 16, no. 6, pp. 415-27, 2008. [Online]. Available: <https://www.ncbi.nlm.nih.gov/pubmed/19212037>.
- [18] N. T. Van Duijnhoven, T. W. Janssen, D. J. Green, C. T. Minson, M. T. Hopman, and D. H. Thijssen, "Effect of functional electrostimulation on impaired skin vasodilator responses to local heating in spinal cord injury," *J Appl Physiol (1985)*, vol. 106, no. 4, pp. 1065-71, Apr 2009, doi: 10.1152/japplphysiol.91611.2008.
- [19] H. L. Gerrits, A. de Haan, A. J. Sargeant, H. van Langen, and M. T. Hopman, "Peripheral vascular changes after electrically stimulated cycle training in people with spinal cord injury," *Arch Phys Med Rehabil*, vol. 82, no. 6, pp. 832-9, Jun 2001, doi: 10.1053/apmr.2001.23305.
- [20] C. I. Price and A. D. Pandyan, "Electrical stimulation for preventing and treating post-stroke shoulder pain," *Cochrane Database Syst Rev*, no. 4, p. CD001698, 2000, doi: 10.1002/14651858.CD001698.
- [21] S. Itoh, T. Ohta, Y. Sekino, Y. Yukawa, and K. Shinomiya, "Treatment of distal radius fractures with a wrist-bridging external fixation: the value of alternating electric current stimulation," *J Hand Surg Eur Vol*, vol. 33, no. 5, pp. 605-8, Oct 2008, doi: 10.1177/1753193408092253.
- [22] N. Sahin, H. Ugurlu, and I. Albayrak, "The efficacy of electrical stimulation in reducing the post-stroke spasticity: a randomized controlled study," *Disabil Rehabil*, vol. 34, no. 2, pp. 151-6, 2012, doi: 10.3109/09638288.2011.593679.
- [23] P. Gargiulo *et al.*, "Muscle, tendons, and bone: structural changes during denervation and FES treatment," *Neurol Res*, vol. 33, no. 7, pp. 750-8, Sep 2011, doi: 10.1179/1743132811Y.0000000007.
- [24] P. Langhorne, F. Coupar, and A. Pollock, "Motor recovery after stroke: a systematic review," *Lancet Neurol*, vol. 8, no. 8, pp. 741-54, Aug 2009, doi: 10.1016/S1474-4422(09)70150-4.
- [25] D. R. Dolbow, A. S. Gorgey, D. X. Cifu, J. R. Moore, and D. R. Gater, "Feasibility of home-based functional electrical stimulation cycling: case report," *Spinal Cord*, vol. 50, no. 2, pp. 170-1, Feb 2012, doi: 10.1038/sc.2011.115.
- [26] M. Vanderthommen and J. Duchateau, "Electrical stimulation as a modality to improve performance of the neuromuscular system," *Exerc Sport Sci Rev*, vol. 35, no. 4, pp. 180-5, Oct 2007, doi: 10.1097/jes.0b013e318156e785.
- [27] C. M. Gregory and C. S. Bickel, "Recruitment patterns in human skeletal muscle during electrical stimulation," *Phys Ther*, vol. 85, no. 4, pp. 358-64, Apr 2005. [Online]. Available: <https://www.ncbi.nlm.nih.gov/pubmed/15794706>.
- [28] A. Carpentier, J. Duchateau, and K. Hainaut, "Motor unit behaviour and contractile changes during fatigue in the human first dorsal interosseous," *J Physiol*, vol. 534, no. Pt 3, pp. 903-12, Aug 1 2001, doi: 10.1111/j.1469-7793.2001.00903.x.
- [29] R.-C. L. Ignacio, Gila-Useros; Armando, Malanda-Trigueros, A. Ihsan M, Ed. *Motor Unit Action Potential Duration: Measurement and Significance (Advances in Clinical Neurophysiology)*. 2012.
- [30] B. Feinstein, B. Lindegard, E. Nyman, and G. Wohlfart, "Morphologic studies of motor units in normal human muscles," *Acta Anat (Basel)*, vol. 23, no. 2, pp. 127-42, 1955, doi: 10.1159/000140989.
- [31] J. Mariani, B. Maton, and S. Bouisset, "Force gradation and motor unit activity during voluntary movements in man," *Electroencephalogr Clin Neurophysiol*, vol. 48, no. 5, pp. 573-82, May 1980, doi: 10.1016/0013-4694(80)90292-8.

- [32] D. W. Stashuk, "Simulation of electromyographic signals," *J Electromyogr Kinesiol*, vol. 3, no. 3, pp. 157-73, 1993, doi: 10.1016/S1050-6411(05)80003-3.
- [33] A. Hamilton-Wright and D. W. Stashuk, "Physiologically based simulation of clinical EMG signals," *IEEE Trans Biomed Eng*, vol. 52, no. 2, pp. 171-83, Feb 2005, doi: 10.1109/TBME.2004.840501.
- [34] M. B. Raez, M. S. Hussain, and F. Mohd-Yasin, "Techniques of EMG signal analysis: detection, processing, classification and applications," *Biol Proced Online*, vol. 8, pp. 11-35, 2006, doi: 10.1251/bpo115.
- [35] S. Rampichini, T. M. Vieira, P. Castiglioni, and G. Merati, "Complexity Analysis of Surface Electromyography for Assessing the Myoelectric Manifestation of Muscle Fatigue: A Review," *Entropy (Basel)*, vol. 22, no. 5, May 7 2020, doi: 10.3390/e22050529.
- [36] R. A.-A. R. K. S. F. E. Zahedi, "Estimation of Muscle Force with EMG Signals Using Hammerstein-Wiener Model," *BIOMED 2011, IFMBE Proceedings*, vol. 35, pp. 157-160, 2011.
- [37] T. S. Buchanan, D. G. Lloyd, K. Manal, and T. F. Besier, "Neuromusculoskeletal modeling: estimation of muscle forces and joint moments and movements from measurements of neural command," *J Appl Biomech*, vol. 20, no. 4, pp. 367-95, Nov 2004, doi: 10.1123/jab.20.4.367.
- [38] N. N. Donaldson, H. Gollee, K. J. Hunt, J. C. Jarvis, and M. K. Kwende, "A radial basis function model of muscle stimulated with irregular inter-pulse intervals," *Med Eng Phys*, vol. 17, no. 6, pp. 431-41, Sep 1995, doi: 10.1016/1350-4533(94)00013-y.
- [39] Q. Shao, D. N. Bassett, K. Manal, and T. S. Buchanan, "An EMG-driven model to estimate muscle forces and joint moments in stroke patients," *Comput Biol Med*, vol. 39, no. 12, pp. 1083-8, Dec 2009, doi: 10.1016/j.combiomed.2009.09.002.
- [40] F. L. I. M. C. T. F. E. Rogers, "Recursive Identification of Hammerstein Systems with Application to Electricallt Stimulated Muscle," *Control Engineering Practice*, vol. 20, pp. 386-396, 2012.
- [41] L. Vodovnik, W. J. Crochetiere, and J. B. Reswick, "Control of a skeletal joint by electrical stimulation of antagonists," *Med Biol Eng*, vol. 5, no. 2, pp. 97-109, Mar 1967, doi: 10.1007/BF02474498.
- [42] D. Jandali and P. C. Revenaugh, "Facial reanimation: an update on nerve transfers in facial paralysis," *Curr Opin Otolaryngol Head Neck Surg*, vol. 27, no. 4, pp. 231-236, Aug 2019, doi: 10.1097/MOO.0000000000000543.
- [43] M. H. Hohman and T. A. Hadlock, "Etiology, diagnosis, and management of facial palsy: 2000 patients at a facial nerve center," *Laryngoscope*, vol. 124, no. 7, pp. E283-93, Jul 2014, doi: 10.1002/lary.24542.
- [44] N. I. o. N. D. a. Stroke. "Bell's Palsy Fact Sheet." NIH.
<https://www.ninds.nih.gov/Disorders/Patient-Caregiver-Education/Fact-Sheets/Bells-Palsy-Fact-Sheet> (accessed 2021).
- [45] P. P. Devriese, T. Schumacher, A. Scheide, R. H. de Jongh, and J. M. Houtkooper, "Incidence, prognosis and recovery of Bell's palsy. A survey of about 1000 patients (1974-1983)," *Clin Otolaryngol Allied Sci*, vol. 15, no. 1, pp. 15-27, Feb 1990, doi: 10.1111/j.1365-2273.1990.tb00427.x.
- [46] A. G. Marson and R. Salinas, "Bell's palsy," *West J Med*, vol. 173, no. 4, pp. 266-8, Oct 2000, doi: 10.1136/ewjm.173.4.266.
- [47] N. Jowett, "A General Approach to Facial Palsy," *Otolaryngol Clin North Am*, vol. 51, no. 6, pp. 1019-1031, Dec 2018, doi: 10.1016/j.otc.2018.07.002.
- [48] R. A. Otto, R. N. Gaughan, J. W. Templer, and W. E. Davis, "Electrical restoration of the blink reflex in experimentally induced facial paralysis," *Ear Nose Throat J*, vol. 65, no. 9, pp. 30-2, 37, Sep 1986. [Online]. Available: <https://www.ncbi.nlm.nih.gov/pubmed/3490367>.

- [49] M. May, J. W. West, and K. H. Hinderer, "Nasal obstruction from facial palsy," *Arch Otolaryngol*, vol. 103, no. 7, pp. 389-91, Jul 1977, doi: 10.1001/archotol.1977.00780240047005.
- [50] J. Valls-Sole, E. S. Tolosa, and M. Pujol, "Myokymic discharges and enhanced facial nerve reflex responses after recovery from idiopathic facial palsy," *Muscle Nerve*, vol. 15, no. 1, pp. 37-42, Jan 1992, doi: 10.1002/mus.880150107.
- [51] A. B. Robey and M. C. Snyder, "Reconstruction of the paralyzed face," *Ear Nose Throat J*, vol. 90, no. 6, pp. 267-75, Jun 2011, doi: 10.1177/014556131109000608.
- [52] B. Hontanilla, D. Marre, and A. Cabello, "Facial reanimation with gracilis muscle transfer neurotized to cross-facial nerve graft versus masseteric nerve: a comparative study using the FACIAL CLIMA evaluating system," *Plast Reconstr Surg*, vol. 131, no. 6, pp. 1241-1252, Jun 2013, doi: 10.1097/PRS.0b013e31828bd4da.
- [53] A. W. Murphey, W. B. Clinkscales, and S. L. Oyer, "Masseteric Nerve Transfer for Facial Nerve Paralysis: A Systematic Review and Meta-analysis," *JAMA Facial Plast Surg*, vol. 20, no. 2, pp. 104-110, Mar 1 2018, doi: 10.1001/jamafacial.2017.1780.
- [54] J. Rothstein and N. T. Berlinger, "Electronic reanimation of facial paralysis--a feasibility study," *Otolaryngol Head Neck Surg*, vol. 94, no. 1, pp. 82-5, Jan 1986, doi: 10.1177/019459988609400114.
- [55] R. A. Otto, "Restoration of function in the paralyzed rabbit orbicularis oculi muscle by direct functional electrical stimulation," *Laryngoscope*, vol. 107, no. 1, pp. 101-11, Jan 1997, doi: 10.1097/00005537-199701000-00020.
- [56] G. R. Griffin and J. C. Kim, "Potential of an electric prosthesis for dynamic facial reanimation," *Otolaryngol Head Neck Surg*, vol. 145, no. 3, pp. 365-8, Sep 2011, doi: 10.1177/0194599811406065.
- [57] E. Otta, F. Folladore Abrosio, and R. L. Hoshino, "Reading a smiling face: messages conveyed by various forms of smiling," *Percept Mot Skills*, vol. 82, no. 3 Pt 2, pp. 1111-21, Jun 1996, doi: 10.2466/pms.1996.82.3c.1111.
- [58] K. L. Schmidt and J. F. Cohn, "Human facial expressions as adaptations: Evolutionary questions in facial expression research," *Am J Phys Anthropol*, vol. Suppl 33, pp. 3-24, 2001, doi: 10.1002/ajpa.2001.
- [59] C. K. Thompson *et al.*, "Robust and accurate decoding of motoneuron behaviour and prediction of the resulting force output," *The Journal of Physiology*, vol. 596, no. 14, pp. 2643-2659, 2018.
- [60] A. L. Hof, "The Relationship between Electromyogram and Muscle Force," vol. 11, no. 3, 1997.
- [61] P. Jaramillo Cienfuegos, A. Shoemaker, R. W. Grange, N. Abaid, and A. Leonessa, "Classical and adaptive control of ex vivo skeletal muscle contractions using Functional Electrical Stimulation (FES)," *PLOS One*, vol. 12, no. 3, 2017.
- [62] R. W. Berg and D. Kleinfeld, "Rhythmic whisking by rat: retraction as well as protraction of the vibrissae is under active muscular control," *J Neurophysiol*, vol. 89, no. 1, pp. 104-17, Jan 2003, doi: 10.1152/jn.00600.2002.
- [63] L. A. Huet and M. J. Hartmann, "The search space of the rat during whisking behavior," *J Exp Biol*, vol. 217, no. Pt 18, pp. 3365-76, Sep 15 2014, doi: 10.1242/jeb.105338.
- [64] I. W. Hunter and M. J. Korenberg, "The identification of nonlinear biological systems: Wiener and Hammerstein cascade models," *Biol Cybern*, vol. 55, no. 2-3, pp. 135-44, 1986, doi: 10.1007/BF00341929.
- [65] *reklab_nlid*. (2015). Robert Kearney Lab. [Online]. Available: https://github.com/reklab/reklab_public
- [66] P. H. Peckham and J. S. Knutson, "Functional electrical stimulation for neuromuscular applications," *Annu Rev Biomed Eng*, vol. 7, pp. 327-60, 2005, doi: 10.1146/annurev.bioeng.6.040803.140103.

- [67] J. Bobet and R. B. Stein, "A simple model of force generation by skeletal muscle during dynamic isometric contractions," *IEEE Trans Biomed Eng*, vol. 45, no. 8, pp. 1010-6, Aug 1998, doi: 10.1109/10.704869.
- [68] J. Bobet, E. R. Gossen, and R. B. Stein, "A comparison of models of force production during stimulated isometric ankle dorsiflexion in humans," *IEEE Trans Neural Syst Rehabil Eng*, vol. 13, no. 4, pp. 444-51, Dec 2005, doi: 10.1109/TNSRE.2005.858461.
- [69] P. Jaramillo Cienfuegos, A. Shoemaker, R. W. Grange, N. Abaid, and A. Leonessa, "Classical and adaptive control of ex vivo skeletal muscle contractions using Functional Electrical Stimulation (FES)," *PLoS One*, vol. 12, no. 3, p. e0172761, 2017, doi: 10.1371/journal.pone.0172761.
- [70] W. Farahat and H. Herr, "A method for identification of electrically stimulated muscle," *Conf Proc IEEE Eng Med Biol Soc*, vol. 2005, pp. 6225-8, 2005, doi: 10.1109/IEMBS.2005.1615918.